Dissertation

submitted to the

Combined Faculties of the Natural Sciences and Mathematics

of the Ruperto-Carola-University of Heidelberg, Germany

for the degree of

Doctor of Natural Science

Put forward by

Mag. rer. nat. Mathias Jäger

born in: Bad Ischl, Austria

Oral Examination: May 2nd 2013

Evolution of galaxies studied by the COMBO-17+4 survey

Referees: Dr. Klaus Meisenheimer

Dr. Thorsten Lisker

Abstract

In this thesis the evolution of galaxies at redshift $z < 2$ was analyzed, using the COMBO-17+4 (Classifying Objects by Medium-Band Observations) survey. This survey used optical as well as near-infrared data from three different fields of view with a total area of 0.625 square degree. On the basis of an H band selected catalog the photometric redshifts, rest-frame colors and masses of 42,134 galaxies to a limiting magnitude of $H = 21.7$ mag were calculated. Using the color bimodality in $(U_{280} - V)$ the galaxies were divided in a red (passive) and a blue (active) population, which were analyzed separately. The results verify the existence of a bimodality up to a redshift of $z = 1.6$. Further the evolution of the luminosity function for both galaxy populations was analyzed in ten redshift bins. In both populations a significant decrease in the characteristic magnitude M_B^* from $z = 2$ to $z = 0.2$ was measured. Moreover the number density of red galaxies showed a slight increase during this time, whereas the number density of blue galaxies was decreasing. An analysis of the mass function showed a constant value of the characteristic mass for both populations and an increase of the mass density for red galaxies from $z = 2$ to $z = 0.2$.

Zusammenfassung

In dieser Arbeit wurde die Entwicklung von Galaxien bei einer Rotverschiebung von $z < 2$ anhand der Daten aus der COMBO-17+4 (Classifying Objects by Medium-Band Observations) Himmelsdurchmusterung untersucht. Diese Durchmusterung setzt sich aus optischen und nah-infrarot Daten zusammen, welche in drei unterschiedlichen Feldern mit einer Gesamtfläche von 0.625 Quadratgrad aufgenommen wurden. Mit Hilfe eines H Band selektierten Katalogs konnten die photometrische Rotverschiebungen, Ruhebandfarben und Massen für insgesamt 42,134 Galaxien bis zu einer Grenzhelligkeit von $H = 21.7$ mag bestimmt werden. Mit Hilfe der Bimodalität in der Farbe $(U_{280} - V)$ konnten die Galaxien in eine rote (passive) und eine blaue (aktive) Population getrennt und in weiterer Folge untersucht werden. Die Ergebnisse verifizieren die Existenz dieser Bimodalität bis zu einer Rotverschiebung von mindestens $z = 1.6$. Des weiteren wurde die Entwicklung der Leuchtkraftunktion für beide Galaxienpopulationen in zehn Rotverschiebungsintervallen untersucht. In beiden Populationen wurde eine signifikante Abnahme der charakteristischen Leuchtkraft M_B^* von $z = 2.0$ nach $z = 0.2$ festgestellt. Zudem stieg die Anzahldichte der roten Galaxien in dieser Zeit leicht an, während jene der blauen Galaxien abnahm. Die Analyse der Massenfunktion zeigte außerdem eine konstante charakteristische Masse für beide Populationen, jedoch eine Zunahme der Massendichte bei roten Galaxien von $z = 2.0$ nach $z = 0.2$.

Contents

List of Figures

List of Tables

List of Acronyms

Acronym	Definition
2MASS	2 Micron All Sky Survey
ΛCDM	Λ Cold Dark Matter
AEGIS	All-wavelength Extended Groth strip International Survey
BHB star	Blue Horizontal Branch star
BPM	Bad Pixel Mask
CADIS	Calar Alto Deep Imaging Survey
CDFS	CADIS Deep Field South
CMD	Color Magnitude Diagram
CM_*D	Color Mass Diagram
COMBO-17	Classifying Objects by Medium-Band Observations in 17 filters
COMBO-17+4	Classifying Objects by Medium-Band Observations in 17+4 filters
COSMOS	COSMOlogical evolution Survey
DEEP2	DEEP2 redshift survey
FPN	Fixed Pattern Noise
GEMS	Galaxy Evolution from Morphology and SEDs
GOODS	Great Observatories Origins Deep Survey
HIROCS	Heidelberg InfraRed Optical Cluster Survey
IMF	Initial Mass Function
LIR	Line Interlaced Read
MANOS	MPI für Astronomie Near-infrared Optical Surveys
MIDAS	Munich Image Data Analysis System
MUSYC	Multi-Wavelength Survey by Yale-Chile
NED	NASA / IPAC Extragalactic Database
NEWFIRM	NEWFIRM medium-band survey
NIR	Near InfraRed
O2k	Omega 2000
PEGASE	Project d'Étude des GAlaxies par Synthèse Évolutive
PSF	Point-Spread Function
RMS	Root Mean Square
SED	Spectral Energy Distribution
SExtractor	Source Extractor
SDSS	Sloan Digital Sky Survey
UKIDSS	UK INfrared Deep SKy Survey
UV	UltraViolet
VVDS	VIMOS VLT Deep Survey
WD	White Dwarf
WFI	Wide Field Imager

Chapter 1

Introduction

To understand the history and future of our Universe we have to understand the creation and evolution of galaxies, as they are the building blocks of the Universe. However, as often the case in astronomy, there is no clear definition for a galaxy (in particular if dwarf galaxies are taken into account). Forbes et al. (2011) summarized several features which we also use for all further definitions of galaxies: they are gravitational bound, contain stars, have a relaxation time less than the Hubble time H_0^{-1}, a half light radius > 100 pc and contain non-baryonic dark matter.

In this chapter, we want to give a short overview on the history of galaxy classification, our actual understanding of the evolution of galaxies and a summary on cosmology.

1.1 Galaxy Classification

Already in1755, the German philosopher Immanuel Kant suspected that the misty stars which were visible with the telescopes of this time were Milky Ways like our own. But it was Hubble who proved in 1925 that the Andromeda galaxy M31 was actually outside of our own galaxy, by using Cepheid stars for the distance measurement.

A year later, Hubble (1926) started to sort the different types of galaxies that he discovered based on their morphology. He distinguished between elliptical galaxies – within which he established subtypes based on their ellipticity from E0 to E7 – and spiral galaxies. For the latter, he created subtypes based on the opening angle of their spiral arms (Sa, Sb and Sc) and for galaxies with and without a central bar (SBa, SBb, SBc). The galaxies classified as ellipticals by Hubble do not have a visible internal structure (i.e. a random motion of their stars) and are often found in denser environments. The spiral-type galaxies,

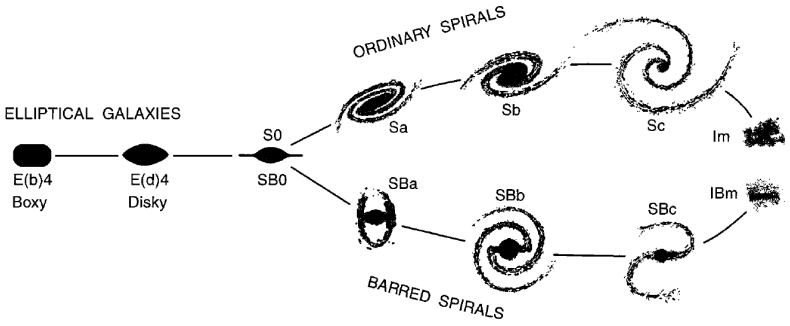

Figure 1.1: The Hubble sequence, adapted by Kormendy and Bender (1996). They added irregular galaxies to the sequence, distinguished between S0 galaxies with and without bars and separated ellipticals into disky and boxy ones instead of sorting them based on their ellipticity.

on the other hand, have clear internal structures like spiral arms, bars, star forming regions and can therefore easily be separated into several subtypes.

Hubble (1936) put the different classes of galaxies he established into a sequence – the so-called Hubble-Sequence or (because of its shape) Hubble Tuning Fork Diagram. In this sequence, he called the elliptical galaxies 'early types' and spiral galaxies 'late types', as he thought ellipticals would evolve into spiral galaxies over time. In the same book, he announced his results on the expansion of the Universe based on the redshifting of the light.

Presently we know that the Hubble sequence has to be read from right to left, as Toomre and Toomre (1972) discovered that actually the spirals (late types) are evolving into ellipticals (early types) and not the other way around. This also explains why elliptical galaxies can be found more often in dense environments, since they form after the merging of spiral galaxies, which frequently happens in dense environments. Nevertheless, the terminology established by Hubble has been kept until today. In time, the Hubble sequence has been changed and additional galaxy types have been added. Kormendy and Bender (1996) for example added Magellanic irregulars to the sequence, distinguished between S0 galaxies with and without a bar and started to subdivide elliptical galaxies into boxy – with an anisotropic random motion – and disky ones – with an isotropic random motion. This updated version of the Hubble sequence can be seen in Figure 1.1.

Despite the fact that the initial sequence by Hubble turned out to have many disadvantages and other astronomers tried to compensate these disadvantages in creating new classification schemes (i.e. de Vaucouleurs (1959); Sandage (1961); Sandage and Tammann (1981)), it is still in use today.

1.1.1 Classification based on color

Next to a morphological / kinematic separation it is also possible to classify galaxies based on their colors. It is already known since Hubble (1936) that there is a correlation between the color of galaxies and their morphology, as most elliptical galaxies consist primarily of old, red stars, whereas most spiral galaxies tend to have blue colors because of ongoing star formation. However, this correlation is not absolute as the morphology of a galaxy is based on its kinematics, whereas the colors are a result of the stellar population. This means that the color of a galaxy gives us information about the stellar population, as well as about the recent and ongoing star formation.

When a color-magnitude diagram for galaxies is created, one can see a clear bimodality in the galaxy population. The galaxies are separated into a sequence of bright, red galaxies (the red sequence) and into a blue cloud; both populations are separated by a sparsely populated area, called the green valley (see Figure 1.2). This bimodality was first discovered by Strateva et al. (2001). Star forming galaxies can be found in the blue cloud, whereas the red sequence is populated by older, quiescent galaxies. The evolution and properties of galaxies in the red sequence were the focus of various papers in the last decade. The galaxies therein are in general passively evolving ellipticals, but about 25% of them seem to be dusty or passive spirals (Rowlands et al., 2011). Wolf et al. tried to answer the question if these galaxies are more often dusty or old in a series of papers (Wolf et al., 2005, 2009). As the star formation rate is in general lower in red spiral galaxies than in blue ones, it is likley that they tend to be old and not just dusty. Regarding the green valley, one has to mention the work of Silk and Mamon (2012), who discovered that allmost all of their studied Seyfert galaxies seem to lie in this valley. But so far no further research on this topic has been done.

One can see that in contrast to the color-magnitude diagram for stars (i.e. the Hertzsprung-Russel diagram), the properties of galaxies are not completely determined by their position in the diagram. In addition, the position of the two populations in the color-magnitude diagram is changing with cosmic time.

1.2 Two Pages on Cosmology

To interpret the data from deep sky surveys we have to make a short excursion into modern cosmology. Our actual understanding of the evolution of the Universe and therefore of the evolution of galaxies is combined in the Λ Cold Dark Matter (ΛCDM) model which combines our knowledge of the Big Bang, the inflation and the acceleration of the Universe, as well as of the growth of

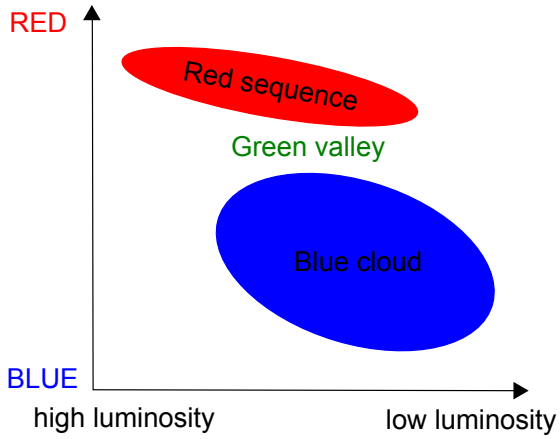

Figure 1.2: A schematic color-magnitude diagram for galaxies. The two galaxy populations from the red sequence and the blue cloud are shown, including their separating, sparsely populated area, called the green valley.

structures in cosmic time. The model also defines the composition of the Universe as 72.6% dark energy, 22.8% dark matter and only 4.6% baryonic matter (Hinshaw et al., 2009). Using these numbers and the Hubble constant H_0 (today assumed with $H_0 \approx 70$ km/s/Mpc) the age of the Universe (13.75 Gyr) can be calculated. The ΛCDM is currently the best model at explaining the observable universe.

Because we know of the expansion of the Universe, all the light we receive is redshifted since it was emitted by its source. The relative wavelength change between the emitted wavelength λ_e and the observed wavelength λ_o determines the redshift z:

$$z = \frac{\lambda_o - \lambda_e}{\lambda_e} - 1 = \frac{1}{a} - 1 \tag{1.1}$$

with a being the scale factor at the time of emission. Lookback time is related to the cosmological redshift and gives the time the light needs to travel from the emitting source to the observer:

$$t_{\text{lookback}} = t_H \int_0^z \frac{dz'}{(1+z')E(z)} \tag{1.2}$$

with $E(z)$ being the dimensionless Hubble parameter which includes the three main parameters of the ΛCDM model:

$$E(z) = \sqrt{\Omega_m(1+z)^3 + \Omega_k(1+z)^2 + \Omega_\Lambda}. \tag{1.3}$$

As the speed of light is limited, we look back in time when we observe distant objects. This allows us to study the evolution of galaxies with time.

The relation between the redshift and the lookback time can be seen in Figure 1.3 (left panel).

The distance of an observed object also changes its apparent magnitude. The object seems to become fainter if the distance between it and the observer becomes larger:

$$m = M + 5\log\left(\frac{D_L}{10\text{pc}}\right) + K(z) \tag{1.4}$$

where m is the apparent magnitudes of the object, M the absolute magnitude and D_L the luminosity distance which again uses the Hubble parameter E_z (see Equation 1.3). $K(z)$ gives the k-correction of the galaxy:

$$D_L = (1+z)\frac{c}{H_0}\int_0^z E(z) \tag{1.5}$$

$$K = -2.5\log\left[(1+z)\frac{L_{(1+z)\lambda}}{L_\lambda}\right] \tag{1.6}$$

To calculate a correct apparent magnitude m a k-correction is necessary because the redshifted object emits its light L_λ in a different pass-band than the observed ($L_{(1+z)\lambda}$) one. Knowing the redshift of an object and the apparent magnitude in at least one filter, the three equations above can be used to calculate the k-correction, the luminosity distance and the absolute magnitude of the object. The relation between the redshift and the luminosity distance can be seen in Figure 1.3 (right panel).

Another important scale for lookback surveys is the comoving volume V_c, which is needed to study galaxies in different redshift slices of the Universe. This volume is defined by the measured volume in which the number density of non-evolving objects remains constant with redshift:

$$V_c = \frac{4\pi}{3}(D_c)^3 \tag{1.7}$$

The above formula assumes a flat Universe. Here, D_c is the comoving distance, which is defined by

$$D_c = D_H \int_0^z \frac{dz}{\sqrt{\Omega_m(1+z)^3 + \Omega_\Lambda}}. \tag{1.8}$$

In the above formula, $D_H = c/H_0$. For a more detailed review on distance measurements in cosmology see Hogg (1999).

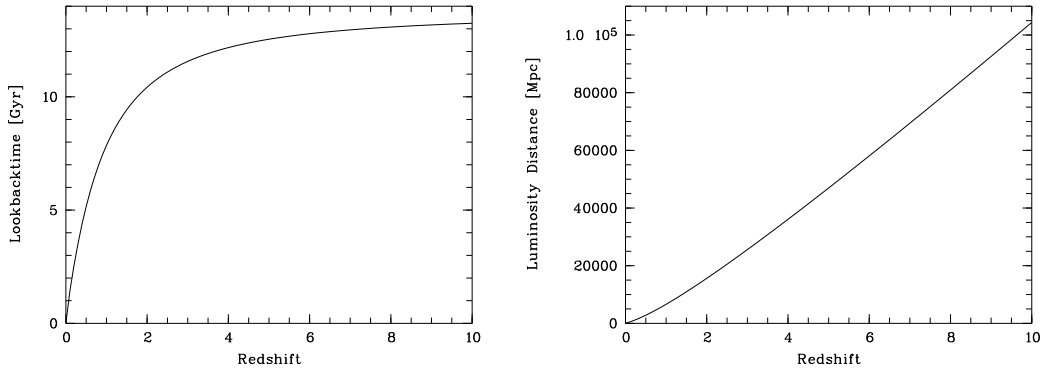

Figure 1.3: Left panel: Lookbacktime as function of redshift. Right panel: Luminosity distance as function of redshift. For both functions a ΛCDM model with $\Omega_m = 0.28$, $\Omega_\lambda = 0.73$ and $H_0 = 71$ km/s/Mpc was used.

1.3 Photometric Lookback Surveys and SEDs

To investigate the evolution of galaxies through cosmic time, a large number of objects and an accurate measurement of the objects redshifts are necessary. In the last decade, photometric redshift surveys became more and more common as a tool for cosmological lookback surveys. The use of multi-filter photometric surveys has several advantages: they can distinguish better between stars, quasars and different types of galaxies than it would be possible with a classification based on morphology. They can also cover larger areas on the sky and classify more galaxies than spectroscopic observations, which are extremely time consuming due to the faintness of high redshift galaxies.

Photometric redshift surveys are based on the idea of observing the same area of sky with different filters (normally a mixture of small-, medium- and broad-band filters). Using the fluxes obtained in the different filters, colors can be calculated. Observed or synthetic Spectral Energy Distributions (SEDs) are then fitted to the observed fluxes, therefore the objects can be classified depending on their SED. The redshift of the objects is most often determined by the use of the 4000 Å break – a result of absorption caused by calcium lines in stellar atmospheres – which is the most distinct feature in the SED of most objects. The accuracy of the resulting photometric redshifts from these surveys depend strongly on the filters and templates used, as well as on the fitting of the templates to the observed fluxes.

The Calar Alto Deep Imaging Survey (CADIS) was the first photometric survey which produced a usable classification of quasars, galaxies and stars (Meisenheimer et al., 1998). The survey was used to study galaxy evolution at $z < 1$ and proved that the resulting data was accurate enough to study the evolution of galaxies and quasars. The success of CADIS directly led to the

COMBO-17 and later to the COMBO-17+4 surveys which were based on the same idea of filter combination and classification. It also opened the door to further projects, some of which are presented in Chapter 2.

1.4 Galaxy Evolution

In the ΛCDM model, galaxies are formed at the bottom of dark matter potential wells and grow mainly through mergers from small Gaussian density distributions to larger structures (White and Rees, 1978). The growth through mergers can be observed and is also supported by various theoretical simulations (Kauffmann et al., 2003). Of course galaxies can also change their properties through other effects like ram pressure stripping, galaxy harassment or merger induced starbursts (Hopkins et al., 2009). However, the evolution in this bottom-up scenario should be observable. Common tools to investigate the evolution of galaxies are the already mentioned color-magnitude diagrams, mass- and luminosity functions as well as morphological studies (the latter are most often restricted to the local Universe).

1.4.1 Evolution in Colors and Magnitudes

One of the main tools to analyze galaxy evolution in the last years have been color-magnitude diagrams. Especially the evolution of the red sequence and the galaxies therein were topics of interest. Bell et al. (2004b) were the first who proved – using the COMBO-17 data – that the red sequence was visible at least up to $z = 1$. More recent results seem to confirm that the red sequence even exits up to $z = 2$ and possibly even beyond this redshift. Cirasuolo et al. (2007) found a bimodality up to $z = 1.5$ with 22,000 galaxies ($K < 22.5$ mag) of the UKIDSS survey using $(U - B)$ rest-frame colors. Using $(B - I)$ rest-frame colors, Franzetti et al. (2006) confirmed the existence of the red sequence up to $z = 2$. Analyzing spectroscopic data, Kriek et al. (2008) found indications for a red sequence at $z > 2$ and color-color plots by Brammer et al. (2011) showed that the bimodality exists most likely up to $z = 2.2$. Whitaker et al. (2011) speculated, on the basis of data acquired from the AEGIS and COSMOS surveys, that with enough data the bimodality would be visible until $z \approx 3$ where it then would collapse. On the other hand, Kajisawa et al. (2010) only detected a bimodal galaxy population up to $z = 1$ in the GOODS North field despite the fact that the sample covers galaxies up to $z = 2.5$. Nevertheless, most of these surveys have the disadvantage of low number counts at $z > 1$, so that statistics becomes unreliable, or they only have a small field of view, so that the selected galaxies become biased due to cosmological inhomogeneities in the distribution of galaxies. If the results are based on a few spectroscopicly

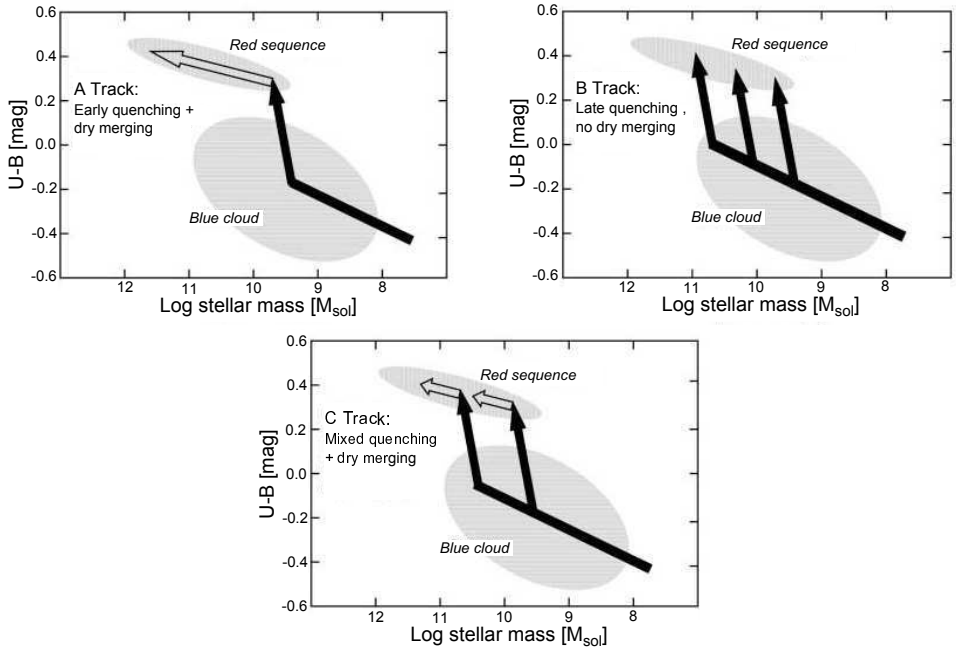

Figure 1.4: The three panels represent three different models for the migration of galaxies from the blue cloud to the red sequence on the basis of star formation quenching and mergers (Faber et al., 2007). It seems that a mixture of early and late quenching combined with dry and wet merger – which is shown in the lower panel – can represent observational data best.

investigated galaxies, also selection effects (i.e. brightness) have to be taken into account. This is one of the main advantages of the COMBO-17+4 survey which is explained in more detail in Section 2. Nicol et al. (2011), who analyze the Abell 901 field of the COMBO-17+4 survey, were able to identify the red sequence in this field up to $z = 1.8$

We also want to take a closer look into the properties of the galaxies in the red sequence and the blue cloud and how these galaxy populations evolve in time. At redshift $z < 1$ the bright end of the red sequence is dominated by massive elliptical galaxies, whereas passive spiral galaxies dominate the faint end (Cassata et al., 2008). If we investigate the population of the blue cloud, we see that it is mainly populated by early type galaxies (Cassata et al., 2008). Also the total number of galaxies in the cloud seems to stay constant over time (Brammer et al., 2011). However, Bell et al. (2004b) discovered that the number density of luminous blue galaxies has decreased strongly since $z = 1$. In the same time the stellar mass of the galaxies in the red sequence doubled. It also has to be mentioned that galaxies at higher redshift are in general bluer than at lower redshift because of a higher star formation rate during this time.

How galaxies evolve from the blue cloud to the red sequence is still a matter of debate. Faber et al. (2007) summarized in their work the three most common

theories on this topic which are shown in Figure 1.4. All models assume that galaxies are built out of blue galaxies when star formation is quenched during a gas-rich major merger. The merger would double the mass of the galaxy and shift it into the red sequence where it would evolve trough a series of gas-poor mergers. In the left panel (A track) of Figure 1.4 the quenching of star formation occurs when the blue galaxies are still small and the evolution of red galaxies takes place directly in the red sequence with the help of dry (i.e. gas poor) mergers. The right panel (B track) on the other hand uses a late quenching where galaxies assemble their mass in the blue cloud. With a single merger they migrate into the red sequence with no further dry mergers. The bottom panel (C track) uses a combination of the other two models and best describes the properties of galaxies in the red sequence in the local universe as well as at redshift $z = 1$.

1.4.2 Evolution in Luminosity

A second important tool to study the evolution of galaxies are luminosity functions, which count the number of galaxies of a specific magnitude M and magnitude interval $M + dM$ per volume unit. As for these functions, absolute magnitudes are needed and an accurate measurement of the distance has to be given. Very often the luminosity functions of blue and red galaxies are studied separately or only specific areas in surveys – like overdensities – are investigated.

Wolf et al. (2003a) were the first to create luminosity functions for the COMBO-17 survey and Bell et al. (2004b) studied luminosity functions in the same survey for galaxies in the red sequence. An extended study of the luminosity functions of 39,000 galaxies in the DEEP2 and COMBO-17 survey was done by Faber et al. (2007) who also separated blue and red galaxies on the basis of their color bimodality. They analyzed the functions at $z < 1$ and verified the fact that the luminosity functions of red and blue galaxies show a different evolution: whereas the blue galaxies are brighter at higher redshift, the absolute magnitudes of red galaxies stays nearly constant. They used a Schechter function with a constant slope α and compared the results of the DEEP2 and the COMBO-17 survey as well as with other surveys and found a good agreement for the total luminosity function in all redshift areas. A comparison between the results by Faber et al. (2007) and the COMBO-17+4 survey can be found in Chapter 6.

Phleps et al. (2007) studied three fields in the COMBO-17 survey and analyzed the effect of dense environments on the luminosity function for galaxies with $R < 23.65$, $z < 0.7$ and $\sigma_z/(1+z) < 0.015$. They concluded that the functions of blue galaxies are unaffected by the environment, whereas the luminosity function of red galaxies differs between dense regions and the normal

field. This change of the function with the environment was already discovered by Phleps and Meisenheimer (2003) in CADIS for galaxies with higher redshifts. The same studies showed that older galaxies seem to be clustered stronger than young ones (Phleps et al., 2006).

1.4.3 Evolution in Mass

Next to the already discussed luminosity functions and color-magnitude diagrams, mass functions are an important tool for the understanding of galaxy evolution. However, stellar masses are more complicated to calculate: common methods are the calculation of the dynamical mass or the estimation of a stellar mass-to-light ratio from SED templates (which is done for the COMBO-17+4 survey, see Chapter 6).

By investigating stellar mass functions we can analyze the mass growth in the blue and the red galaxy population. In the mass-color plane we can also see a bimodality as in the color-magnitude plane. Cassata et al. (2008) proclaim that they have found evidence for the bimodality up to $z = 2$ using masses and $(U - B)$ colors.

The focus of research in the last decade relating to the masses of galaxies has been the red, quiescent and more massive population because this population showed a drastic change in the mass density since $z \sim 2$, whereas the mass density of the blue population stayed almost constant (Borch et al., 2006). How the red galaxies grow in mass so strong is still a matter of debate, as the growth can be explained only up to 50% due to mergers (Brammer et al., 2011). An additional topic of interest regarding the red galaxies is the discovery of red (old) high mass galaxies at $z \sim 2$, which are not expected in our cosmological model, as we are using a bottom up model in which galaxies are growing hierarchically. However, observations indicate that a large fraction of red galaxies with masses $M > 3 \times 10^{11} M_{\odot}$ were already in place at $z > 1$ (Brammer et al., 2011). These galaxies are not only unusual with respect to their mass and color but they also seem to be more compact than modern elliptical galaxies. If these measurements regarding the sizes of these galaxies are trustworthy and how they can get so compact is still a matter of debate (Ferré-Mateu et al., 2012).

1.5 Topic and Questions of this Thesis

In this thesis we present the newest data reduction process of the COMBO-17+4 survey and the results acquired in the two observed fields of Abell 226 and S11, based on a deep H band selected catalog. The use of additional four near-infrared filters in contrast to the COMBO-17 survey allows us to study

galaxy evolution up to a redshift of $z = 2$, whereas the COMBO-17 survey was limited to a redshift of $z < 1.1$. By using the NIR data we are also able to improve the photometric redshift accuracy of objects in the COMBO-17 survey at $z \sim 1$. We are going to divide the galaxy population into a red and a blue population, based on a measured evolving color bimodality. Using this bimodality we will be able to create mass and luminosity functions for different redshift bins in both fields, as well as for the combined COMBO-17+4 survey, for both populations separately. Using these results we are going to investigate the following questions:

- How reliable are the photometric redshift measurements of the detected galaxies?
- Can we find and verify the red sequence beyond $z = 1$ and even up to the limiting redshift of $z = 2$ using color bimodality?
- How does the luminosity function evolve beyond redshift $z = 1$ and can we find differences between the blue and red galaxy population?
- How is the mass of blue and red galaxies evolving from $z = 2$ to $z = 0.2$?
- Can we find massive red galaxies at redshifts $z \approx 2$ and are there only a few of these galaxies, or can we speak of a whole population?

The thesis is organized in the following way: In Chapter 2 we describe the features of the COMBO-17+4 survey and its advantages compared to the COMBO-17 and other multi-wavelength surveys. In Chapter 3 we explain the data reduction process of the near infrared data and how we combine it with the optical data from the COMBO-17 survey. The process of object classification and template fitting is detailed in Chapter 4. Chapter 5 presents the evolution of galaxy bimodality in the redshift range of $0.2 < z < 2.0$. In Chapter 6 we investigate the evolution of the luminosity function and in Chapter 7 we analyze the evolution of galaxy masses and take a look at massive red galaxies at high redshifts. Chapter 8 gives a summary of the thesis and will answer the questions raised in this section.

Chapter 2

The COMBO-17+4 survey

Baum (1962) was the first to use photometric information to deduce the redshift of galaxies. He successfully used 9 filters (ranging from the UV to the NIR) to calculate the the distance of 25 galaxies up to $z = 0.5$. With the use of the COMBO-17 survey and the comparison between the therein measured photometric redshifts for galaxies with known spectroscopic redshift, it was proven that photometric information can also be used to classify galaxies up to $z = 1.1$ and quasars even up to $z \sim 5$ (Wolf et al., 2004).

In this chapter we will discuss the advantages and specifications of the COMBO-17 survey and the subsequent improvements gained with the COMBO-17+4 (Classifying Objects by Medium-Band Observations in 17+4 filters) survey. We will also give information on the telescope, the camera and the four NIR filters, which were part of the survey, along with the conditions experienced during the observation runs. At the end of the chapter we give a short overview of comparable multi-wavelength surveys.

2.1 The COMBO-17 Survey

The COMBO-17 survey is a photometric multi-wavelength survey that combines the data gathered in 17 filters (five broad band and twelve medium band) between 365 nm and 815 nm to calculate photometric redshift for galaxies up to $z = 1.1$. The data were acquired between February 1999 and June 2006 with the 2.2 m telescope at la Silla (Wolf et al., 2003a). The Wide Field Imager (WFI) was used to build up this survey. This detector consists of eight CCD-sensors, each with 2000×4000 pixels. The pixels have a size of $0.238''$ and the detector covers a field of $30' \times 30'$ in total. The goals of the survey were to classify galaxies up to a redshift of $z = 1.1$, to analyze the evolution of the red sequence, to explore weak gravitational lensing, and to investigate the evolution of the luminosity and mass function. In addition, various quasars up to $z = 5$ were

Table 2.1: Coordinates of the three COMBO-17+4 fields.

Field Name	α (2000)	δ (2000)
A901	$09^h56^m17^s$	$-10^\circ01'00''$
A226	$01^h39^m00^s$	$-10^\circ11'00''$
S11	$11^h42^m58^s$	$-01^\circ42'50''$

identified. Due to the comparison of the measured photometric redshifts with spectroscopic redshifts, an accuracy of $\sigma z/(1+z) < 0.01$ for objects brighter than $R < 21$ and $\sigma z/(1+z) < 0.05$ for objects brighter than $R < 24$ was verified (Wolf et al., 2004).

To avoid cosmological variations, five different fields above the galactical plane were observed. Classification of galaxies above $z = 1.1$ was not possible, as only optical filters were used and at least two measured fluxes above the 4000 Å break are needed (next to other features) for a reasonable classification.

First results using the COMBO-17 survey were published by Wolf et al. (2001a). Since then numerous paper on the luminosity and mass functions, weak lensing, active galactic nuclei and the bimodality of galaxies were published(e.g. Gray et al. (2002); Wolf et al. (2003a,b); Bell et al. (2004b); Kleinheinrich et al. (2005)).

2.2 The COMBO-17+4 Survey

The COMBO-17+4 survey can be seen as an extension of the COMBO-17 survey, as it is using the already available optical data and adds additional NIR observations to the survey. Three out of the five observed fields from the COMBO-17 survey were reobserved in the COMBO-17+4 survey. These fields are called Abell 226, Abell 901 and S11. As the observations for the NIR part of the COMBO-17+4 survey were performed on the northern hemisphere at the 3.5 m telescope of the Calar Alto Observatory in Spain, it was not possible to observe the two most southern fields, SPG and CDFS, of the COMBO-17 survey. The central positions of the three observed fields are listed in Table 2.1.

The main reason to extend the COMBO-17 survey with four near infrared filters was to extend the possible object classification from a maximum of $z \approx 1.1$ to $z \approx 2.0$. This combination of 17 optical and 4 near infrared filters also led to the name of the survey. Using the Omega2000 camera observations in the Y, $J1$, $J2$ and H band were made. The central wavelengths, FWHM, lower and upper limits of each NIR filter are listed in Table 2.2. The efficiency of the filters using the WFI and the Omega2000 camera is shown in Figure 2.1. The

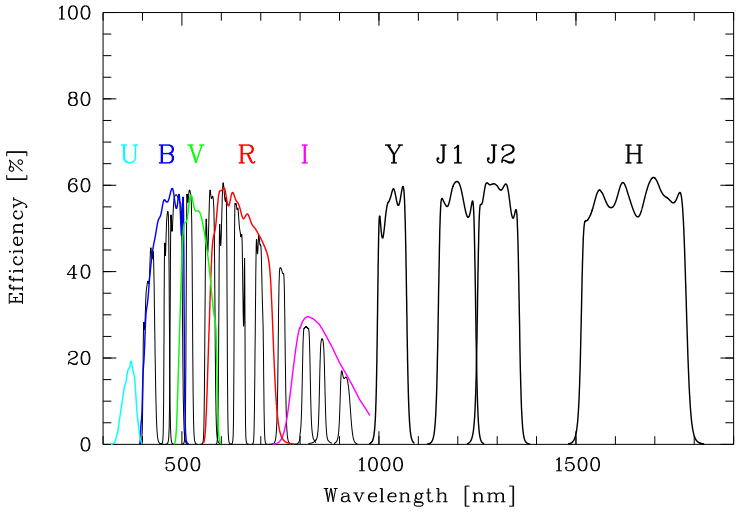

Figure 2.1: The COMBO-17+4 survey filter set. The efficiency of the WFI for the optical filters and the Omega2000 detector for the NIR filters is taken into account. The five optical broad band filters and the four filters in the near infrared are labeled.

filters Y, $J1$ and $J2$ are medium band filters, whereas H is a broad band filter. J1 and J2 represent approximately the lower and upper half of the classical J band filter.

The NIR observations were performed between September 2003 and May 2009 in 24 service runs. Due to losses caused by bad weather conditions, only the Abell 226 field was observed completely. In each of the other two fields, one out of four subfields was not observed. This was a compromise that led to a smaller area that can be analyzed. Yet, the remaining area provides the necessary depth to classify objects up to a redshift of $z = 2.0$.

Each of the observed fields should have covered $30' \times 30'$, which means that the COMBO-17+4 survey was supposed to cover 0.75 square degrees in total. As two subfields – Subfield A in S11 and Subfield D in A901 – were not completed due to bad weather (see also Table 2.3), the total area is reduced to 0.625 square degrees.

2.3 Calar Alto Observatory and Omega2000 camera

The observations for the NIR part of the COMBO-17+4 survey were performed with the 3.5 m telescope at the Calar Alto Observatory, which is the second largest observatory in Europe. The Observatory is located on the Calar Alto mountain (2168 m above sea level) in the Sierra de los Filabres in Almeria, Spain. The coordinates are $37°13'25''N, 2°32'46''W$. The construction of the

observatory started in 1967 by the Max Planck Institute of Astronomy (MPIA) to provide German astronomers with the possibility to work on modern telescopes. Because of the leading position of the MPIA in the construction of the observatory the institute gets a large amount of guaranteed observation time which also was used for the COMBO-17+4 survey. Today the observatory consists out of five telescopes: 3.5 m, 2.2 m, 1.123 m, an 80 cm Schmidt telescope and a 1.52 m telescope operated by Spain. The counterpart of the 2.2 m telescope is located at La Silla, Chile, where the optical data of the COMBO-17 survey was obtained. The median seeing at the Calar Alto observatory is about 0.9 arcsec. The night sky is very dark ($H = 13.99$, $J = 15.95$, $R = 21.36$ and $U = 22.39$), which is comparable to the night sky at La Silla or La Palma (Barrado et al., 2010). During the observations for the COMBO-17+4 survey we encountered very bad weather conditions and only had clear skies for about 16% of the time.

The near infrared camera Omega2000 is mounted on the 3.5 m telescope and had its first light in 2001 (Sánchez et al., 2008). The camera is equipped with three filter wheels in which 17 filters are stored (Baumeister et al., 2003). The detector is HAWAII-2 and it is sensitive from z to K band (i.e. from 850 to 2,500 nm). This 2048×2048 pixel detector has a field of view of $15.4' \times 15.4'$, which leads to a pixel size of 0.45 arcsec / pixel. The physical pixel size is 18 μm. The Omega2000 detector has a negligible field distortion of 0.06%, which is less than 1 pixel from cornor to corner. Since the distortion is negligible, we do not have to take it into account during the data reduction processing. The detector is constructed out of 4 independent quadrants and several different readout modes are possible. For the COMBO-17+4 survey, the Line Interlaced Read (LIR) was chosen. Besides the four infrared filters used for the COMBO-17+4 survey, the instrument has roughly two dozen broad, medium and narrow band filters. For more details on the Omega2000 camera see Kovacs (2006), the Calar Alto Observatory webpage[1] and the Omega2000 manual, which is available there.

Due to the large field of view, the Omega2000 camera is perfect for surveys in the NIR. As well as the COMBO-17+4 survey, it was also used for the the MANOS[2] project. This project was divided into the deep COMBO-17+4 survey and wide HIROCS[3] survey; the latter the was meant to search for high redshift clusters. In both cases the goal was to do a wide field observation of galaxies in the near infrared at high redshifts.

[1] http://www.caha.es/
[2] MPI für Astronomie Near-infrared Optical Surveys
[3] Heidelberg InfraRed Optical Cluster Survey

Table 2.2: Characteristics of the NIR filters used in the COMBO-17+4 survey. Central wavelength, full width at half maximum, upper and lower cut offs of the transmission curve are given.

Filter	Central Wavelength [nm]	FWHM [nm]	lower cut off [nm]	upper cut off [nm]
Y	1034	75	975	1090
J1	1198	95	1122	1267
J2	1302	106	1223	1384
H	1649	266	1480	1826

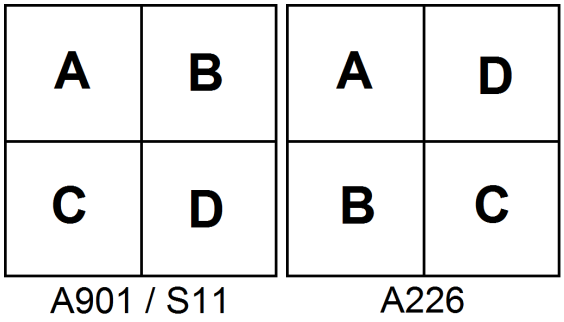

Figure 2.2: Alignment of the four subfields in the three different fields of the COMBO-17+4 survey.

2.4 Observations

As the optical data for the COMBO-17+4 survey was gathered with the Wide-Field Imager at the 2.2 m telescope at La Silla, which covers a field of $30' \times 30'$, the fields had to be divided into four subfields for the Omega2000 camera, which cover only $15.4' \times 15.4'$. The subfields are named A, B, C and D. The positions of these subfields are shown in Figure 2.2: left for Abell 901 and S11 and right for Abell 226.

The individual frames for the same pointings are dithered to avoid information loss due to bad pixels. In addition, as the sky in the infrared is changing on a second timescale, the individual raw-frames are composed of several images. In adding up several images the number of frames which have to be handled is reduced significantly. Frames in the *H* band have an exposure time of 60 seconds and consist out of 20 coadded images. *J*2 frames have an exposure time of 80 seconds and contain 8 coadded frames. *J*1 frames contain 5 coadded images with each 20 seconds exposure time to a total exposure time of 100 seconds. Finally, the *Y* band has an exposure time of 100 seconds and consists out of 10 coadded frames.

The goal of the survey was to reach between 8,000 and 12,000 seconds per subfield and filter. Due to data loss caused by bad weather and reductions

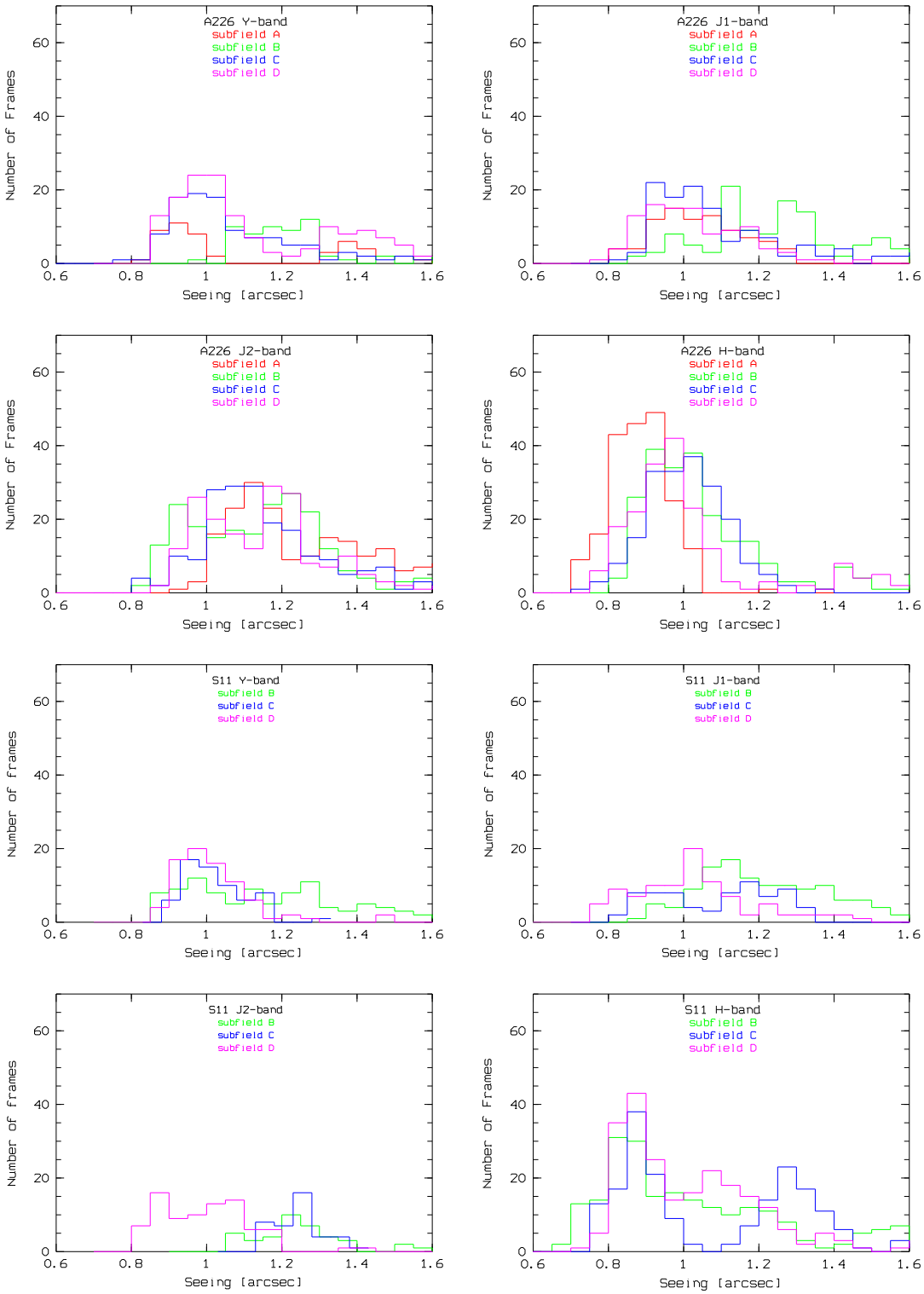

Figure 2.3: The eight panels show the seeing distribution in the four NIR filters and the two analyzed fields. The seeing distribution is divided into the four, respective three, subfields.

Table 2.3: Total integration time in the three fields of COMBO-17+4. The Subfield D of the Abell 901 Field and Subfield A of the S11 Field were never completed and therefore no object detection was done on these Subfields.

Field	Filter	Subfield A [sec]	Subfield B [sec]	Subfield C [sec]	Subfield D [sec]	Goal [sec]
A226	Y	8,000	8,600	8,500	10,200	8,000
	J1	9,000	13,000	12,400	8,100	8,000
	J2	16,800	19,500	14,300	15,300	12,000
	H	13,600	16,800	11,900	14,400	12,000
A901	Y	8,900	5,200	6,400	*1,100*	8,000
	J1	8,600	7,100	8,300	*1,100*	8,000
	J2	7,100	7,400	8,500	*5,300*	12,000
	H	11,800	12,000	11,100	*0,800*	12,000
S11	Y	*0*	9,700	6,400	8,000	8,000
	J1	*4,500*	9,900	4,800	10,200	8,000
	J2	*0*	3,200	3,200	7,000	12,000
	H	*6,000*	20,400	12,000	13,500	12,000

in observation time for the entire project, these goals were not reached for all subfields or all filters. The Abell 226 field was the only one which was observed completely and for which all data was acquired. In Table 2.3 the goals for each filter and the finally acquired data are listed. This table also highlights that observations for the Subfield A in the S11 Field and the Subfield D in the Abell 901 Field have never been completed. Due to the short total exposure time in these subfields, they have been excluded from the further analysis.

The near infrared data of the Abell 901 field was already analyzed by Nicol (2009), whereas the other two fields are analyzed in this thesis. However, we are going to include the results of the Abell 901 field for a complete analysis of the COMBO-17+4 survey.

During our observations a seeing of < 1.50 arcsec was required. An average seeing for each observation run is given in the Tables 2.4 and 2.5. The seeing was varying between 0.83 and 1.68 arcsec in the H band, 0.89 and 1.41 arcsec in the Y band, 0.92 and 1.49 arcsec in the $J1$ band, and 0.94 and 1.78 arcsec in the $J2$ band (see Figure 2.3). See also the Tables 2.4 and 2.5 for the average seeing in each each filter and each observation run. In general, the seeing conditions for all three fields are comparable. For the data analysis images with a seeing greater than 1.5 arcsecs are excluded (see Chapter 3). For a detailed description of the seeing conditions in the Abell 901 field see Nicol (2009).

2.5 Comparable Multi-Wavelength Surveys

As spectroscopic observations are time consuming and restricted to small numbers and bright objects, more and more multi-wavelength photometric surveys were started in the last decade. Most of these surveys only use broad band filters in the optical wavelengths and focus on the galaxy population at $z < 1$. There are a few surveys besides COMBO-17+4 which investigate galaxy evolution up to redshift $z \sim 2.0$:

- The UKIDSS survey, successor of the 2MASS project, consists of 5 subprojects; three of them are used to study extragalactic objects and have limiting magnitudes of $K = 18.4$, $K = 21$ and $K = 23$ and cover areas of 4,000, 35 and 0.77 square degrees respectively. For the different projects in the survey five broad band filters (Z, Y, J, H and K) and two narrow band filters ($H_2 1 - 0S1$ and $Br - g$) were used. The deep extragalactic survey studies the evolution of galaxies in the redshift range of $1.0 < z < 1.5$, whereas the ultra-deep survey has the goal to study the evolution of red galaxies at $z < 3$ (Warren et al., 2006).

- The COSMOS survey covers an area of 2 square degrees and combines data from various observations and instruments. The main data was observed by the Hubble Space Telescope, but the photometric redshifts are calculated using data from the Subaru telescope in Hawaii. The final project contains about 2 million objects brighter than $I > 27$ mag at redshift $z < 2.0$ (Scoville et al., 2007)

- The MUSYC project observes four fields with a total of 1 square degree in six optical filters (U, B, V, R, I and z) and one near infrared filter (either J, H or K). In addition they observe four smaller subfields in their fields to greater depths, in which observations are done in all three NIR filters. For these subfields (the so called MYSIC deep) they use a K band selected catalog of galaxies to study their luminosity functions, mass functions and clustering in a redshift range of $2 < z < 3.5$ (Quadri et al., 2007).

- The FIREWORKS survey covers an area of 138 arcmin^2 and use 16 different filters for observation. The objects which are detected in this survey reach up to a redshift of $z \approx 4$ (Wuyts et al., 2008).

- The NEWFIRM survey was inspired by the COMBO-17 survey and combines medium-band optical filters with five filters in the near infrared. The project is able to study the evolution of galaxies in the redshift range $z < 2.2$ and covers a field of 27.6×27.6 arcmin. With the filterset used, the size of the field which was observed and the classification reaching a redshift of $z \approx 2.0$ this survey is a direct competitor of the COMBO-17+4 survey. Like in the COMBO-17+4 survey the objects in the NEWFIRM

survey are separated into two populations (a red and a blue one) and masses / mass-functions are calculated (Brammer et al., 2011). As both surveys are so similar we will be able to compare their results directly with these of the COMBO-17+4 survey.

Table 2.4: Summary of the Abell 226 field observation runs including information on the average seeing and the total integration time achieved.

Subfield	Filter	Date of Observation	Integration time [sec]	Seeing [arcsec]	Campaign Name
A226 A	Y	August 2007	4800	1.41	256b
	Y	December 2007	1600	0.89	256d
	Y	October 2007	1600	0.97	256c
	J1	December 2006	6400	0.98	250
	J1	December 2007	1800	1.18	256e
	J1	October 2007	1800	1.16	256c
	J2	October 2006	6400	1.12	248
	J2	December 2007	3440	1.40	256d
	J2	December 2007	3200	1.40	256e
	J2	October 2007	3840	1.44	256c
	H	November 2003	2940	0.90	207
	H	September 2003	3120	0.85	205
	H	September 2004	7560	0.90	220
A226 B	Y	October 2005	2500	1.23	238
	Y	December 2007	2000	1.32	256d
	Y	October 2007	1600	1.09	256c
	J1	October 2005	5800	1.37	238
	J1	December 2006	1800	0.99	250
	J1	December 2007	3600	1.14	256e
	J1	October 2007	1800	1.26	256c
	J2	October 2005	1600	1.78	238
	J2	December 2006	1600	1.02	250
	J2	October 2006	6400	1.00	248
	J2	December 2007	3520	1.33	256d
	J2	December 2007	1600	1.33	256e
	J2	October 2007	4800	1.21	256c
	H	November 2003	4860	1.20	207
	H	September 2003	3000	1.01	205
	H	September 2004	7500	0.97	220
	H	August 2007	1500	1.68	256b
A226 C	Y	September 2004	4440	0.98	220
	Y	December 2007	4000	1.30	256d
	J1	September 2004	1560	0.94	220
	J1	August 2007	2900	1.14	256b
	J1	December 2007	1800	1.09	256d
	J1	October 2007	3600	1.49	256c
	J2	September 2004	4500	1.09	220
	J2	October 2006	1600	1.36	248
	J2	December 2007	3520	1.17	256e

Table 2.4: Summary of the Abell 226 field observation runs including information on the average seeing and the total integration time achieved. (continued).

Subfield	Filter	Date of Observation	Integration time [sec]	Seeing [arcsec]	Campaign Name
	J2	December 2007	1520	1.17	256d
	J2	October 2007	3200	1.12	256c
	H	November 2003	2940	1.05	207
	H	September 2003	3000	0.91	205
	H	September 2004	4500	1.01	220
	H	August 2007	1500	1.10	256b
A226 D	Y	September 2004	6600	1.01	220
	Y	August 2007	1600	1.57	256b
	Y	December 2007	1800	1.27	256e
	Y	December 2007	3200	1.27	256d
	J1	November 2003	3000	1.11	207
	J1	September 2004	1500	1.14	220
	J1	December 2007	1800	1.07	256d
	J1	October 2007	1800	0.92	256c
	J2	September 2004	4500	1.22	220
	J2	December 2006	1680	0.95	250
	J2	December 2007	4000	1.16	256e
	J2	December 2007	3600	1.16	256d
	J2	October 2007	1600	1.21	256c
	H	November 2003	2940	1.00	207
	H	September 2003	3360	0.92	205
	H	September 2004	6600	1.00	220
	H	August 2007	1500	1.47	256b

Table 2.5: Summary of the S11 field observation runs including information on the average seeing and the total integration time achieved.

Subfield	Filter	Date of Observation	Integration time [sec]	Seeing [arcsec]	Campaign Name
S11 A	J1	April 2004	4500	1.52	213
	H	April 2004	3000	1.56	213
	H	February 2009	3000	1.25	261
S11 B	Y	April 2008	1600	1.23	257d
	Y	May 2008	3200	1.38	257e
	Y	April 2009	1600	1.09	257d
	Y	March 2009	3300	0.95	262
	J1	April 2004	4500	1.28	213
	J1	May 2008	1800	1.49	257e
	J1	April 2009	3600	1.05	263
	J1	May 2008	1800	1.49	257e
	J2	March 2009	3200	1.26	262
	H	April 2004	4500	1.11	213
	H	February 2008	2460	0.86	257b
	H	March 2008	1500	0.84	257c
	H	February 2009	7500	1.23	261
	H	March 2009	4500	0.83	262
S11 C	Y	April 2008	1600	1.10	257d
	Y	April 2009	4800	1.00	263
	J1	April 2004	3000	1.01	213
	J2	March 2009	3200	1.25	262
	H	April 2004	3000	1.35	213
	H	April 2008	3000	1.32	257d
	H	February 2008	1200	0.91	257b
	H	March 2008	1800	0.93	257c
	H	March 2009	3000	0.84	262
S11 D	Y	April 2008	3200	0.98	257d
	Y	April 2009	4800	1.04	263
	J1	April 2004	3000	0.93	213
	J1	May 2009	8500	1.13	264
	J2	April 2004	3000	0.94	213
	J2	March 2009	3200	1.06	262
	H	April 2004	6000	0.98	213
	H	April 2008	1500	1.25	257d
	H	March 2008	3000	1.27	257c
	H	February 2009	1500	1.03	261
	H	March 2009	1500	0.83	262

Chapter 3

Data Reduction of the COMBO-17+4 Survey

The observed data from the COMBO-17+4 survey is reduced mainly using the MPIAPHOT package within the MIDAS[1] software. The MPIAPHOT package was developed by Meisenheimer and Roeser (1987) and has already been used for the data reduction of CADIS and the COMBO-17 survey. For the modeling of the sky background, flatfielding and dark subtraction the OMEGA2k pipeline by Fassbender (2003) is used. Object detection is performed with the Source Extractor program by Bertin and Arnouts (1996).

This chapter gives an overview of the individual steps in the data reduction process. A detailed step by step explanation, showing all the commands used can be found in Appendix B. Detailed explanations for the used commands can be found in the MPIAPHOT manual[2]. For the data reduction we use the same sequence of commands as Nicol (2009) for the reduction of the Abell 901 field.

3.1 Preparation for the Data Reduction

Since most of the data reduction is done in the MIDAS environment using the MPIAPHOT pipeline, the raw data has to be changed from the regular *.fits format to the MIDAS internal *.bdf format. In addition, the names of the individual images have to be adapted to the internal name convention of MANOS, which consists of three four-character long blocks. The first block gives information on the type of the image (raw_, dome, flat), the second gives the year and month of the observation and the last one is a consecutive number. The two number blocks do not change during the reduction process.

[1] Munich Image Data Analysis System

[2] http://www.mpia.de/HIROCS/mpiaphot.pdf

As the NIR observations for the COMBO-17+4 survey were done within five years, some names of the descriptors in the headers of the images changed during that time period. Before any other commands are used, the descriptors that store the observation date and the exposure time have to be updated to the current format, otherwise the information stored therein will be lost.

In addition, MPIAPHOT needs new descriptors included in the image header. The descriptor *epsilist* contains information on the optics, the detector and the filter used. The descriptor *lambda* also has to be added. This descriptor contains information about the central wavelength, the FWHM of the filter used and the lower and upper wavelength limits of the transmission curve.

3.2 Dark Current

Normally, the first step in the reduction process of astronomical data is the subtraction of the dark current, which is influencing every singe raw image. Dark current occurs due to thermal motion of the electrons in the detector. Therefore the amount of dark current can be reduced by cooling down the detector. The OMEGA2k detector is cooled to 78 K, which reduces the dark current to $< 0.03 e^{-}/sec$ (Fassbender, 2003). This low count rate at low temperatures, combined with an integration times in the NIR of only a few seconds, leads to a very low amount of dark current in the raw images. Still, these electrons contaminate the images and should normally be subtracted using dark images.

In the data reduction process of the COMBO-17+4 survey, the dark current is subtracted with the sky background in the OMEGA2k data reduction process, and therefore no specific dark current files have to be created.

3.3 Bad Pixel Masks

There are two types of bad pixels present in the OMEGA2k detector: (1) dead pixels, which do not detect incident radiation and (2) hot pixels, which accumulate charge even in the absence of incident radiation. To mark dead pixels on the individual science images, bad pixel masks (BPMs) have to be created for each observation run in the survey. It is necessary to have an individual BPM for each run, as the number of dead pixels can change each time the the camera is removed from the telescope or simply due to detector degeneration over time.

It is known that about 1% of all pixels on the OMEGA2000 detector have to be flagged as bad pixels (Fassbender, 2003). This means that about 1% of all pixels cannot be used, as they do not accurately record the number of photons

hitting them. To correct for this loss of information in the individual images, the bad pixels are replaced with a median value.

To identify the bad pixels, we use dome flat images with different exposure times. Care has to be taken that non of these images exceeds a count of 30,000 photons per pixel (which is reached with an integration time of about 100 seconds). Above this limit, the detector no longer reacts linearly to incident photons. Images with a higher count rate have been removed.

Since dome flats are not available for all observation runs and all observed filters, we sometimes have to use BPMs from other runs. We make sure that we always use BPMs from later runs, since the possibility that a pixel becomes dead is higher than the possibility that a dead pixel starts to working correctly again.

Three different techniques are combined to identify the bad pixels from the dome flats: We plot a linear fit for every single detector pixel through our selected stack of dome flat frames. This fitting gives a slope, a constant and root mean square (RMS) value for each pixel (see Figure 3.1). All three of these values are used to identify bad pixels on the frames.

First, we flag all pixels which have a slope value deviating by more then 3 σ from the mean slope value as bad pixels. The only exception to this is the bad pixel mask for the September 2003 run, where we use a 5 σ value, as the slope value distribution is broader than usual. This method allows us to identify pixels whose sensitivity curve is different from the average. On average roughly 5,500 bad pixels are identified this way.

The second criteria for bad pixel selection is the RMS of the fit. Again, pixels whose fit RMS is greater than 5 σ are flagged as bad pixels. Pixels which are flagged this way behave very non linear. Roughly 1,200 bad pixels are identified using this method.

As a third method, we flag all pixels whose fit gives a constant value 3 σ higher or lower than the mean constant value. Flagged pixels have a large offset from the common zero point. This means that pixels with a lower value are bad pixels, whereas pixels with a higher value are hot pixels. We find about 22,000 dead pixels this way, which makes it by far the most efficient method to detect dead pixels.

To create the final bad pixel mask, the bad pixels identified with all three methods are combined. After normalizing, the final bad pixel mask images show either a value of one (bad pixel) or zero (good pixel). Within the 13 created BPMs, an average of 27,400 bad pixel are flagged, which corresponds to $\approx$ 0.7% of all detector pixels. This is in a good agreement with previous results. The BPM created for the run in August 2007 is shown in Figure 3.2.

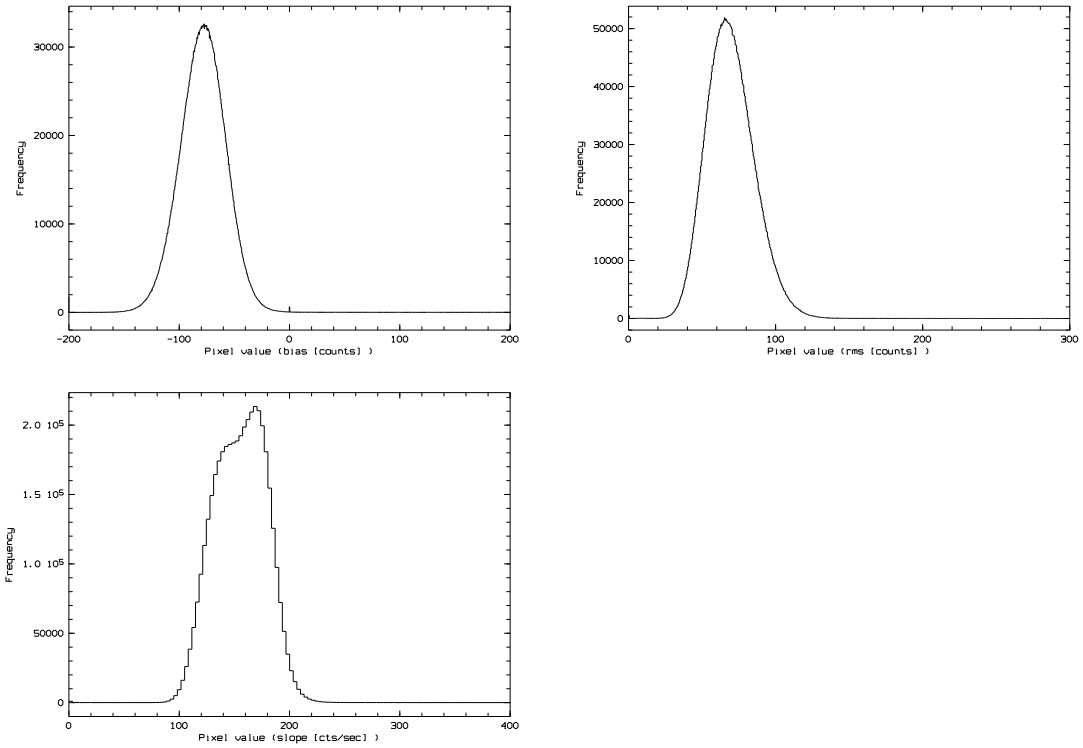

Figure 3.1: The three plots are used to identify bad pixel on the dome flats. The upper left graph shows the distribution of the constant values, the upper right graph shows the RMS values and the lower graph shows the slope value.

3.4 Flatfield Correction

After the bad pixels are flagged, the images are corrected for instrument response variations using flatfield images. Flatfields are needed to compensate pixel-to-pixel sensitivity variations and a global non homogeneous sensitivity of the detector and the optical system, as well as to find contamination on the detector, the lenses and on the used filter. The pixel-to-pixel variation shows fixed patterns on the detector and is therefore also called fixed pattern noise (FPN). The FPN results from impurities on the pixels. The overall inhomogeneity of the detector on the other hand is caused by an inhomogeneous thickness of the photometric layer of the detector. Therefore, the detector is more sensitive in one area than in another. These contaminations can be found in every detector.

All these effects are multiplicative, which means that the raw image has to be divided by the final flatfield to remove all of these effects. Flatfields can be created in two ways: either a series of dome images are taken, in which case an area in the dome is illuminated homogeneously, or a series of sky images are taken. In the latter case, the images are taken either at dusk, shortly after

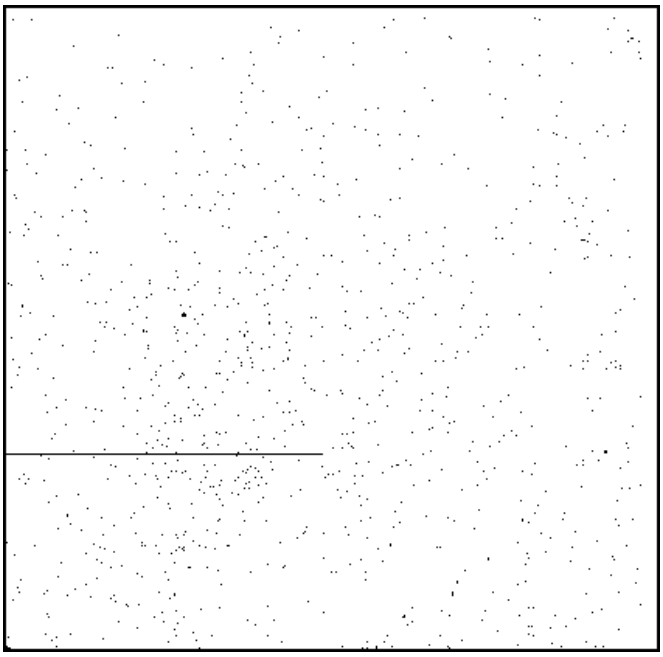

Figure 3.2: An example of a bad pixel mask for the OMEGA2k detector from the August 2007 run. Bad pixels are shown in black, whereas good pixels are shown in white. A significant line of bad pixels can be seen in the left bottom quadrant of the frame. As this line is easy to recognize with the naked eye, it can be used for a fast inspection on the quality of the BPM. For a better presentation a black border was added around the frame.

sunset, but before stars can be seen, or at dawn, shortly before the sun rises. In this twilight the sky can be assumed to be illuminated uniformly, so that flatfield images can be taken. For the reduction of the COMBO-17+4 survey both dusk and dawn images are used.

As the flatfields depend on the wavelength and the contamination in the optical system, they can change over time. Therefore, individual flatfiels are created for every run and every filter. Due to the fact that flatfield images were not taken for every filter in every run, flatfields for some runs are created from science images. In this case, it is important to ensure that a large dithering of at least 20 arcseconds between the used images exists, so that no bright stars from the science images can influence the final flatfield.

Flatfields at the telescope are taken using the OMEGA2k acquisition software, which maximizes the number of sky flats taken during the usable twilight time at dusk and dawn. The program calculates the background level and adapts the exposure time to the changing light conditions during sunset / sunrise. This ensures that a constant count level of roughly 15,000 counts is maintained. If the exposure times get either too long or too short the program stops automatically.

The MPIAPHOT routine FLAT/CATALYST is used to create a master-flatfield image out of the individual flatfield images. This routine needs a normalized dome flat of the corresponding filter as input. This normalized dome flat contains only the FPN and is divided through the flatfield. This way the noise of the individual frames is reduced. A κ-threshold value of 5 σ is used to remove faint stars that otherwise will be seen on the final flatfield. In addition, a diameter of a median-filter box of 3 pixels is given. These values are the default ones given by the routine. After the removal of the stars, the FPN is multiplied again with the flatfield to maintain the count rate. At the end, the flatfield image is divided by its median value to get a normalized flatfield.

A careful creation of the individual flatfields is necessary, as suboptimal flatfields will lead to incorrect flux measurements for the individual objects in the science frames. The quality of the flatfield can only be verified after the images are completely reduced and the fluxes are calibrated. If a corrupt flatfield is identified, the whole data reduction process for the run using this flatfield has to be redone. The flatfield now contains the pixel-to-pixel sensitivity variation of the detector and the mirror contaminations. However, there is one additional contamination that has to be removed from the flatfield images before they can be used in the data reduction process.

3.4.1 Correction of the reflection

A known problem with the OMEGA2k instrument is the spurious reflection from the detector baffle which contaminates all images. This reflection leads to a roughly circular illumination pattern on the detector, whose center is aligned with the center of the detector. The origin of the reflection is still not completely understood but with a high probability comes from reflected light by one of the interference filters which finds its way on the detector.

Nicol (2009) discovered that there is no relation between the intensity of the reflection and the wavelength of the filter used but there seems to be a connection with the optical surface of the interference filters. Nicol (2009) also measured that the reflection is most intense in the $J2$ filter, where it adds 10% to the total measured flux. In the filters $J1$ and Y the contribution of the reflection is at a 5% level. Only in the H filter the reflection is negligible, as it only contributes 0.5% to the total flux, nevertheless the reflection is still visible.

In the individual science images, the reflection can be ignored as the photometry routines will subtract it as a background contribution. This is not the case with the flatfield frames, where more processing is required. Therefore the reflection pattern has to be subtracted from the normalized master-flatfields in the $J1$, $J2$ and Y filter, as the reflection is an additive effect. Failure to correctly account for this reflection in the master-flatfields will contaminate the science

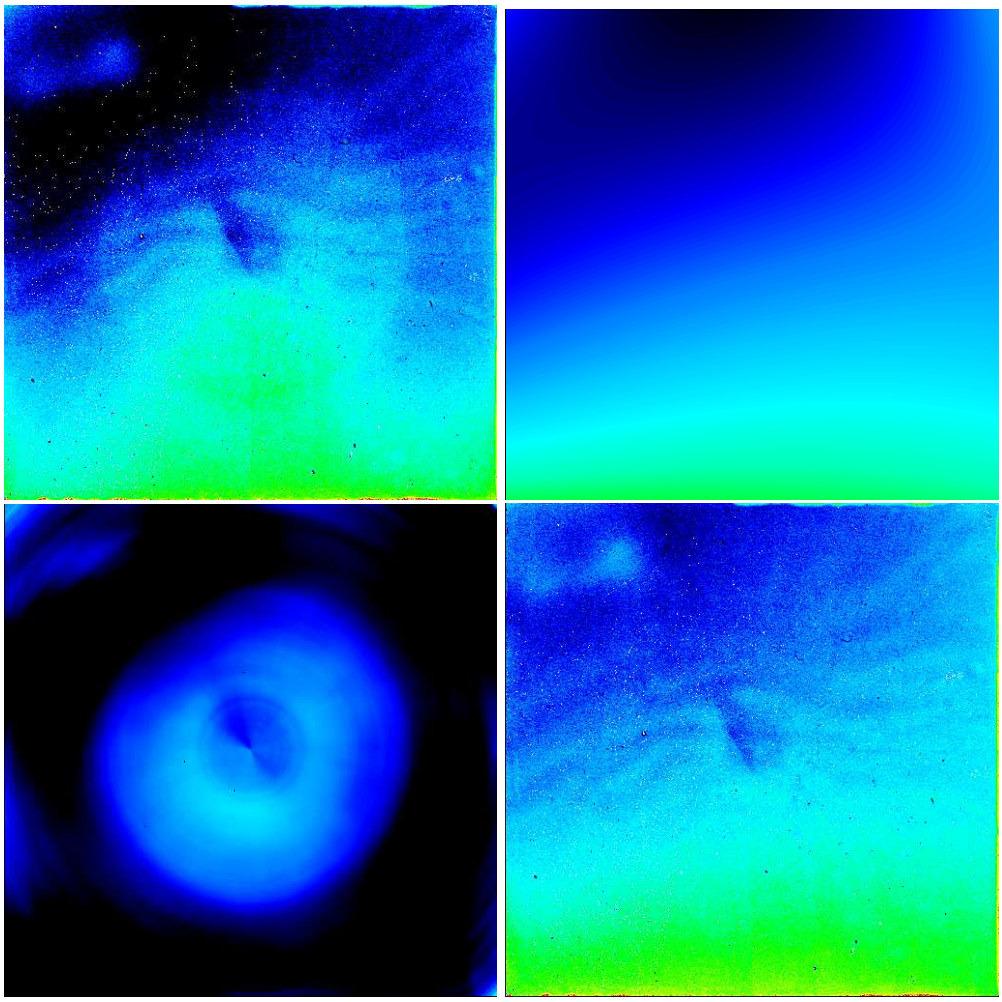

Figure 3.3: The upper left image shows an example of a flatfield from the *J*2 band, before the correction of the reflection from the detector baffle. The image in the upper right shows the calculated background from the flatfield. The lower left image shows the ring model, which is calculated on the basis of this background. The image in the lower right shows the final corrected flatfield.

images, as we are dividing the science images by the flatfields.

To subtract the ring from the flatfield, the ring first has to be identified. In the routine FIT/FLAT, the area around the ring is flagged manually, so that a model of the background can be created. The original image is then divided by the background image, which separates the ring from the background.

The routine FIND/RING then models the ring by transforming the image from Cartesian coordinates to polar coordinates. The routine also allows the user to specify a center for the ring, which in the case of the OMEGA2k instrument is always the middle of the image. Within the routine, the image is both smoothed and interpolated in Cartesian coordinates. The output image

of the routine contains a model of the ring. This ring model is multiplied with the background model to recover the varying sensitivity over the ring. This final ring model is subtracted from the original flatfield and thus the ring is removed. The different reduction steps of the reflection can be seen in Figure 3.3.

Like with the *H* band flatfields, the ring-corrected flatfields in the *J*1, *J*2 and *Y* bands are then divided by their median, to normalize them. The images are checked visually during the individual correction steps and at the end to verify the accuracy of the reduction process.

With all flatfields created, reflection corrected and normalized, the next reduction step of the science images can be done.

3.5 OMEGA2k Reduction Pipeline

The flatfield correction and the sky background subtraction is performed using the OMEAG2k pipeline developed by Fassbender (2003). The pipeline is used as part of the online data reduction at the Calar Alto Observatory. A fast data reduction during the observation runs is necessary, as the observed sources are not visible in the raw science images due to their low S/N and the high sky background in the NIR. With a near real time reduction pipeline, the observer is able to verify the pointing position of the telescope accurately, assess the image quality and instrument performance and check the limiting magnitude of his science frames.

The OMEGA2k pipeline subtracts the dark frame, divides by the flatfield, corrects bad pixels and models the sky (which is then subtracted) in three steps:

In the first step, every frame of the input list is calibrated. This means that the dark current is subtracted first. As already mentioned above, we are only using a dummy dark frame, which is needed for the pipeline, whereas the real dark is subtracted with the background in the second reduction step. Then the frames are flatfielded and the information from the BPMs is used to replace bad pixels on the flatfields with a median value.

The sky is subtracted in the second step. To save valuable observation time, no sky frames are taken and therefore the sky is directly measured on the science frames. This is very useful, as the sky in the NIR is changing quickly. To get the information on the sky background, a stack of normalized and dithered images (for our reduction scheme we always used a stack of 5 frames) is loaded. Frames taken before and after the chosen main frame are loaded in the stack. The actual sky modeling is then done for each pixel individually: The values of one pixel are loaded, sorted and rearranged in an

ascending order. As we are using the outlier-clipping method, which leads to the best results, we can identify stellar outliers on the pixels and exclude them from the sky determination process. Pixels with a value of 3 σ above the median background are, in our case, counted as astronomical objects (or hot pixels) and not used for the sky modeling. This way the sky is determined individually for each pixel. As soon as the sky for one frame is determined a new stack of frames is loaded and the reduction process starts again.

In the third step, a second iteration is performed to improve the background subtraction. This is required, as the dither step is not sufficiently large to transverse large objects such as extended galaxies and bright stars. This step also removes cosmic rays. Again a stack of images is loaded (this time 9 frames), but this time a mask of all objects having a 1.5 σ above the treshold is created. The frames are then aligned and again the value for each pixel is measured and a second iteration for the sky model can be done. In addition, pixels with 5 σ above the normal background level are flagged as cosmics and replaced by a median value. Due to the dithering of the images, the correction for cosmics can only be done in the center of the frames. Therefore a second cosmic removal using a mosaic median frame is necessary.

At the end of the pipeline procedure, the mean count level of the background is added to the science frames to preserve the flux level.

It has to be mentioned that the pipeline is a black box with about 30 internal parameters that cannot be changed by the user. In addition some steps in the pipeline are not explained very well and it occurred more than once that the pipeline stopped in the middle of the reduction process or the output was obviously wrong. It helped to exclude individual frames, even though they did not seem to have any obvious problems or to change the order of the frames in the stack of images.

3.6 Quadrant Structure Correction

The Omega2000 camera is constructed out of four quadrants, which are read out independently from each other. Due to this construction, and the special read out procedure of the sensor, it is possible that the quadrant structure becomes visible in the science frames (see Figure 3.4). This occurs mainly due to diffuse clouds that are passing through the field of view and therefore the structure appears more often on images using the H or $J2$ band filters, which are both more sensitive to water vapor. As the observations were made during very good weather conditions, and as only low clouds lead to a visible structure, the number of affected frames is very low.

Nevertheless, the structure must be removed to perform accurate photo-

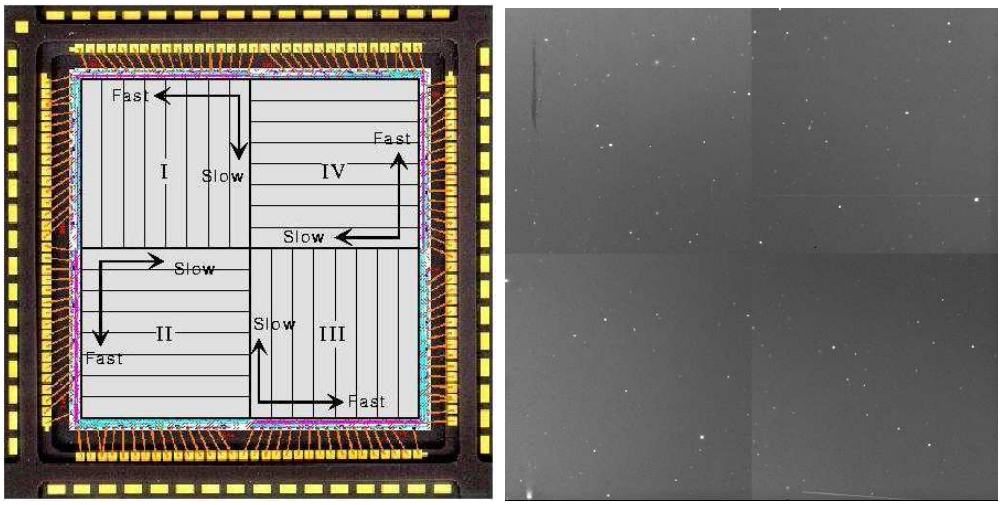

Figure 3.4: The left image shows the electronic structure of the Omega2000 detector including the read out directions (Kovacs, 2006). The four independent quadrants of the detector can also be visible on the science frames, like in the right image, under the correct circumstances.

metric measurements. For this we use a procedure in the MPIAPHOT environment that flattens and subtracts the background. This procedure is normally done before the activation of the OMEGA2k pipeline, but if all images of the run to be analyzed show the quadrant structure it can also be done after the OMEGA2k pipeline processing. Tests done with COMBO17+4 data show that both procedures lead to the same results. For the data of the Abell 226 field and the S11 field the quadrant structure correction is performed after the OMEGA2k pipeline processing. However, the data for the Abell 901 field, which was reduced by Nicol (2009), the correction was done before the pipeline processing.

An image whose quadrant structure is flattend normally only has a variation of less than 1% between the four quadrants left. However, there are a couple of frames in which the structure is so strong that flattening of the background is not sufficient to get rid of the structure. These frames are excluded before the reduction process proceeds. Before the next reduction step, the images are converted from counts to electrons. Afterwards the coordinates of the individual images are converted from pixel values into arcseconds.

3.7 Gnomonic Projections

The flat fielded and sky subtracted images still contain bad pixels and cosmic rays. Bad pixels were already identified with the BPM, and cosmic rays by the OMEGA2k reduction pipeline. However, the latter is not able to identify

cosmic rays at the edges of the individual frames.

To do so, a mosaic median image using the corrected science images have to be created for each of the four filters. A median image is used because the different pointings of the individual images lead to an overlap of the subfields, by which we are able to identify cosmics at the edges of the individual frames.

Before we can create a mosaic median image, the corrected images have to be shifted towards a common coordinate system. We use the 2MASS catalog for this purpose. The brightest objects on each image are tagged and these objects are identified in the 2MASS catalog. Images with too few bright objects have to be excluded from our data the 2MASS catalog cannot find enough reference objects to calculate a correct shift.

The now shifted images, with a common coordinate system, are rebinned into a gnomonic projection. The gnomonic projection projects all frames directly on the sky, with the identified stars in the 2MASS catalog used as references. The projection has an accuracy of $\leq$ 0.1 arcsec. With the accurate information about the position of the stars (and therefore also the position of the individual frames) we are able to create a mosaic image, which covers all observed subfields. For the median image, a mean value for each pixel (for which at least four images are available) is calculated. As the individual images are dithered, the outer borders of the mosaic are not always covered by at least four individual images. Pixels in this areas of the median mosaic image are automatically flagged by the routine and not used for further photometry.

The median mosaic image is also used for a correction of the bad pixels and cosmic rays. In addition, the mosaic median image and the automatically created mosaic RMS image can be used for an additional check to see if a gradient is visible over the mosaic (which would be the result of a bad flatfield) or if other substructures are visible (due to bad images or a wrong correction of single images).

3.8 Removing Bad Pixels and Cosmic Rays

The mosaic median image has to be used to remove the bad pixels and cosmics. Each pixel on every single gnomonic projected image is compared with the value of the same pixel in the median mosaic image. If the value of the pixel on the gnomonic projected images deviates by more than 5 σ, this pixel is flagged as a cosmic.

In a second iteration, the pixels subjected to cosmics are analyzed. If their value deviated by 2.5 σ or more from the median value they are also flagged as cosmics. The combined information of both iterations is then stored in a cosmic mask that is created for each science image.

Table 3.1: The number of frames used to create the summed images for A226 and S11 respectively. The exposure time for the subfield with the shortest exposure time in each field and the seeing in arcseconds for both fields are also reported. Our numbers are compared with the number of images used for the deep *H* band image of A901. The number of frames used for S11 and A901 are lower as both fields consist of only three subfields. The lower seeing in both new fields was reached by using single images, whereas for the A901 summed-up images were used.

Field	# frames	exposure time	seeing
A226	820	11,280 sec	0.93″
S11	651	11,580 sec	0.98″
A901	720	11,160 sec	1.03″

Now that the information on the position of bad pixels (which is stored in the BPM) and the cosmics is available, the values in the contaminated pixels can be replaced by the median value from the mosaic median image. This information is applied on the original, non-gnomonic, quadrant-structure corrected images.

Now the images are fully reduced and available for photometry.

3.9 Master Object Catalog

To create a master catalog that contains all the objects we want to analyze and do photometry on, a deep *H* band mosaic image has to be created out of gnomonic projected frames. This deep sky image contains all reduced images from all pointings.

The deep sky image is a weighted sum image in which the gnomonic frames from the input catalog are weighted according to their depth:

$$\text{weight} = \frac{1}{(\text{transmission}) \times (\text{background-noise})^2 \times \text{PSF}^2} \tag{3.1}$$

The number of images used to create the summed-up images for A226 and S11, the total exposure times and the seeing are listed in Table 3.1. As a comparison, the results of the summed-up images from the A901 field are given.

The summed-up mosaic images of A226 and S11 can be seen in the Figures 3.5 and 3.6. Clearly visible are the edges at the outer borders where, due to dithering, only a few frames have been summed-up and therefore the summed image does not reach the necessary depth to measure photometric fluxes of the interesting objects.

The software Source Extractor[3] by Bertin and Arnouts (1996) is used to find sources on the deep H band image. During the work on the Abell 901 field, using the data by Nicol (2009), Wolf (priv. communication) discovered that the standard parameters used for the analysis of this field are not optimized to find faint objects on the summed image. With the use of the standard parameters, the program identified variations in the background as real sources that are then contaminating the faint population of galaxies and stars.

Therefore, we performed a parameter study to improve the detection of faint objects and simultaneously reduce the amount of falsely identified sources. The most important parameter identified is the threshold in units of signal-to-noise ratio. As the standard value of 4.7 leads to many spurious objects, we increase the value up to 5.5. In addition, the minimum amount of connected pixels needed to lead to the detection of an object increased according to the seeing of the images.

Unfortunately, the first version of this so called master catalog still contains artifacts and sources that cannot be used for photometry. Especially objects in the border region of the summed images and objects around bright stars have to be excluded. For this we use two new routines:

Firstly, the borders of the summed images are cut using the world coordinates of the summed images. This way, objects that do not have the necessary depth for a useful photometry are excluded. Secondly, objects around bright stars, whose photometry will be contaminated by the star, are excluded. Therefore, all objects with a Source Extractor internal value of mag0 = 12 or lower are selected[4]. Then all objects within a radius of 20 arcseconds of the selected objects are flagged as contaminated objects. This contaminating radius is reduced by 6 arcseconds per magnitude down to a minimal radius of 5 arcseconds. This excludes all objects within the halos of the bright stars without loosing too much area in the observed field. The surface area of the entire cleaned area is calculated and saved in a descriptor. This number has to be subtracted from the total observed area as soon as we start to analyze the evolution of galaxies in a cosmological context, as it otherwise will lead to wrong calculations.

As a last update of the master catalog, extremely elongated objects in the catalog are flagged. These objects are mainly artifacts created by satellites and diffraction spikes from bright stars. Elongated objects are defined by a longitudinal axis of 10 arcseconds or larger, a flag number by SExtractor of 3 or larger and a ratio between longitudinal and transversal axis of at least 3.

All flagged objects are excluded from the original master catalog. The re-

[3]also known as SExtractor or SEx

[4]mag0 does not represent real magnitudes, as no proper zero point is available for the Sourece Extractor

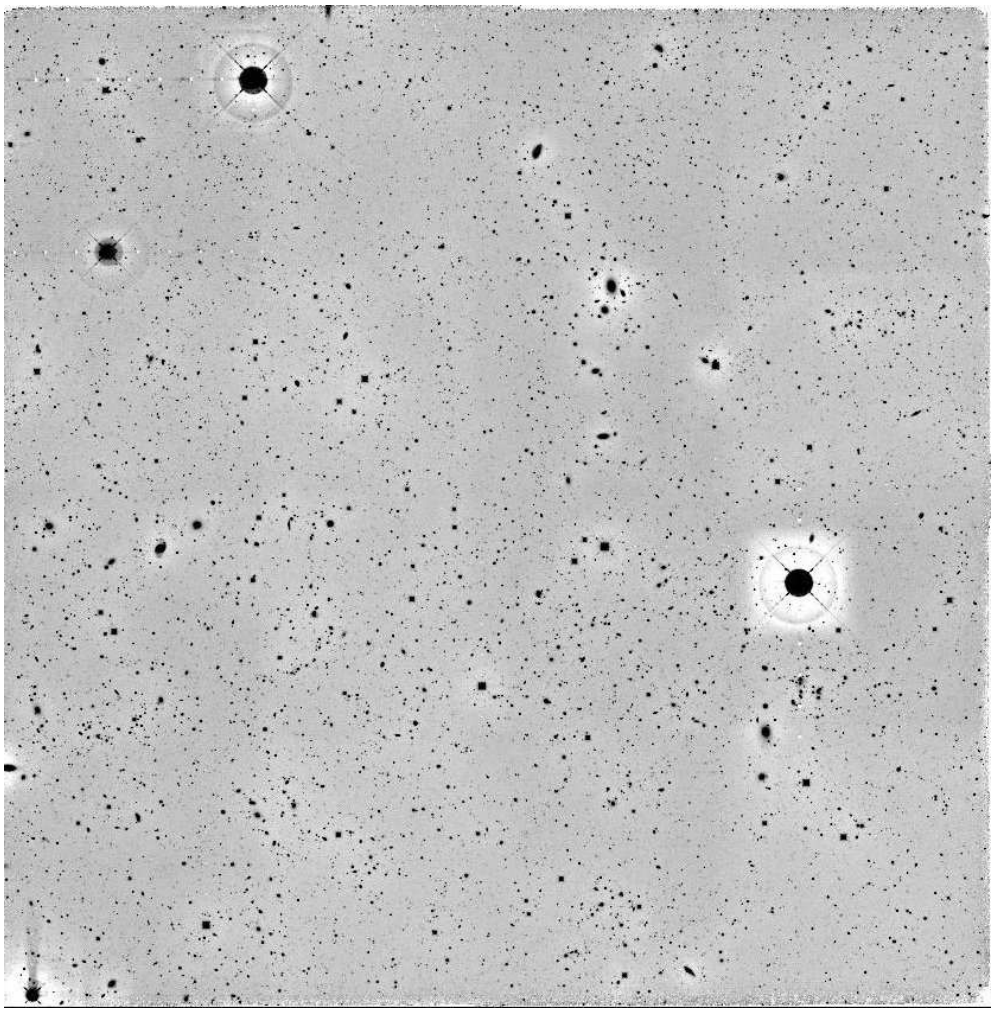

Figure 3.5: The combined mosaic image of the Abell 226 field in the *H* band.

maining objects are saved in the final master catalog. This master catalog contains a coordinate system that projects the objects on the celestial sphere, as well as the pixel coordinates of the objects, world coordinates and right ascension and declination. The latter are available due to the shifting done with the individual images according to the 2MASS catalog. For all further photometry the positions of these objects are used.

3.10 Summing-up Images

For the NIR part of the COMBO-17+4 survey, several hundred images in each filter and for each pointing are taken. Due to the large number of frames MIDAS is not able to handle all of them in the MIDAS internal table format. Therefore, we are forced to sum-up individual images to reduce the overall

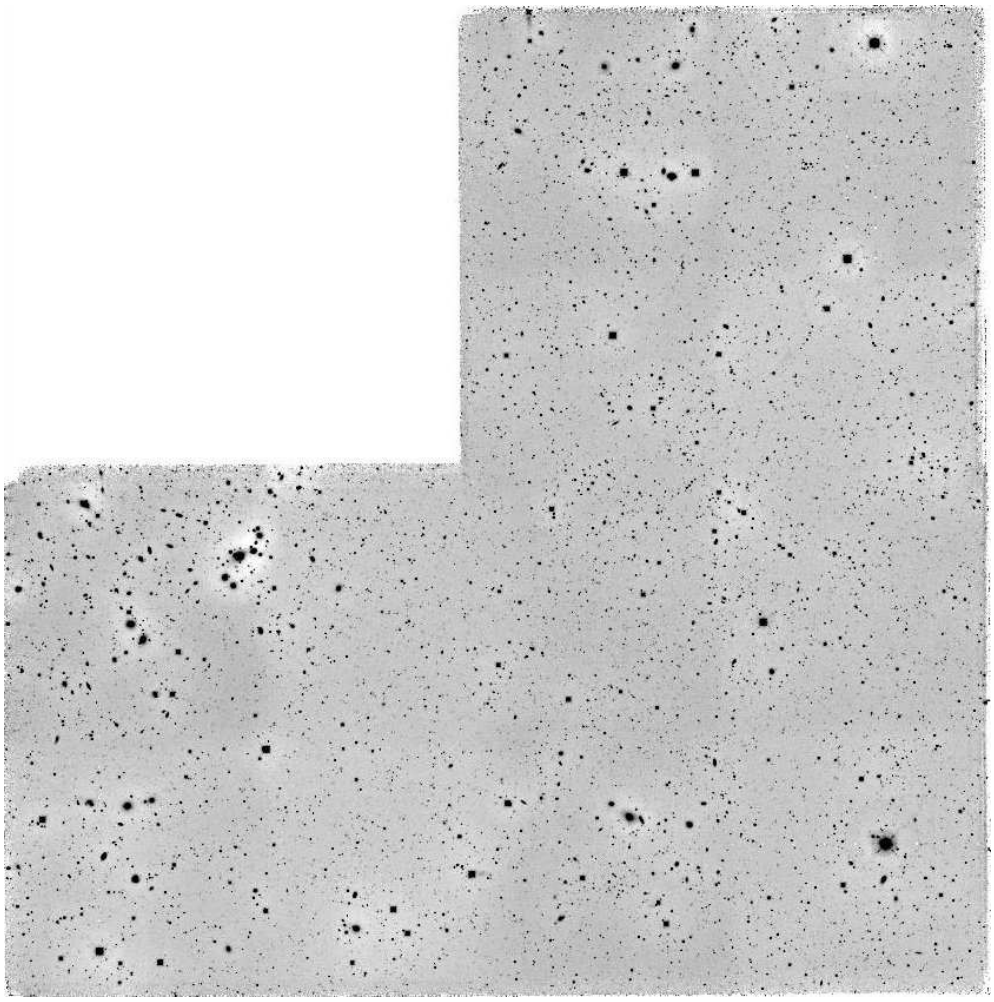

Figure 3.6: The combined mosaic image of the S11 field in the H band. Since the subfield A was not observed completely in all filters in the near infrared, it was excluded from the object detection.

number.

Ideally photometry should be done on individual images, as it leads the best results and the stacking of images leads to a reduction in photometric accuracy and to a larger seeing. This means that we want to sum-up as few frames as necessary without overstraining the capacities of the MIDAS table format.

We decide to sum-up 5 frames in the H band, 2 in $J1$, 4 in $J2$ and 2 in Y. The summation process is done with a standard MIDAS routine, that performs a simple pixelwise summation. Therefore, an accurate measurements of the shifts of the frames has to be done beforehand. To preserve good seeing on our best frames, only images with similar seeings are summed-up. Still, due to uncertainties in the alignment the seeing increases by $\sim 0.1''$. In addition, only

images from the same observation run are summed-up, as that leads to better results in the flux measurement process.

With the number of images in each filter reduced by a factor between 2 and 5, fluxes can be measured on the summed-up images.

3.11 Adding COMBO-17 Data

As the COMBO-17+4 survey consists of not only the four NIR filters, but also out of 17 colors in the optical, it is necessary to merge these two data sets.

The data from the optical part of the survey was already reduced and mostly analyzed by Wolf et al. (2003a, 2003b, 2004, 2005, 2007, 2008). Due to some changes in the naming convention of some basic descriptors since then, the descriptors ccd_para, start and filter have to be updated or rewritten. In addition, the descriptor *epsilist* is not saved by MIDAS when the images are transformed from the MIDAS format *.bdf to the usual *.fits format, so this descriptor has also to be rewritten as well. The transformation between these two formats is necessary as the data reduction started with a Solaris computer and changed later to a Linux computer. Due to this difference in operating systems, the *bdf format is read out differently on the two systems and so the *.fits format has to be used.

Since the zero point in the internal coordinates system is different between the optical and the NIR part of the survey, the descriptor *start* has to be adapted to the start value of the deep *H* band image. Afterwards, the shift between the master catalog from the COMBO-17+4 survey and the optical frames is calculated with only the bright stars within the field used as reference objects. Galaxies and faint stars – especially blue ones – are not able to help us in finding references in both surveys and in a worst case scenario can even lead to wrong shifting parameters.

As with the NIR data, frames for which no objects are found or for which we are not able to calculate a shift, are excluded from the survey. Because of this, a whole run in the R band has to be excluded from the A226 data, as no useful shift can be calculated. After updating the individual frames we do a new photometry on the optical frames, as described in Section 3.12.

3.12 Flux Measurement

After the final correction of the frames for all four filters, we can measure the photometric values of the detected objects, which are saved in the master cat-

alog. To measure the fluxes the routine EVALUATE/IMAGE is used (Roeser and Meisenheimer, 1991). This function analyses all images with a common effective point-spread function (PSF). This is done to avoid spurious colors when images taken under different seeing conditions are combined. Therefore every image is analyzed with a different Gaussian weighted function:

$$\sigma^2_{\text{eff}} = \sigma^2_{\text{seeing}} + \sigma^2_{\text{weight}} = \text{const.} \tag{3.2}$$

Equation 3.2 shows that images with a good seeing are analyzed with a broad weighting function, whereas images with a bad seeing are analyzed with a narrow one. For the COMBO-17+4 data (NIR as well as optical) we choose, in agreement with the work done by Nicol (2009), a common effective PSF of $1.7''$ FWHM. The setup file, which contains all necessary information for the evaluate-procedure, can be found in Appendix A.

After successfully measuring the fluxes on each image in each filter, all the measured fluxes from one filter are combined into a single table. Therefore the routine FLUX/UNITE is used. At the end of this step 21 flux tables (one for each filter) are available.

3.13 Color Indices

We use color indices to check and improve the calibration of our objects in the united flux table using template stars from the catalog by Pickles (1998). The color indices are also needed for the classification of the objects, which will be discussed in Section 4.

A color index itself simply describes the difference of the objects brightness between two chosen filters and is given in magnitudes. As it is difficult to convert color indices into flux values (and vice versa) using the classic Vega magnitude system, Wolf et al. (2001c) introduced a new magnitude system. This system, called *CD magnitudes*, was originally developed for CADIS and gives flux values in units of photons per (m^2 s nm) as it is common in the X-ray astronomy.

$$CD_{\text{mag}} = 20.01\text{mag} - 2.5 \log F_{\text{phot}}. \tag{3.3}$$

F_{phot} is given in $\gamma \text{m}^{-2}\text{s}^{-1}\text{nm}^{-1}$ and objects with $F_{\text{phot}} = \text{const}$ therefore have CD colors equal to zero. The system is designed in a way that the zeropoint is at a wavelength of $\lambda_0 = 548$ nm, which is a common zeropoint in astronomy (e.g. astronomical magnitudes, ABmag by Oke (1964) or STmag by Walsh (1996)). Thus, an object with $V \sim 20.01$ mag has a flux of $1\gamma \text{m}^{-2}\text{s}^{-1}\text{nm}^{-1}$ at λ_0.

Color indices and errors on the basis of CD magnitudes are defined as:

$$m_1 - m_2 = -2.5 \log \frac{F_{\text{phot},1}}{F_{\text{phot},2}}, \tag{3.4}$$

$$\sigma_{m_1 - m_2} = \sqrt{(\sigma F_{\text{phot},1} / F_{\text{phot},1})^2 + (\sigma F_{\text{phot},2} / F_{\text{phot},2})^2}. \tag{3.5}$$

To calculate the color indices it is necessary to obtain the fluxes of the objects in each of the filters (see Equation 3.4). For the COMBO-17 survey the *Asinh* magnitude system was used (Wolf et al., 2001c). This system was developed by Lupton et al. (1999) for the SDSS and creates a modified magnitude system that does not use a logarithmic definition for magnitudes, but instead a hyperbolic sinus function. Due to this change, colors for very faint objects, and even objects with negative fluxes, can be calculated. During the reduction of the Abell 901 field of the COMBO-17+4 survey by Nicol (2009), it was discovered that the *Asinh* magnitude system leads to two significant redshift focuses at $z \sim 1.0$ and $z \sim 1.6$. Meisenheimer (priv. communication) discovered that the reason for this focuses is the use of colors, which are computed out of a mix of broad- and medium-band filters. Since the SDSS is only using medium-band filters, this problem was not discovered beforehand. To remove the redshift focuses Meisenheimer (priv. communication) developed the *upper limit* magnitude system, which is especially useful for objects with low and even negative fluxes:

$$\text{upper limit}_{\text{mag}} = 20\text{mag} - 2.5 \log(F_{\text{phot}} + 2\sigma_{\text{flux}}) + 2\sigma_{\text{mag}}. \tag{3.6}$$

See Nicol (2009) for more information about the advantages of the *upper limit* system compared to the *Asinh* system.

Out of the 21 filters available in the COMBO-17+4 survey, we calculate 21 color indices for Abell 226 and 23 color indices for S11 – not all of which are used for the object classification. In the optical, the same colors as in the COMBO-17 survey are used. For the NIR part of our survey, the colors $I - J1$, $Y - J1$, $J1 - J2$ and $J1 - H$ are used. The colors in the NIR are always the result of the differences between a filter with a shorter and a longer wavelength. All calculated colors, the color correction and the minimum errors are listed in the Table 3.2. For reference the calculated colors by Nicol (2009) for the A901 field are given in Table 3.3.

Table 3.2: Color calibration factors for Abell 226 and S11. The list shows all the color indices used, as well as the zeropoint correction for the corresponding indices. The third column shows the minimum assumed error for each color.

Abell 226

Color Index	Color Correction [CD mag]	Min. Error [CD mag]	Color Index	Color Correction [CD mag]	Min. Error [CD mag]
U-B	0.10	0.10	R-697	-0.09	0.00
B-V	-0.02	0.00	752-I2	0.00	0.00
V-R	-0.07	0.00	816-I2	0.00	0.00
R-I2	-0.02	0.00	I-856	-0.03	0.00
418-B	0.00	0.00	I-915	0.00	0.00
B-464	-0.05	0.00	I2-J_1	0.10	0.07
486-V	-0.03	0.00	I-Y	0.076	0.07
520-V	-0.03	0.00	Y-J_1	0.00	0.00
573-R	-0.03	0.00	J_1-J_2	-0.04	0.00
605-R	0.02	0.00	J_1-H	0.10	0.00
643-R	0.00	0.00			

S11

Color Index	Color Correction [CD mag]	Min. Error [CD mag]	Color Index	Color Correction [CD mag]	Min. Error [CD mag]
U-B	0.20	0.10	R-752	0.00	0.00
B-V	0.00	0.00	R-816	0.00	0.00
V-R	-0.06	0.00	752-I	0.00	0.00
R-I	-0.03	0.00	816-I	0.00	0.00
418-B	0.04	0.00	I-856	0.00	0.00
B-464	-0.03	0.00	I-915	0.00	0.00
486-V	0.00	0.00	I-J_1	0.00	0.07
520-V	-0.03	0.00	I-Y	0.10	0.07
573-R	0.00	0.00	Y-J_1	-0.06	0.00
605-R	-0.02	0.00	J_1-J_2	-0.02	0.00
643-R	0.04	0.00	J_1-H	0.00	0.00
R-697	0.00	0.00			

Table 3.3: Color calibration factors for Abell 901 as used by Nicol (2009). The list shows all the color indices used, as well as the zeropoint correction for the corresponding indices. The third column shows the minimum assumed error for each color.

Abell 901					
Color Index	Color Correction [CD mag]	Threshold [CD mag]	Color Index	Color Correction [CD mag]	Min. Error [CD mag]
U-B	-0.02	0.10	643-R	0.03	0.00
B-V	0.02	0.00	R-697	0.00	0.00
V-R	-0.06	0.00	752-I	-0.01	0.00
R-I	-0.03	0.00	816-I	0.03	0.00
418-B	0.00	0.00	I-856	0.00	0.00
B-464	-0.05	0.00	I-915	-0.03	0.00
486-V	-0.02	0.00	I-J_1	0.03	0.07
520-V	-0.05	0.00	Y-J_1	-0.046	0.00
573-R	-0.05	0.00	J_1-J_2	0.05	0.00
605-R	0.01	0.00	J_1-H	0.05	0.00

3.14 Flux and Color Calibration

To calibrate the fluxes of all 21 filters we use standard stars. These are selected from the *R* band catalog from the COMBO-17 survey. All stars have to have well fitted templates from the Pickles (1998) catalog (see Section 4.1.1 for more details). As no observed data exists in the Pickles template catalog in the wavelength range between $\approx 1050 - 1450$ nm, the data has to be interpolated in this region. For the selection of standard stars, it is important to check the quality of the interpolation of the templates used.

Individual standard stars are required for each subfield of the COMBO-17+4 survey as the measured fluxes for each pointing and each frame are only relative fluxes. For the optical data of the COMBO-17 survey several secondary standard stars were spectroscopically observed. For the COMBO-17+4 survey we use main sequence stars with a good fitting template from the Pickles (1998) library. For these tertiary standard stars a good interpolation of the templates at the wavelengths ≈1050-1450 nm is necessary (see Section 4.1.1 for more details). With the help of the standard stars, these relative fluxes can be translated into physically meaningful measurements.

Severals standard stars are used to calibrate the fluxes in the different filters and subfields. For Abell 226 we use four standard stars in the subfields A, B and D, whereas we only have three in the subfield C. For the optical data of Abell 226 we only have one standard star, which is identical with a standard star in the B subfield of the NIR part of the COMBO-17+4 survey. For S11 we use only five standard stars for the three subfields: One star for each subfield

C and D and three stars for subfield B. Due to calibration problems we do not use the two original optical standard stars from the COMBO-17 survey, but the star which is also used to calibrate subfield D. The list of standard stars used for the NIR data of the survey can be seen in Table 3.4.

After the flux calibration with the standard stars the 21 flux tables are combined in one flux table. This table now contains all necessary information from every detected object for further investigation of the observed field, including world coordinates, right ascension, declination, fluxes for all filters and the respective errors. All final flux tables from the three observed fields have the same structure, which will make it easier to combine the data in the end. The structure of the COMBO-17+4 flux tables, again, is based on the COMBO-17 format.

After the calibration of the fluxes and their combination, it is also necessary to adjust the objects' colors, as wrong colors will lead to a misclassification of the object. This color correction is performed with the star templates from the Pickles (1998) library. The colors of the stars in the library are compared with the colors of the stars from the COMBO-17+4 survey. The Pickles catalog will also be used later in the classification process.

Since stars can be found in the main sequence of the color-color plot, we use a visual inspection to compare their colors with the colors from our bright point sources in the plots. As a result, we select only round objects which have a magnitude of $13 < H < 19$ from our catalog. In contrast to the Abell 901 reduction by Nicol (2009), we do not use the preclassification by SExtractor, as this classification seems to be inaccurate at the faint end, where stars and elliptical galaxies are mixed up. Within the Abell 226 field, we use 556 stars for calibration. In the S11 field we use 740 stars. A subset of color-color plots for both fields can be seen in the Figures 3.9 and 3.10.

Only some minor corrections have to be made for the optical data, as the color correction factors are already well known from the COMBO-17 survey. For the NIR data, we start with the factors from the Abell 901, field which then are adjusted in several iterations. The final color calibration factors for both fields are listed in Table 3.2. For comparison, the calibration factors for the Abell 901 field are listed in Table 3.3.

Missing data in the standard stars' spectral templates lead to some problems in this process. Specifically, as incorrect normalization of our fluxes in some of the subfields of A226 occurred. The reason therefore is the incorrect interpolation between the optical spectra and the spectra in the H band. Because of that, we have to adjust the fluxes in the subfields by multiplying them with the missing factor to get a correct photometry: In subfield A we have to adjust $J1$ by 1.12, $J2$ by 1.12 and Y by 1.36. In subfield B we adjust $J1$ by 1.15, $J2$ by 1.15 and Y by 1.09. After multiplying the fluxes with these numbers

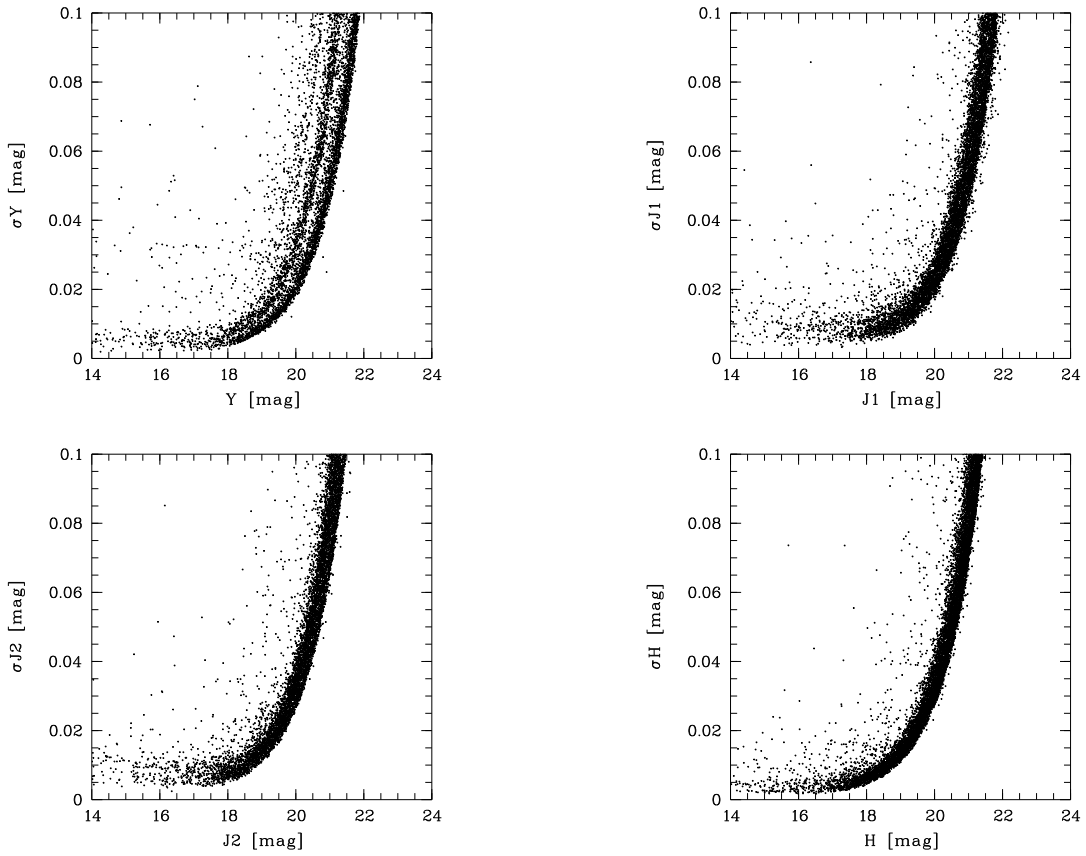

Figure 3.7: The magnitudes of all objects with a maximum error of 0.1 mag in the Abell 226 field versus their errors. The four NIR filters are shown separately. The figures include objects from all four subfields.

the identified main-sequence stars from the Abell 226 field are shifted into the main-sequence given by the stars from the Pickles (1998) library.

A second problem is identified in the color calibration process of subfield A in the *J*2 band of the Abell 226 field, where half of our calibration stars have a lower flux than the rest. A closer analysis of this data shows that this problem results from several individual images in only one run. The flux difference correlates well to the slope of the flatfield used for these images. However, we do not find a reason why the flatfield is not usable for these specific images. Repetition of the full data reduction chain was performed, but since this does not remove this erroneous slope, we exclude these images from further analysis.

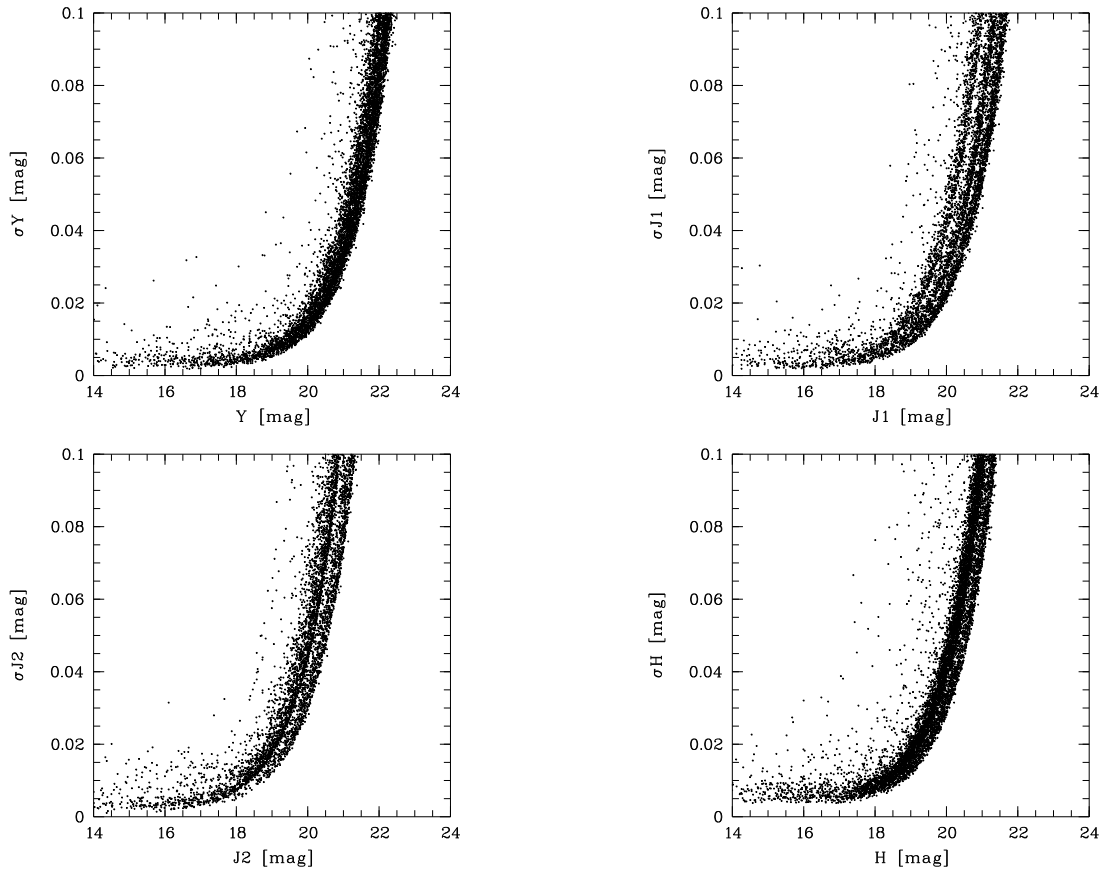

Figure 3.8: The magnitudes of all objects with a maximum error of 0.1 mag in the S11 field versus their errors. The four NIR filters are shown separately. The figures include objects from all three subfields.

3.15 Variability Correction

After the color calibration, we also correct objects that show variability in the different runs. This correction is necessary for all observed filters, as otherwise the SED based classification will lead to wrong results. The most numerous variable objects that have to be corrected are quasars and Seyfert galaxies. In addition to these two types of objects we also have to correct some variable stars. According to Wolf et al. (2004) it is also possible to correct for supernovae but no such object is detected in the survey. Wolf et al. (2004) mentioned that ignoring the variability of these objects will not only lead to a possible missclassification, but will also lead to a dramatic increase in their redshift errors.

Objects are identified as variable based on their flux in each R band observation run. Therefore no short time flux changes, which are in the time scale of one observation run, can be corrected. In agreement with Wolf et al. (2004),

we only correct objects which meet the following criteria:

- the flux of at least one of the R band measurements is determined to better than 10 σ;
- the difference in flux between two runs have to be at least 0.15 mag;
- and the difference have to have a significance of at least 6 σ.

For correction of the variable objects we use the flux difference in R between two different observation runs, because the R band was the only filter which was observed in almost every observation run:

$$(m_{\text{filter 1}} - m_{\text{filter 2}})_{\text{corr}} = -2.5 \log \frac{F_{\text{filter 1, run i}}}{F_{\text{filter 2, run j}}} + (R_{\text{run j}} - R_{\text{run i}}) \tag{3.7}$$

In observation runs without any R band data available the correction factor is calculated using the flux difference of other bands, which are observed during more than one observation run. However, some objects show a variability which is different over several wavelengths. Because we are only using the R band as a reference filter, we cannot correct the variability for these objects. In addition we do not correct for variability in the NIR filters, as these observations are made years later and we do not have a common reference filter. To reduce the effect of variability we therefore assume a minimum error of 0.07 mag for colors which use an optical and a NIR filter.

3.16 Magnitude Limit and Completeness

The magnitude limit depends on the absolute exposure time of the combined images. Therefore, we have a different magnitude limit not only in different filters, but also in different subfields. The depth reached in each filter can be seen in the Figures 3.7 and 3.8. The figures show the magnitude of all objects in the corresponding fields versus their magnitude errors up to an error of 0.1 mag in the four NIR filters.

Since we are interested in the statistical distribution of galaxies in different redshift ranges, we also need the completeness limit for each field. As the exposure times for the different subfields can vary, the completeness limit for one entire field is determined by the shortest total exposure time in one subfield. Nicol (2009) determined a completeness limit of $H = 21.7$ mag for the Abell 901 field, whereas we found a limit of $H = 22.0$ mag for the Abell 226 field and

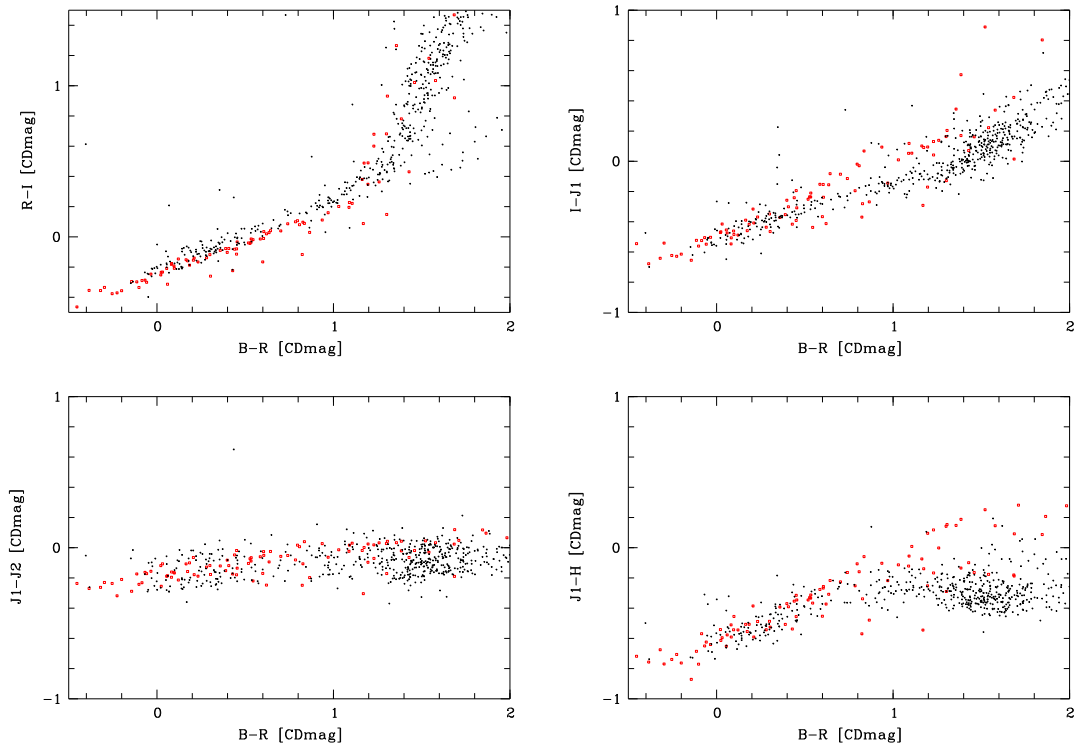

Figure 3.9: Some color-color diagrams from the Abell 226 field. Red dots indicate the templates from the Pickles (1998) catalog. Black dots show bright stars in the A226 field of the COMBO-17+4 catalog. These diagrams are used to measure the color correction factor for each filter. Colors are given in CD magnitudes.

$H = 21.7$ mag for the S11 field (see also Figure 3.11). For all further statistical analyses only galaxies brighter than these limits are taken into account. For analyzing the results of all three fields together we use the lower completeness limit from the Abell 901 and S11 fields, with $H = 21.7$ mag.

Table 3.4: Standard stars in A226 and S11 field. The first column shows the number of the star in the corresponding COMBO-17+4 catalog. The second column gives the name of the standard stars. The names give information about the field and the subfield, where they can be found. α and δ gives the coordinates of the stars on the sky. The columns m_H and m_R give the measured apparent magnitudes in H and R respectively.

Catalog Number	Name	α	δ	m_H [mag]	m_R [mag]	Subfield
01950	$A226\_c1$	$01^h39^m20.12^s$	$-10°24'09.54''$	13.72	14.80	C
02981	$A226\_b1$	$01^h39^m42.28^s$	$-10°22'41.86''$	14.98	15.86	B
03952	$A226\_b2$	$01^h40^m16.74^s$	$-10°21'20.43''$	13.74	15.94	B
04233	$A226\_c2$	$01^h39^m06.94^s$	$-10°20'58.92''$	14.26	15.46	C
07206	$A226\_b3$	$01^h39^m43.26^s$	$-10°17'19.72''$	13.65	14.85	B
13137	$A226\_a1$	$01^h40^m06.87^s$	$-10°10'08.65''$	13.79	15.23	A
13147	$A226\_d1$	$01^h38^m49.59^s$	$-10°10'08.06''$	14.02	15.36	D
17965	$A226\_a2$	$01^h39^m46.95^s$	$-10°04'39.34''$	15.00	15.82	A
20134	$A226\_d2$	$01^h39^m16.79^s$	$-10°02'07.86''$	13.77	14.82	D
23408	$A226\_d3$	$01^h38^m39.84^s$	$-09°58'27.15''$	14.54	15.58	D
24718	$A226\_a3$	$01^h39^m46.09^s$	$-09°57'09.26''$	14.19	15.13	A
08365	$S11\_\_c2$	$11^h43^m03.14^s$	$-01°47'39.24''$	18.24	19.24	C
08830	$S11\_\_d3$	$11^h42^m33.68^s$	$-01°47'06.38''$	16.72	18.09	D
13833	$S11\_\_b4$	$11^h42^m55.74^s$	$-01°41'36.24''$	17.78	19.25	B
15223	$S11\_\_b2$	$11^h42^m45.95^s$	$-01°38'45.41''$	17.53	18.51	B
15481	$S11\_\_b3$	$11^h42^m50.79^s$	$-01°38'10.10''$	17.37	18.35	B

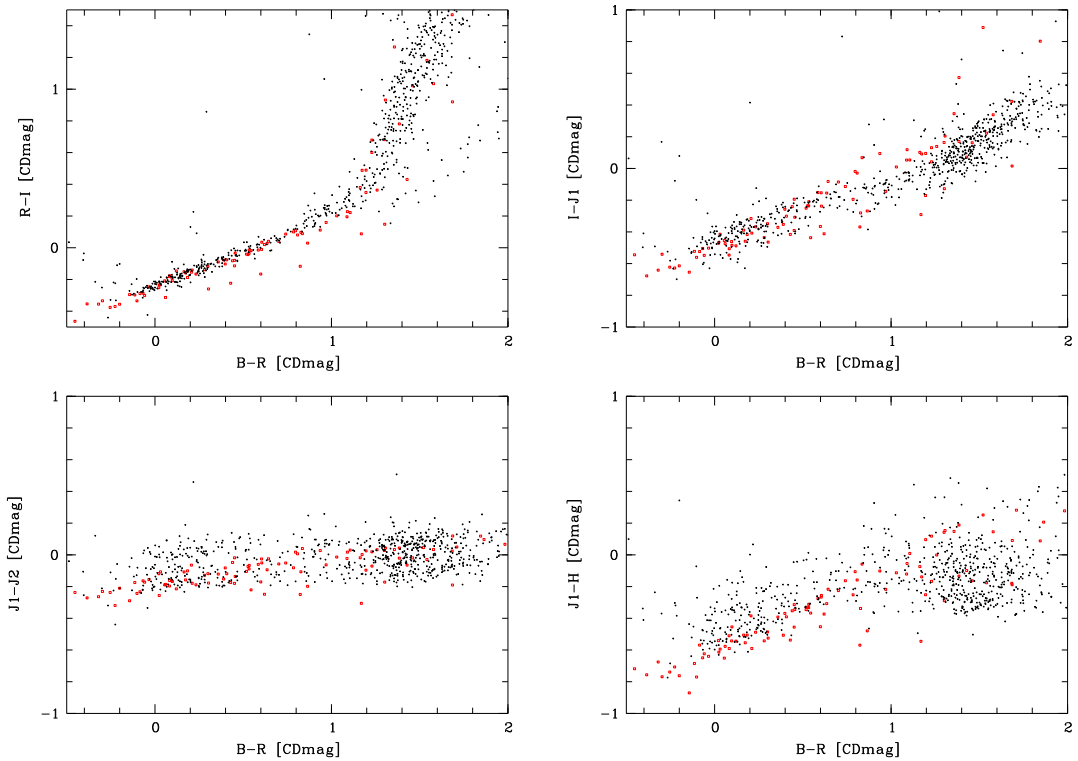

Figure 3.10: Some color-color diagrams from the S11 field. Red dots indicate the templates from the Pickles (1998) catalog. Black dots show bright stars in the S11 field of the COMBO-17+4 catalog. These diagrams are used to measure the color correction factor for each filter. Colors are given in CD magnitudes.

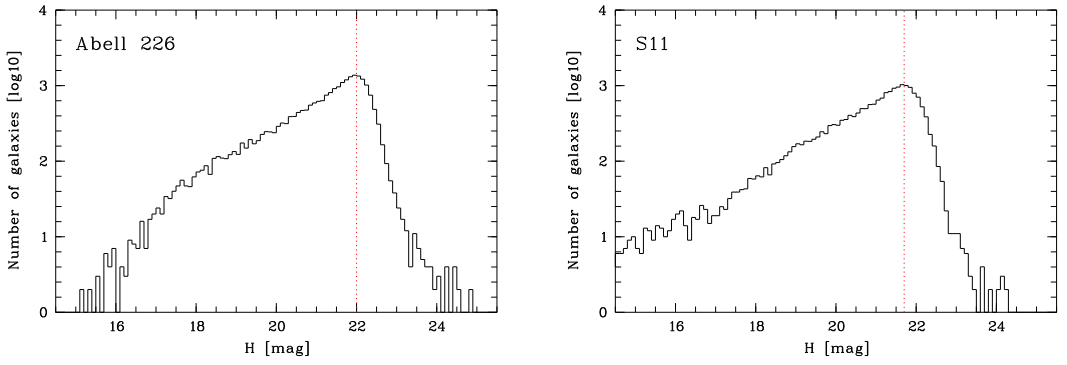

Figure 3.11: Completeness limits of A226 and S11 in the H band. For a further analysis, only galaxies brighter than the completeness limits of the corresponding fields are taken into account.

Chapter 4

Object Classification and Scientific Analysis

This chapter explains how the calculated rest-frame colors are interpreted so that a classification of the detected objects is possible. In addition the first results are presented. They contain the distribution of galaxies in the redshift range $0 < z < 2$ (shown for the fields Abell 226 and S11 as well as for all galaxies in the COMBO-17+4 survey) and the evolution of SEDs. We also present a direct comparison between the COMBO-17 and the COMBO-17+4 survey of measured redshifts of objects common in both catalogs.

4.1 Object Classification

The object classification is based on a comparison of the color indices of the COMBO-17+4 survey and the colors of known objects from object libraries. This method was developed by Wolf (1998) for CADIS and is also suitable for COMBO-17+4, only with different colors. Using color indices instead of fluxes has the advantage of avoiding absolute calibration for each wavelength used. This works only if the fluxes are calibrated well with each other which is achieved with the help of spectroscopical measured standard stars. How this calibration is done is explained in Section 3.13. Further details on the classification process can be found in the MPIAPHOT manual, Wolf et al. (2001b) and Wolf et al. (2001c).

4.1.1 Libraries

The objects are classified using SEDs from several different libraries, which contain observed and synthetic spectra. Together with the color information

from the COMBO-17+4 survey we can then use these libraries to calculate probabilities for the class of each object. We distinguish between stars, white dwarfs, galaxies or QSOs. In total we use four libraries (2 for stars, 1 for galaxies and 1 for QSOs), each library contains the color indices of our survey. Combining these results with the potential variability and the morphology we do the final classification.

The star libraries and the QSO library were already used for the COMBO-17 survey whereas for galaxies we are using a new, more accurate library. Information on the libraries are gathered from the corresponding papers and mainly from the MPIAPHOT user manual. Therefore, further detail on the libraries can be found in the cited papers and the user manual.

Star Libraries

We are using two different libraries for the classification of stars. The library by Pickles (1998) contains 96 star-templates of the spectral types F, G, K and M and covers the luminosity classes I to V. However, the library has two weaknesses. The first is the incompleteness of data in the NIR. The library was constructed using spectra from several resources covering the wavelengths from the UV to the IR, but as for the NIR only a few and poorly calibrated fluxes were available, most of the templates do not cover this wavelength area. Therefore, the data for wavelengths in the range of $\approx$1050-1450 nm had to be interpolated. As the calibration with the used standard stars for the COMBO-17+4 survey shows, these interpolations are not always accurate, but the Pickles library is still better than comparable older catalogs.

The second weakness of the Pickles library is the lack of L-stars and white dwarfs. Therefore we use a second star library by Detlev Koester which is using theoretical spectra and contains white dwarfs (WD), blue horizontal branch (BHB) stars and sub-dwarfs. This way the lack of these types of stars in the Pickles library can be compensated.

QSO Library

To identify QSOs in our catalog we use a library which is derived from the SDSS template spectrum (Vanden Berk et al., 2001), using 2200 QSO spectra. The color library covers the redshift range from $0.504 < z < 5.96$. At a redshift of $z < 0.5$ the available templates do not cover the complete filter set of the COMBO-17 nor the COMBO-17+4 survey (Wolf et al., 2004). Wolf et al. (2004) state that not many QSOs are expected at low redshift so that this problem is acceptable. The library uses a three dimensional grid to identify QSOs: the spectral slope axis (with 20 steps), the emission line strength (with 9 steps)

and the redshift (with 155 steps). The redshift gird has a resolution of 0.01 in $\log(1+z)$.

Galaxy Library

As already mentioned above, we are using a different galaxy library than the one used for the COMBO-17 survey. The old library by Kinney et al. (1996) used 10 template UV-optical data of starburst and quiescent galaxies, based on observational data. They extended these ten templates by interpolation up to 100 spectral types.

The new library by Meisenheimer (priv. communication) uses an improved version of the library by Borch et al. (2006) which contains templates on the basis of a two starburst formation model. This improved two-burst model allows to reproduce a wide range of galaxy types (from starburst to quiescent) and it allows a mixture of a young and old star population in the galaxies.

The new library is calculated using the PEGASE[1]-code (Fioc and Rocca-Volmerange, 1997) and contains galaxy templates in 60 different ages. Each of these templates is available with 6 different extinction levels, which results in 360 different galaxy templates. The age of the galaxies cover a range from 50 Myr to 15 Gyr and the extinction level from 0 to 0.5; the redshift covers the range of $0 < z < 2.3$ and has a resolution in z of 0.005 in $\log(1+z)$.

For the classification the available 60 different SED types are fitted to the galaxies identified in the deep *H* band images, whereas SED template with # 1 indicates a blue, young starburst galaxy and # 60 red and old galaxies. Galaxies with SED numbers of 1-25 are therefore starburst galaxies, number 26-42 are typical disk galaxies and numbers above 42 are bulge dominated galaxies.

4.2 Update of the Classification Procedure

Compared to the classification process done by Nicol (2009) we update the photometric redshift estimation in excluding a simple sub procedure in the classification program.

During the classification process it can happen that two possible redshift solutions for one object exist. Normally the solution with the higher probability is taken (this can either be the higher or the lower photometric redshift). However, for the COMBO-17 survey an extra condition was added to the program: If two redshifts are possible for a galaxy and if the higher redshift is $z > 1$,

[1]Project d'Étude des GAlaxies par Synthèse Évolutive

Table 4.1: Detected objects in the three different fields from the COMBO-17+4 survey. Numbers for the Abell 901 are taken from Nicol (2009). The columns objects, stars and QSOs show all detected objects in the corresponding field, whereas the column galaxies only gives the number of these galaxies, which are finally used for the further investigation.

Field Name	Objects	Galaxies	Stars	QSOs	Subfields
Abell 901	32,340	12,023	1,871	169	3
Abell 226	25,431	16,984	1,220	199	4
S11	20,358	13,127	1,221	84	3
Total	88,129	42,134	4,321	452	

the two redshifts are checked again. The larger the difference between the redshifts is, the more likely the lower redshift value is taken. This procedure was useful for the COMBO-17 survey as it was unlikely that many galaxies were detected at $z > 1$, using optical filters only, but it contradicts the idea of the COMBO-17+4 survey where we want to identify as many high redshift galaxies as possible. The exclusion of this subprogram leads to a significant change in the redshift distribution of the classified galaxies, especially at $z > 1$. We therefore have to assume that between 5 to 10% of the galaxies in the A901 field have a wrong calculated (too low) photometric redshift. An analysis in the exact amount of galaxies in the A901 field with wrong redshifts still has to be done.

A second change with respect to the Abell 901 field, analyzed by Nicol (2009), is the use of an additional medium-band filter in the Abell 226 field. Additionally to the normal broad band I filter observations with the $I2$ filter were made. The filter has a central wavelength of $\lambda_c = 827$ nm and a FWHM of $\lambda_{\mathrm{FWHM}} = 203$ nm. This filter allows a better redshift estimation for objects at $z > 1$ because it has a smaller FWHM than the standard I filter. For the Abell 226 field almost all classification criteria which normally use the I filter are replaced with the $I2$ filter. Still, in the S11 field only the standard I filter is available.

4.3 First Results

The object classes in the master catalog are determined using the maximum-likelihood and minimum error variance method. The classification distinguishes between the following types: *star* (if the object has stellar colors or if it has a round shape and a redshift of $z < 0.2$), *WDwarf* (if object has the colors of a WD, BHB star or subdwarf or if it has a round shape and a redshift of $z < 0.2$), *galaxy* (if the object has the colors of a galaxy whereas the shape is irrelevant), *galaxy (star?)* (if the objects has the colors of a star, but an extended

shape and a redshift of $z < 0.2$), *galaxy (uncl!)* (if the color is unclear; statistics showed that it is almost always a galaxy), *QSO* (if the colors fit to a QSO and the object shows a stellar shape) and *QSO (gal?)* (if the color fits a QSO, but the shape is extended). The remaining objects are summed-up in *strange objects* and contain photometric artifacts, objects with strong uncorrected variability or objects with an unusual spectrum. The objects labels are chosen based on the calculated probability for each object. A list which contains the numbers of different object classes found in the three different fields is given in Table 4.1. The table shows that roughly 4,000 galaxies per observed subfield are used for further analysis.

After the classification we have redshifts, redshift errors, and SED type – for objects classified as galaxies – available. All of these results are made on the basis of a minimum error variance method and on the basis of a maximum likelihood of the nearest object in the four libraries.

Later we will discuss the distribution of galaxies in the redshift space and the evolution of different SEDs up to redshift $z = 2$ for both analyzed fields. For the discussion we only use galaxies in the completeness limit in the H band of the corresponding field. In addition to the cut in the H band we add two additional cuts: These cuts are introduced because across the observed redshift range the R and Y band (which have different completeness limits than the H band) are mapped onto the rest-frame V band, which later will be necessary to study the evolution of the red sequence.

At redshift $z < 0.43$ the observed R band is redder than the 4000 Å and roughly coincident with the rest-frame V band and so we require the galaxies in this redshift regime to have $R < 24.5$ mag. This is a magnitude deeper than the completeness limit of the COMBO-17 survey. However, as already mentioned by Nicol et al. (2011), the additional NIR data lead to a completeness at fainter magnitudes. At $0.43 < z < 1.4$ the Y band is redder than the 4000 Å break and therefore we exclude objects in this redshift range fainter than $Y < 22.8$ mag.

4.3.1 Abell 226 Field

Within the Abell 226 field we find 25,431 objects in the H band deep catalog. 18,841 of these objects are brighter than $H < 22$, which is the completeness limit of this field. The classification of the objects shows that 17,390 galaxies are within the limiting magnitude range. Within the limiting magnitude we are able to identify 1,220 stars and 199 QSOs. After making additional cuts in the R and Y band (as explained above) 16,984 galaxies remain in the A226 field.

The distribution of all galaxies and of the galaxies within our limiting mag-

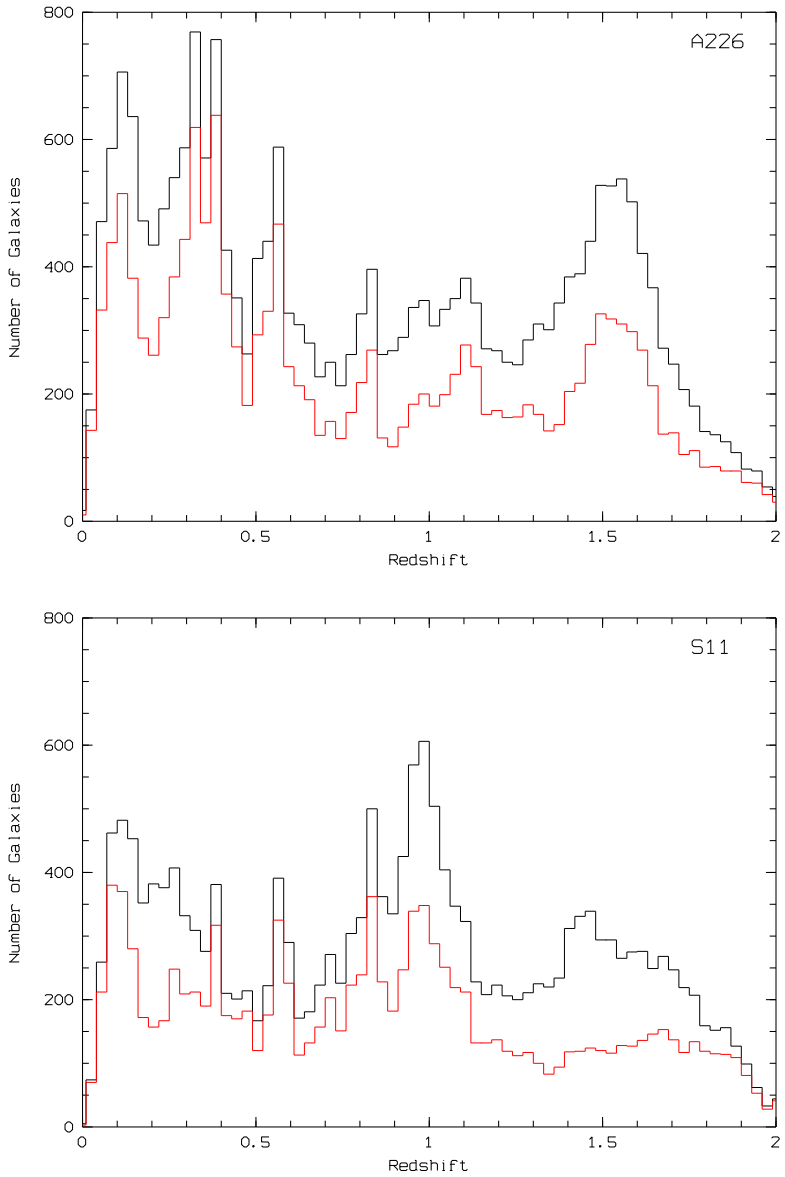

Figure 4.1: Redshift distribution of the galaxies found with the COMBO-17+4 survey in the Abell 226 and the S11 field. The black line contains all galaxies, whereas the red line only contains galaxies in the completeness limit of $H < 22.0$ for the A226 field, respectively $H < 21.7$ for the S11 field. In addition only galaxies with magnitudes of $R < 24.5$ at $z < 0.43$ and $Y < 22.8$ at $0.43 < z < 1.4$ were used.

nitudes can be seen in Figure 4.1. We examine redshift ranges with a higher number of galaxies. Contour plots of these redshift ranges are shown in Figure 4.2. The first peak in the distribution of Figure 4.1 at $z \sim 0.1$ indicates, among others, the clusters of Abell 226 and Abell 228. Abell 226 is visible as an overdensity in the middle of the top left panel in Figure 4.2. The second overdensity visible in Figure 4.1 with two sharp peaks at $0.23 < z < 0.44$ can

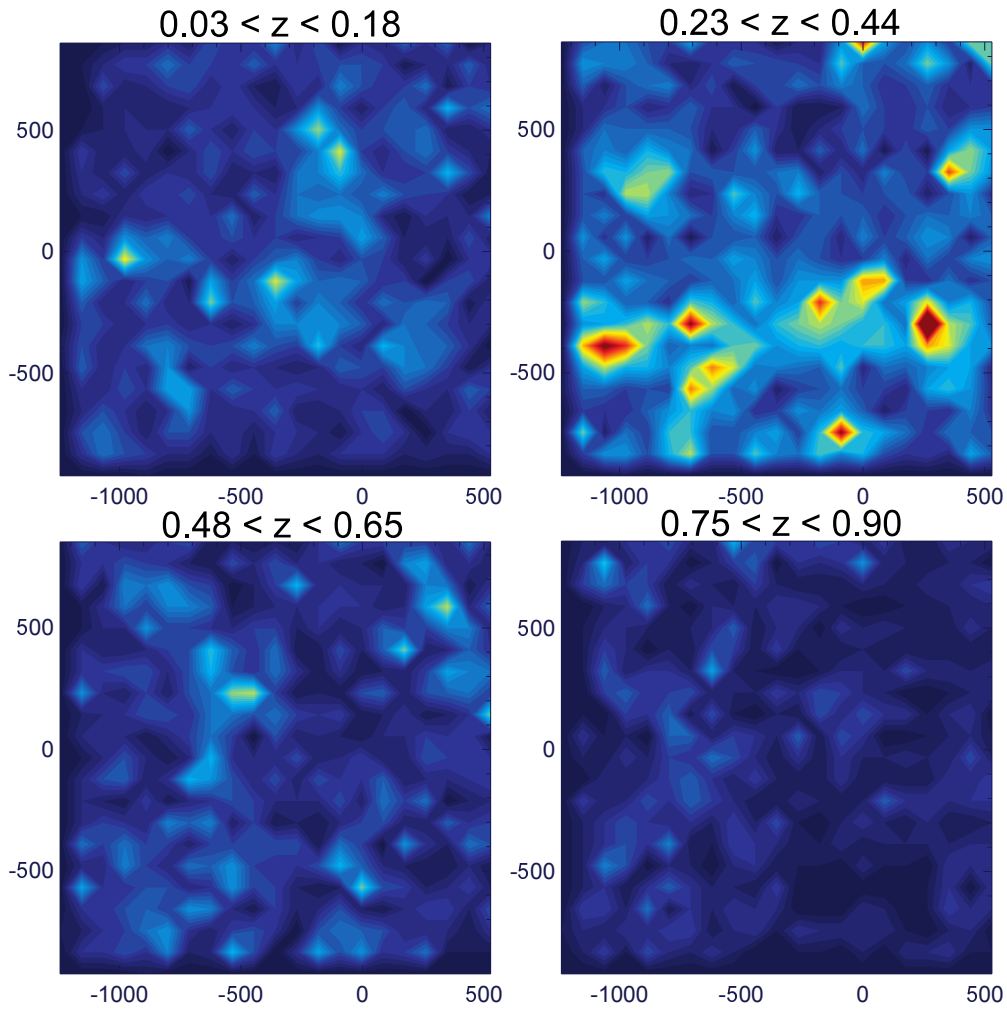

Figure 4.2: Position of overdensities in the A226 field. Yellow and red areas indicate a high density of galaxies, whereas blue and black ares indicate low densities. The panel on the top left shows galaxies at $0.03 < z < 0.18$ and the overdensity caused by the Abell 226 cluster (visible in the center of the figure). The panel on the top right shows the positions of overdensities at $0.23 < z < 0.44$, which have been identified as galaxy clusters by the NED. The lower left panel shows galaxies at $0.48 < z < 0.65$; one overdensity is visible near the center of the figure. The lower right panel shows galaxies at $0.75 < z < 0.90$; no overdensities are visible.

also be seen in the COMBO-17 survey. It originates from eight known clusters in this redshift range. The existence of the clusters has been verified with the NED[2] and they are also visible as overdensities in the top right panel of Figure 4.2. There is also one overdensity visible in this figure at $x \sim -900$ and $y \sim -400$ which is not listed in the NED and most likely an unknown galaxy cluster. The sharp peak at $z \sim 0.55$ in the redshift distribution can also be explained as an overdensity, as one is visible in the lower left contour plot near

[2]NASA/IPAC Extragalactic Database

the center of the image. The fourth broad peak in the range of $0.75 < z < 0.90$ is also visible in the COMBO-17 survey but no information on galaxy clusters in this redshift range can be found in the NED. However, no overdensities are visible in the contour plot (bottom right). The significant increase of detected objects at $z > 1.3$ in general as well as of galaxies which are used for a further analysis is not completely understood.

The other information we have so far is the SED type for each galaxy which is defined in the classification process. The distribution of the different SED types in redshift – which can be seen in Figure 4.3 (top panel) – therefore gives us a first hint on the evolution of galaxies in time. The figure shows the build up of evolved galaxies (SED types > 50) since $z = 2$. The lack of galaxies with SED types > 40 at $z > 1.6$ is remarkable, especially since the evolution of the red sequence at lower redshifts seems to be linear. This lack of high redshift galaxies with SED > 40 seems to be a feature of the Abell 226 field as it was not observed in the Abell 901 field by Nicol (2009). The increasing lack of very blue galaxies with SED numbers < 20 at $z > 1.0$ can easily be explained by the use of an H band selected catalog, which is biased towards redder galaxies. Another interesting feature are the large number of starburst galaxies which can be seen in several narrow redshift bins at $z < 0.9$. Such large number of extreme starburst galaxies are not expected and we can be sure that these objects are misclassified.

4.3.2 S11 Field

In the S11 field we find 20,358 objects in the H band master catalog. As already mentioned the completeness limit for the S11 field is reached at $H = 21.7$ mag. Within this limiting magnitude range we are able to identify 13,333 galaxies, as well as 1,238 stars and 77 quasars. To exclude further objects without reasonable measured fluxes in other filters besides the H band we introduce the same additional limits in the R band ($R < 24.5$ mag at $z < 0.43$) and the Y band ($Y < 22.8$ mag at $0.43 < z < 1.4$). Adding these additional restriction to the objects in the S11 field, 13,127 analyzable galaxies remain in the catalog.

The distribution of all detected galaxies as well as the distribution of the galaxies which remain in the catalog after our restricting magnitude limits are shown in Figure 4.1 (lower panel). As in the A226 field we examine redshift areas with large numbers of galaxies to see if they are the results of local overdensities or of redshift focusing. Because no observations were done with the $I2$ filter to minimize the redshift focusing at $z \sim 0.85$, we expect to find hints of this focusing in the redshift distribution of the galaxies. Contour plots of the redshift areas of interest are shown in Figure 4.5. The first peak at $z \sim 0.5$ contains several galaxy clusters, among others Abell 1364. The second sharp peak at $z = 0.38$ does not show an overdensity in the corresponding contour plot

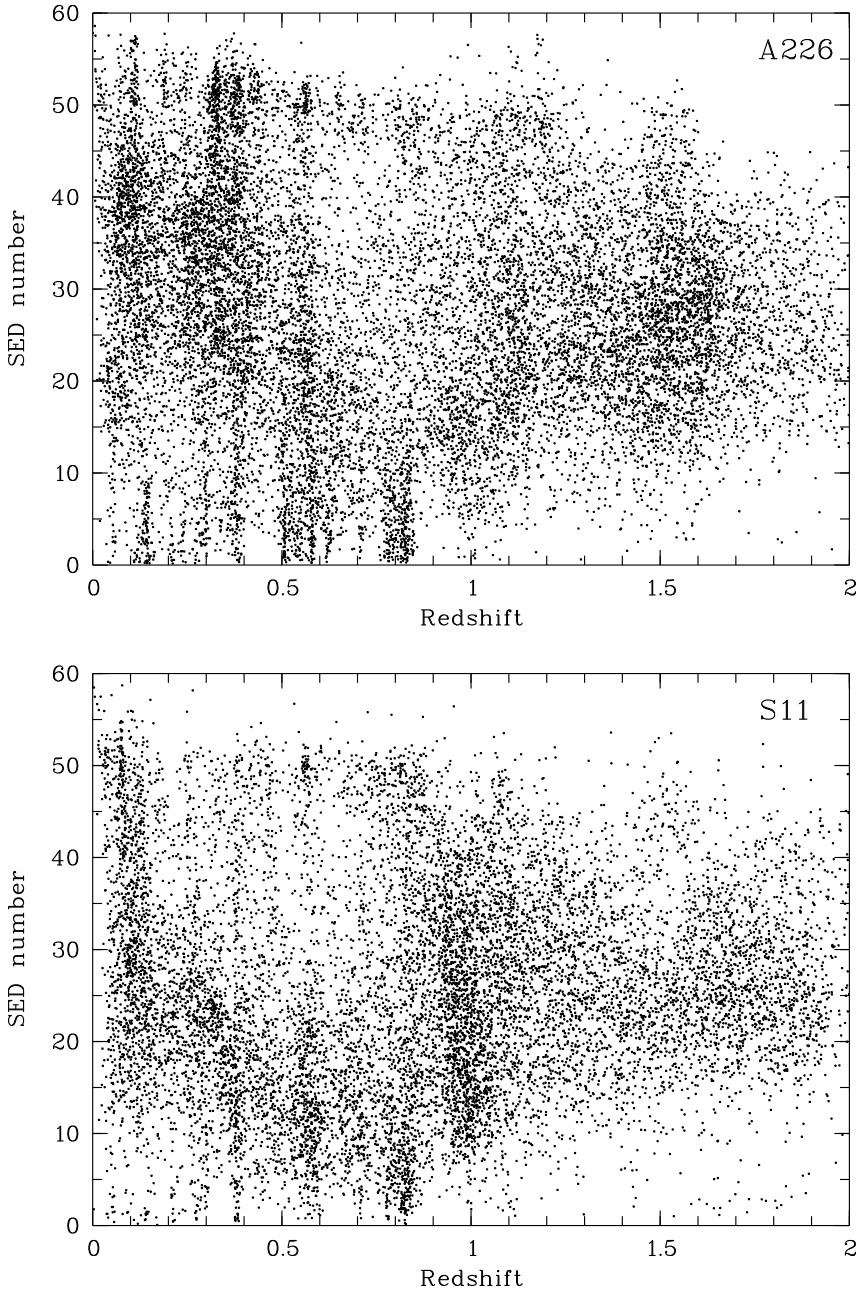

Figure 4.3: Distribution of different SED types in the redshift range of $0 < z < 2$ for galaxies within the completeness limit ($H < 22.0$ for A226 and $H < 21.7$ for S11) and with cuts of $R < 24.5$ at $z < 0.43$ and of $Y < 22.8$ at $0.43 < z < 1.40$. SED templates range from young, blue, starburst galaxies (number 1) to evolved red galaxies (number 60).

and is therefore most likely the effect of redshift focusing. Another sharp peak at $z = 0.55$, which cannot be explained by known clusters, is indeed visible as an overdensity in subfield B. However, in the contour plot we also see a large

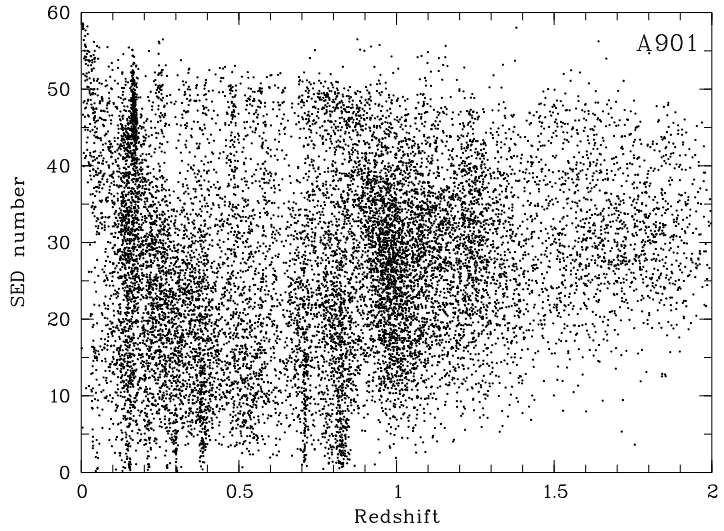

Figure 4.4: Distribution of different SED types in the A901 field, based on the data by Nicol (2009). An overall limiting magnitude of $H < 21.7$ and cuts of $R < 24.5$ at $z < 0.43$ and of $Y < 22.8$ at $0.43 < z < 1.40$ are set.

number of randomly distributed galaxies which leads to the conclusion that also redshift focusing plays a prominent role in the build up of this peak. The fourth peak in the galaxy distribution at $z = 0.83$ is also the effect of redshift focusing plus a possible (yet unknown) cluster. The peak is the result of redshift focusing because of the not used $I2$ filter. The broad peak in the galaxy distribution at $z \sim 1.0$ is most likely the combined result of a redshift focusing and background noise which is included into our list of objects.

Comparing the distribution of galaxies in the A226 and the S11 field we find a feature which is not visible in the A901 field. In both fields of S11 and A226 a significant rise in the number of galaxies at $z > 1.4$ is visible. However, most of the galaxies within these peaks do not fulfill our selection criteria. Many of the excluded objects are indeed only the results of background noise.

If we look at the distribution of galaxies in redshift as a function of their SED type (see Figure 4.3, bottom panel) we see a similar distribution as in the A226 field. However, we do not see a lack of red galaxies (SED > 50) at $z > 1.6$ like in the A226 field, but a linear evolution to less red galaxies at higher redshift. Comparing the results derived from the A226 field and the S11 field shows once more the importance of different field of views for cosmological surveys. Like in the A226 field we can also see a large population of starburst galaxies at $z < 0.9$, which is also visible in Figure 4.4, showing the A901 field (Nicol, 2009). As the distribution of these starburst galaxies in redshift is almost identical in all three fields, we assume a redshift focusing caused by our set of used optical filters.

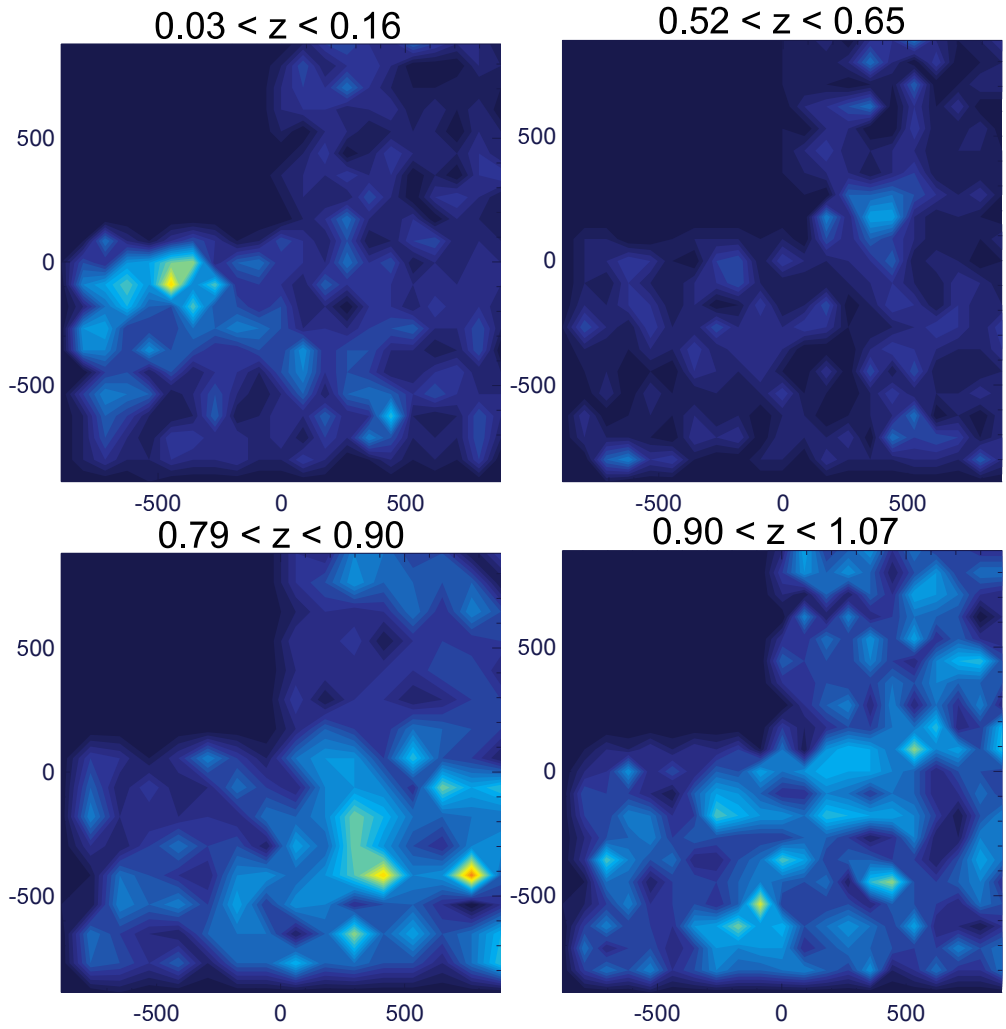

Figure 4.5: Position of overdensities in the S11 field. Yellow and red areas indicate a high density of galaxies, whereas blue and black ares indicate low densities. The panel on the top left shows the positions of overdensities at $0.03 < z < 0.16$, which have been identified as several clusters by the NED. The panel on the top right ($0.52 < z < 0.65$) shows no overdensities. The bottom left panel ($0.79 < z < 0.90$) shows some unknown overdensities but also a large number of uniformly distributed objects. The bottom right frame ($0.90 < z < 1.07$) shows a general high level of galaxies, which is the effect of redshift focusing.

4.3.3 COMBO-17+4 in total

After finishing the classification for the A226 and the S11 field we combine these two fields with the catalog created by Nicol (2009) for the A901 field to get a distribution of all galaxies in the COMBO-17+4 survey in redshift. As only A226 reaches a depth of $H = 22.0$ mag and the other two fields $H = 21.7$ mag, we only use galaxies brighter than $H = 21.7$ mag for the complete catalog. In addition we add the already explained cuts in the R band ($R < 24.5$

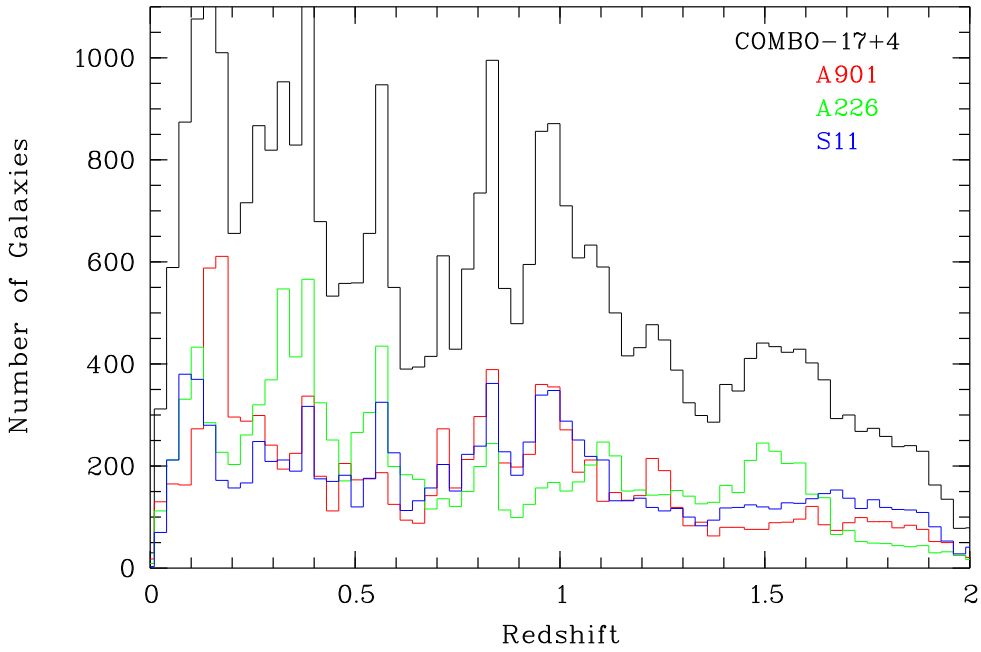

Figure 4.6: Redshift distribution of the galaxies found in the three fields of the COMBO-17+4 survey. The black line contains selected galaxies from all three fields, whereas the colored lines only contains galaxies from the corresponding fields. We only use galaxies with the following selection criteria: $H < 21.7$, $R < 24.5$ at $z < 0.43$ and $Y < 22.8$ at $0.43 < z < 1.4$.

at $z < 0.43$) and the Y band ($Y < 22.8$ at $0.43 < z < 1.4$). In total the combined COMBO-17+4 catalog contains 42,134 galaxies.

Figure 4.6 shows the distribution of the selected galaxies in the COMBO-17+4 survey as well as in the three different fields. In this figure we detect hints for three redshift focuses. The focuses are identified as sharp peaks in the galaxy distribution which show up in all three fields at $z \sim 0.38$, $z \sim 0.56$ and $z \sim 0.85$. At these redshifts the 4000 Å break can be found at 592 nm, 620 nm and 740 nm respectively. The redshifts of the focuses agree very well with the redshifts of our large number of starburst galaxies, which we identified in Figure 4.3. A detailed analysis of these redshift focuses is beyond the scope of this thesis. However, we know that the focusing at $z \sim 0.85$ is caused by the gab between the two broad band filters R and I, with only the narrow band 752 nm filter in between. As can be seen in Figure 4.6 the use of the $I2$ filter was able to reduce the redshift focusing in A226, but not to remove it completely.

4.4 COMBO-17+4 versus COMBO-17

To check the quality of our result we also compare the data achieved from the COMBO-17+4 survey with the results from the COMBO-17 survey. For this, we first have to identify the objects which are detected in both catalogs. As there is no information about right ascension and declination available in the COMBO-17 catalogs for neither the Abell 226 nor the S11 field we are forced to use pixel coordinates to identify identical objects. Since the optical data is shifted and rotated compared to the NIR data we use the same transformation matrix, as it is used during the reduction process for individual frames, to move them into a common coordinate system.

Before we compare the two surveys with each other we also have to mention again the differences between COMBO-17 and COMBO-17+4. In particular, the COMBO-17 survey use a different photometric setup file for the evaluate procedure (see Section 3.12) with a different PSF. In addition the *Asinh* system instead of the *upper limit* system of the COMBO-17+4 survey is used. The third difference is the exclusion of the sub procedure in the classification process (see Section 4.2).

4.4.1 Comparison of the Abell 226 Field

In the Abell 226 field 51,351 objects in the R band selected catalog from the COMBO-17 survey are found. As we restrict the limiting magnitude for the comparison to $H < 21.7$ mag, only 12,861 objects in the H band selected COMBO-17+4 survey are used. Especially blue objects at low redshift are missing in the new catalog, because they are not or only hardly visible in the H band. In total 9,182 objects are found which are visible in both catalogs.

The distribution of objects from both catalogs and the distribution of common objects over redshift can be seen in Figure 4.7 (upper panel). Here the black line shows the distribution of galaxies in the COMBO-17 survey, the red line the selected galaxies from the COMBO-17+4 survey and the green line only contains galaxies which are found in both surveys. At $z < 0.6$ both surveys have a very similar structure, but at higher redshifts the surveys show very different structures. This is caused due to the exclusion of the subprogram in the redshift determination process (see Section 4.2). In Figure 4.7 it is also visible that a lot of galaxies from the COMBO-17 survey are shifted to redshifts $z > 1$ due to the use of the four additional NIR filters in the COMBO-17+4 survey. We can therefore assume that especially in the redshift range of $0.8 < z < 1.0$ of the COMBO-17 survey a lot of objects actually have higher redshifts.

To check the improvement of the measured redshifts we compare the mea-

sured redshifts from the common galaxies in the COMBO-17 and COMBO-17+4 survey (see Figure 4.8, upper panel). The figure shows that a lot of objects from the COMBO-17 survey above $z > 0.8$ are indeed shifted to higher redshifts (even up to redshift $z = 2$). At lower redshifts the agreement between both surveys is in general very good. The little wiggles in this redshift range are the result of redshift focuses. These focuses have their origin in the use of the *Asinh* system, which is used for the COMBO-17 survey.

Like Nicol (2009) we find a population of galaxies which have low redshifts ($z < 0.3$) in the COMBO-17 survey, but very high redshifts in the COMBO-17+4 survey ($z > 1.4$). This population contains 164 galaxies, which are about 1.8% of the studied sample. For comparison, Nicol (2009) only counted 39 galaxies (0.5 % of her sample) in this redshift area. On the other hand we do not find a population of galaxies with high redshift values in the COMBO-17 survey and low redshifts in the COMBO-17+4 survey as Nicol (2009). The enhancement of the first population is highly likley caused by the exclusion of the subprogram in the redshift estimation process.

To minimize further misclassification in case of redshift we check the fitted templates of about a quarter of the galaxies which show a strong difference between the two surveys. With the exception of only a few objects all of them have very well fitted and reasonable looking templates. Therefore, we assume that the redshift calculation for the COMBO-17+4 survey is done as good as possible.

4.4.2 Comparison of the S11 Field

In the S11 field 52,451 galaxies in the R band selected catalog from the COMBO-17 survey are found. We restrict the limiting magnitude for the comparison again to $H < 21.7$ mag for the COMBO-17+4 catalog. In total 10,678 objects are found which are visible in both catalogs.

The distribution of objects of both catalogs and the distribution of common objects over redshift can be seen in Figure 4.7 (lower panel). Like for the A226 field the black line shows the distribution of galaxies in the COMBO-17 survey, the red line the selected galaxies from the COMBO-17+4 survey and the green line only contains galaxies which are detected in both surveys. Like in the A226 field both surveys show a similar structure at $z < 0.6$ and a different one at higher redshifts. We again see that a lot of galaxies from the COMBO-17 survey are shifted to $z > 1$. However, in the S11 field even a larger fraction of galaxies at $z > 1.6$ is found in both surveys. The results for the S11 field also supports our assumption that many galaxies from the COMBO-17 survey in the redshift range of $0.8 < z < 1.0$ indeed have higher redshifts.

Like in the A226 field we also want to see a direct comparison of the

measured redshifts in the COMBO-17 and the COMBO-17+4 survey for each galaxy (see Figure 4.8, lower panel). The distribution of the galaxies in this figure is almost identical to the distribution of the galaxies in the A226 field. Again we see a very good agreement between both surveys at $z < 0.8$ and the scattering at higher redshifts. Like in the A226 and the A901 field we also detect a population of galaxies with low redshifts ($z < 0.3$) in the COMBO-17 survey, but high redshifts ($z > 1.4$) in the COMBO-17+4 survey. This population contains 170 galaxies, which are 1.6 % of the sample. The relative number of this population has the same size as the population in the A226 field (1.8 %) and is three times larger than in the A901 field. Since we find an enlarged population in the S11 as well as in the A226 field, it seems reasonable that the exclusion of the subprogram in the redshift determination process led to this result.

In contrast to the A226 field, but in agreement with the A901 field we detect a second population of galaxies with large redshifts ($z > 0.5$) in the COMBO-17 survey and low redshifts ($z < 0.3$) in the COMBO-17+4 survey. 105 galaxies can be found in this area, which are 0.98 % of the sample. The same relative amount of galaxies is found in the A901 field (1.2 %). Again we check the fitted templates of about a quarter of these galaxies and again we find very well fitted templates for most of them. This supports our conclusion that the calculated photometric redshifts for the COMBO-17+4 survey are accurate.

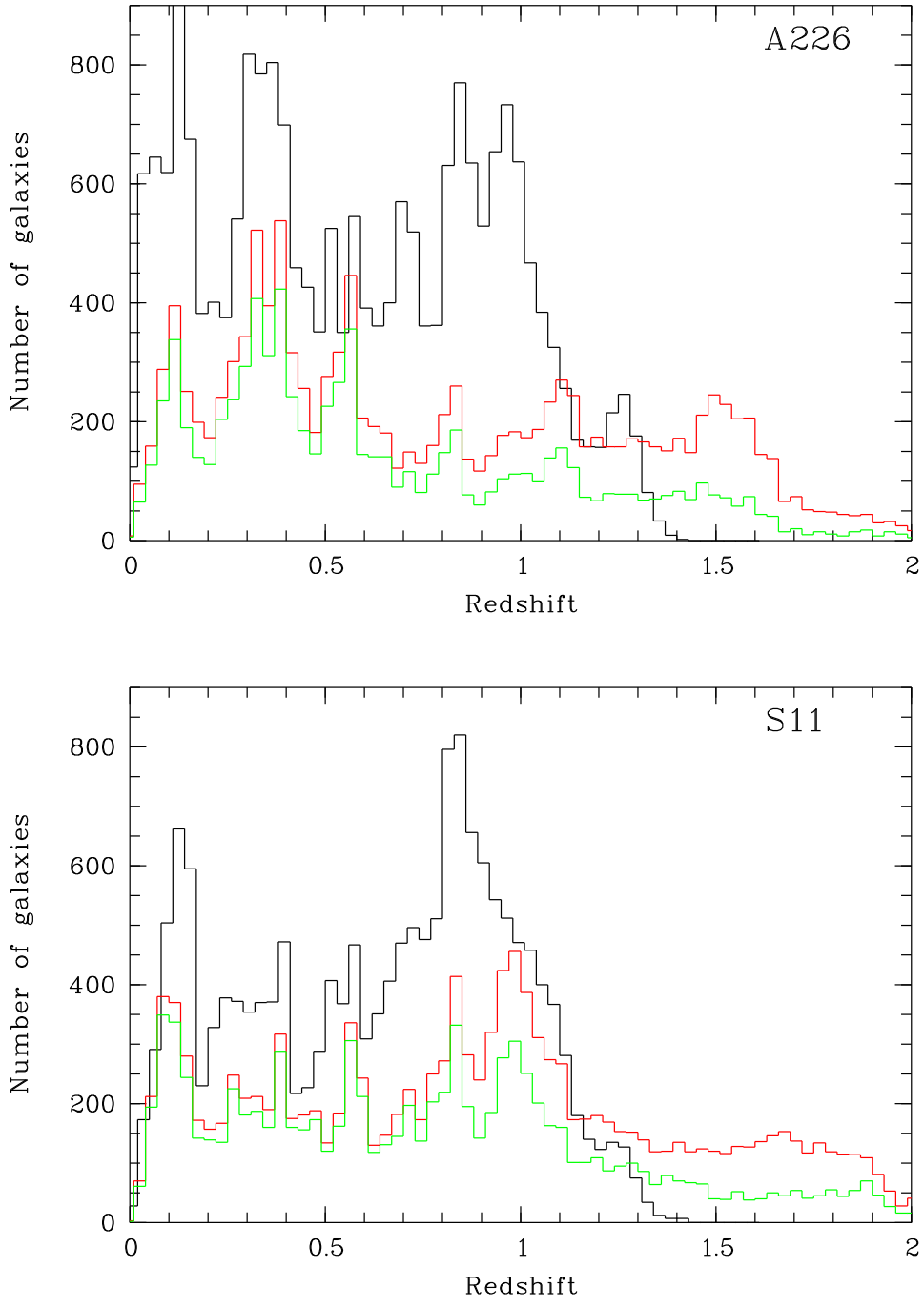

Figure 4.7: Comparison between the redshift distribution of galaxies in the COMBO-17 and the COMBO-17+4 survey. The black line shows all galaxies brighter than $R < 24.5$ mag from the COMBO-17 survey. The red line shows the galaxies from the COMBO-17+4 survey which are brighter than $H < 21.7$ mag. The green line only contains galaxies which are available in both catalogs. For plotting them the measured redshifts by the COMBO-17+4 survey are used.

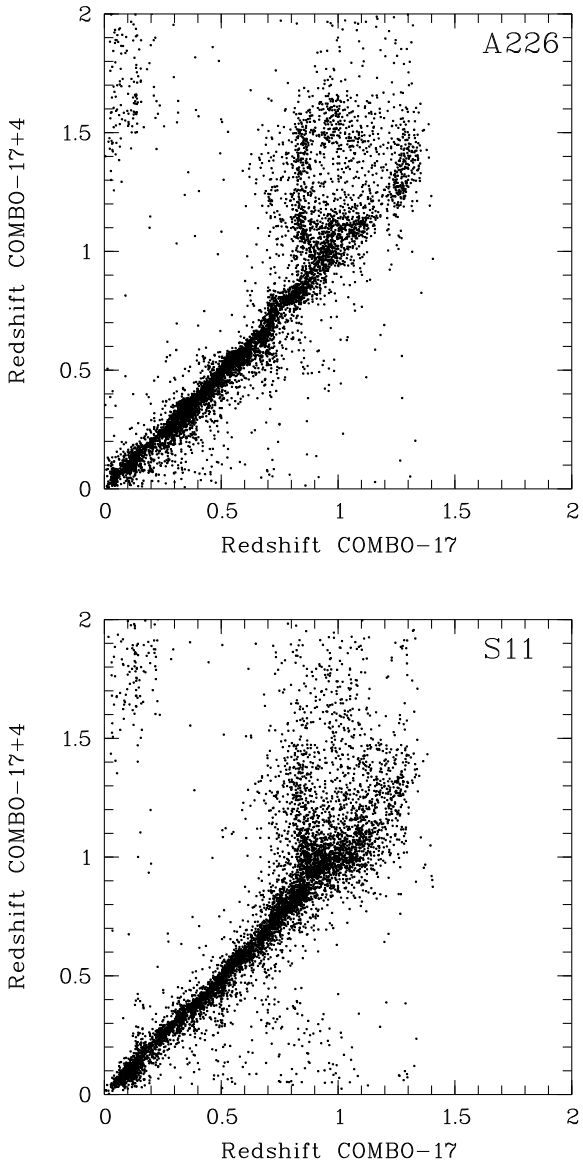

Figure 4.8: Comparison between the measured photometric redshifts from the optical data of the COMBO-17 survey and the optical plus NIR data of the COMBO-17+4 survey. Only galaxies detected in both surveys and within the magnitude cuts of $R < 24.5$ mag (for the COMBO-17 data) and $H < 21.7$ mag (for the COMBO-17+4 data) are shown.

Chapter 5

Evolution of the Red Sequence

In this section we explain how we calculate the rest-frame colors and absolute magnitudes using the measured fluxes and calculated redshifts. We also analyze the evolution of the bimodality of the galaxy population up to redshift $z = 2$. Within this chapter we are using the following cosmological parameters: $\Omega_m = 0.3, \Omega_\lambda = 0.7, H_0 = 70\text{km s}^{-1}\text{Mpc}^{-1}$.

5.1 Calculation of Rest-Frame Fluxes and Colors

So far we only used the measured colors, which are however not the real colors of our objects as the colors are redshifted. To investigate the evolution of the red sequence in the COMBO-17+4 survey and further to study the evolution of the luminosity and mass function, we have to calculate the rest-frame colors of the objects in our catalogs.

The measured fluxes of our objects are moved to redder wavelengths compared to their rest-frame wavelengths, due to redshifting. Therefore, we have to calculate the rest-frame magnitudes by calculating the flux for the closest

Table 5.1: The used filter to calculate the rest-frame luminosities for U_{280}, V and B respectively at different redshifts.

$M_{U_{280}}$ [mag] Redshift	Filter	M_V [mag] Redshift	Filter	M_B [mag] Redshift	Filter
$z < 0.80$	B	$z < 0.30$	V	$z < 0.30$	V
$0.80 < z < 1.04$	V	$0.30 < z < 0.80$	R	$0.30 < z < 0.73$	R
$1.04 < z < 1.71$	R	$0.80 < z < 1.39$	I	$0.73 < z < 1.39$	I
$z > 1.71$	I	$z > 1.39$	J1	$z > 1.39$	J1

broad band filter. The rest-frame magnitudes are calculated using the filters $U, B, V, R, I, J1$ and H. Using these broad band filters we calculate the rest-frame fluxes of three filters from the Johnson-system (U, B and V), the five filters from the SDSS (u, g, r, i and z) as well as an artificial UV band (U_{280}) with a central wavelength of $\lambda_c = 280$nm. Table 5.1 shows at which redshifts which broad-band filter is used to calculate the rest-frame fluxes of the filters U_{280}, V and B. These three filters are shown here, because they will be needed for the further analysis of the gathered data.

To calculate the rest-frame fluxes we use a color table which contains a k-correction color table. The information in this table originates from the templates stored in the galaxy library. The k-correction table contains observed versus rest-frame colors for all used broad band filters in the COMBO-17+4 survey plus the additional information for the Johnson- and ugriz-system in a three dimensional array of 6 extinction levels for 60 different types of SEDs (i.e. 360 templates) and 240 steps in redshift. The latter cove the range of $0 < z < 2.3$. Using these 86,400 possibilities of comparison we are able to calculate the rest-frame fluxes and magnitudes for each observed galaxy based on the observed flux.

By using the luminosity distance, the rest-frame magnitudes, the Equations 1.3, 1.4, 1.4 and 1.6, and the cosmological values assumed at the beginning of this chapter we are now able to calculate the absolute magnitudes of the detected galaxies. However, to get correct absolute magnitudes for extended objects we have to add a correction between the used aperture magnitudes in the flux table and the total magnitudes. For the correction the value of *MAG-BEST* derived by SExtractor is used and applied in a way that for stars the difference between total and aperture magnitude is zero. We perform a separate calibration for each subfield in S11 as Nicol (2009) did for the calibration of the A901 field. However, we do not calibrate for the different subfields in A226, because the correction factors of the four subfields are almost identical. Nicol (2009) also explained how the errors in luminosity are assumed: Additionally to the error of the magnitude in the observed filter to the redshifted rest-frame band and the error of MAG-BEST, a minimum error of 0.03 is assumed. The latter contains uncertainties in the redshift calculation and the calibration process.

With the so calculated rest-frame magnitudes and the absolute magnitudes, we are able to calculate rest-frame colors. As both used magnitudes for the color calculations have their own errors, the size of the final error is a quadratic addition from both filters. As for the calculation of the absolute magnitude, an additional minimum error of 0.05-0.1 is added. The exact value depends on the position of the rest-frame bands involved.

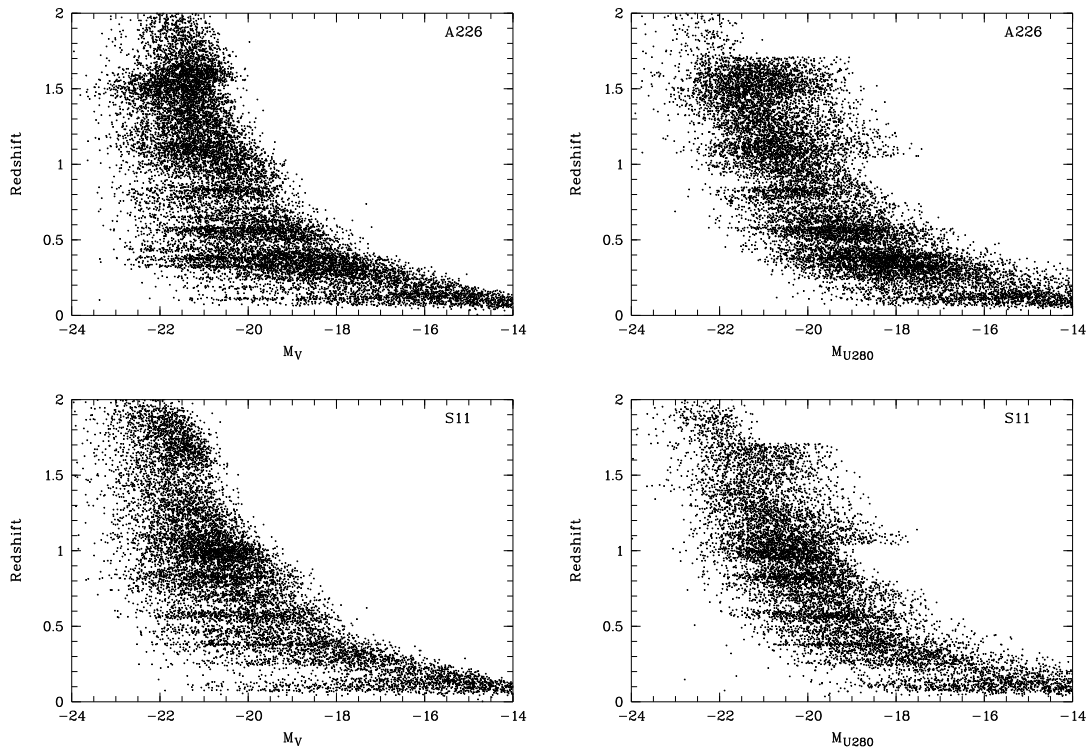

Figure 5.1: Evolution of the absolute magnitudes M_V and $M_{U_{280}}$ over redshift. The top panels show objects in the A226 field, whereas the bottom ones show the objects in the S11 field. Only galaxies brighter than the limiting magnitudes in the corresponding fields and magnitude errors lower 0.3 mag are shown.

5.2 Checking Absolute Magnitudes and Rest-Frame Colors

We are using the $(U_{280} - V)$ rest-frame color to investigate the galaxy bimodality and their evolution over cosmic time. Using the U_{280} filter instead of the common Johnson U band allows us to measure fluxes lower than the 4000 Å break better and in addition the $M_{U_{280}}$ rest-frame band as well as the M_V rest-frame band are both observable over the complete redshift range of $0 < z < 2$. Since our analysis on the evolution of the red sequence depends on this color, it is important to check and verify the calculated absolute magnitudes and rest-frame colors. We therefore investigate the evolution of galaxies in redshift using the color $(U_{280} - V)$ and we also examine the distribution of galaxies in the redshift-magnitude planes of M_V and M_{U280}. As a third point we check the evolution of the errors of $(U_{280} - V)$ in redshift.

For our analysis we exclude objects with errors >0.3 mag and of course we only use galaxies within the limiting magnitudes, as described in Section 4.3. Results for the distribution in the redshift-magnitude plane for M_V and

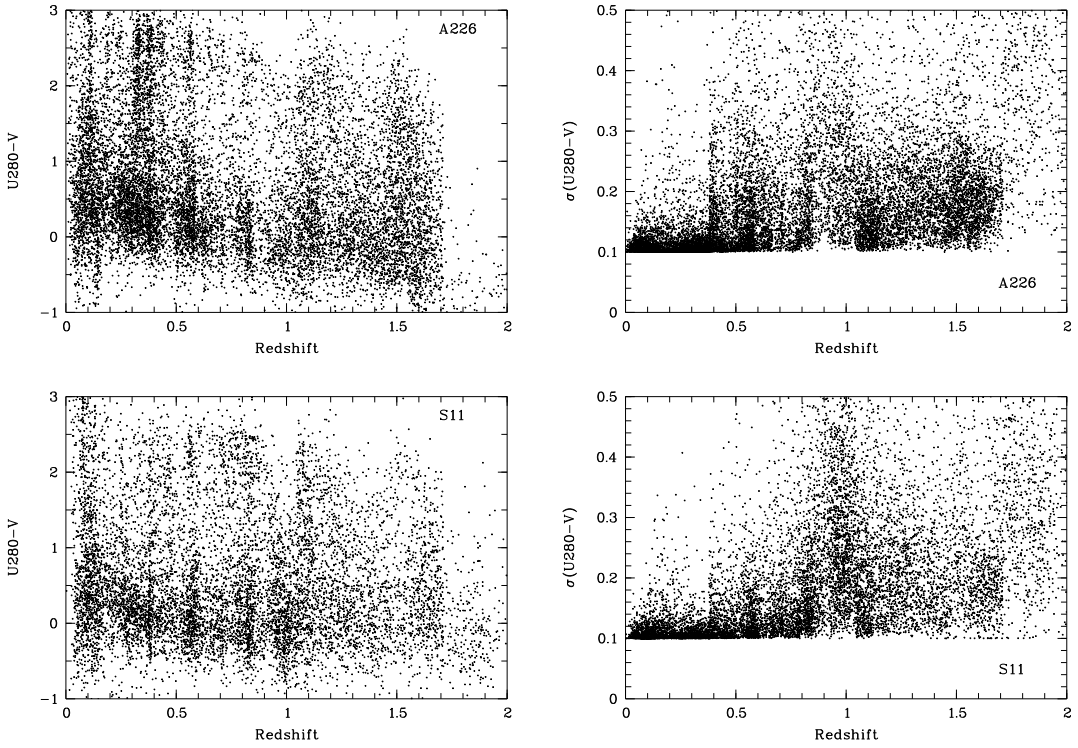

Figure 5.2: **Left panel**: Evolution of the rest-frame color $(U_{280} - V$ over redshift. **Right Panel**: $\sigma(U_{280} - V)$ as function of redshift. A minimum error of 0.1 mag is assumed. The top panels show objects in the A226 field, whereas the bottom ones show the objects in the S11 field. Only galaxies brighter than the limiting magnitudes and with $\sigma(U_{280} - V) < 0.3$ mag are used.

M_{U280} can be seen in Figure 5.1. In both figures of each field one can see at which redshift the rest-frame magnitudes are calculated using the observed R band: The R band is used to calculate M_V at $z < 0.38$ and to calculate $M_{U_{280}}$ at $1.04 < z < 1.71$. As the observed R band is deeper than the other optical filters, we are able to detect fainter objects in these redshift regimes. To calculate $M_{U_{280}}$ at $z > 1.71$ the observed I band is used. Compared with the S11 field we see only a small number of galaxies at $z > 1.71$ in the A226 field because the I band filter is not so deep as in the S11 field. The reason for this is the observation with the $I2$ filter in the A226 field.

Furthermore we investigate the evolution of the color $(U_{280} - V)$ in redshift. The left panels of Figure 5.2 show the result of this distribution. We are only using objects with an error in color smaller than 0.3 mag. The distribution of galaxies in the color-redshift plane shows the same structure as the distribution of SEDs in Figure 4.3 because the color of the galaxies is directly related with their SED type. This is simply because a star forming (or starburst) galaxy emits most of its light in shorter wavelengths (i.e. the U_{280} filter) than in longer ones (i.e. the V filter) and it is vice versa for red, evolved galaxies. The fact that

the same structures appear in the ($U_{280} - V$) diagram (Figure 5.2 left panels) as well as in the SED distribution (Figure 4.3) indicates that the calculation of the color is done correctly.

Finally we check how $\sigma(U_{280} - V)$ changes with redshift. All galaxies have an assumed minimum error of 0.1 mag. The transitions between used filters to calculate the rest-frame color are visible as increases and decreases in the average scattering of the errors – depending on the observed fluxes used. Within the A226 field we see a large scattering at low redshifts ($0.1 < z < 0.3$). This problem is caused by large errors in M_V and $M_{U_{280}}$. At $z < 0.3$ the observed V and the observed B band is used to calculate the corresponding rest-frame magnitudes and both filters show large errors in the A226 field. Because our observed B band shows smaller errors in the S11 field we do not see a large scattering at $z < 0.8$. The increase in scattering at $0.8 < z < 1.07$ in both fields is caused by the use of the filters V and $J1$ which are used to calculate $M_{U_{280}}$ and M_V respectively. In the A226 field we again see the reduction in the number of galaxies at $z > 1.7$, which is caused by the observed I filter (which is used to calculate $M_{U_{280}}$).

5.3 Error-Weighted Color Histograms

To analyze the accurate distribution of red and blue galaxies in different redshift slices and the evolution of the red sequence in particular, we use error-weighted color histograms. In these histograms each galaxy is represented by a Gaussian probability distribution: $p \sim e^{-(c-c_0)^2/2\sigma_c^2}$, where σ_c is the error of the color and p is normalized so that $\int pde = 1$. This means that galaxies with a large error have a broad Gaussian curve and contribute only weakly to the distribution of galaxies. However, galaxies with a small error lead to a distribution with a sharp peak and these galaxies contribute strongly to the distribution in the histogram. Again, we analyzed the bimodality using the color ($U_{280} - V$). For both fields we create up to 25 histograms which show the evolution of both galaxy populations in different redshift areas and different volumes in the redshift range between $0.2 < z < 2.0$. As the number of galaxies is dropping drastically at higher redshifts we use larger volumes at higher redshifts to identify the red sequence. This enhances our chances to find the red sequence even at these high redshifts, despite the low number counts of galaxies.

Each histogram gives the lower and upper end of the analyzed redshift range and the total number of galaxies within this redshift range. A selection of created histograms for the Abell 226 field can be seen in Figure 5.3, histograms for the S11 field can be seen in Figure 5.4. As the galaxies in the histograms are weighted on their error in color we do not have to make an error cut, but

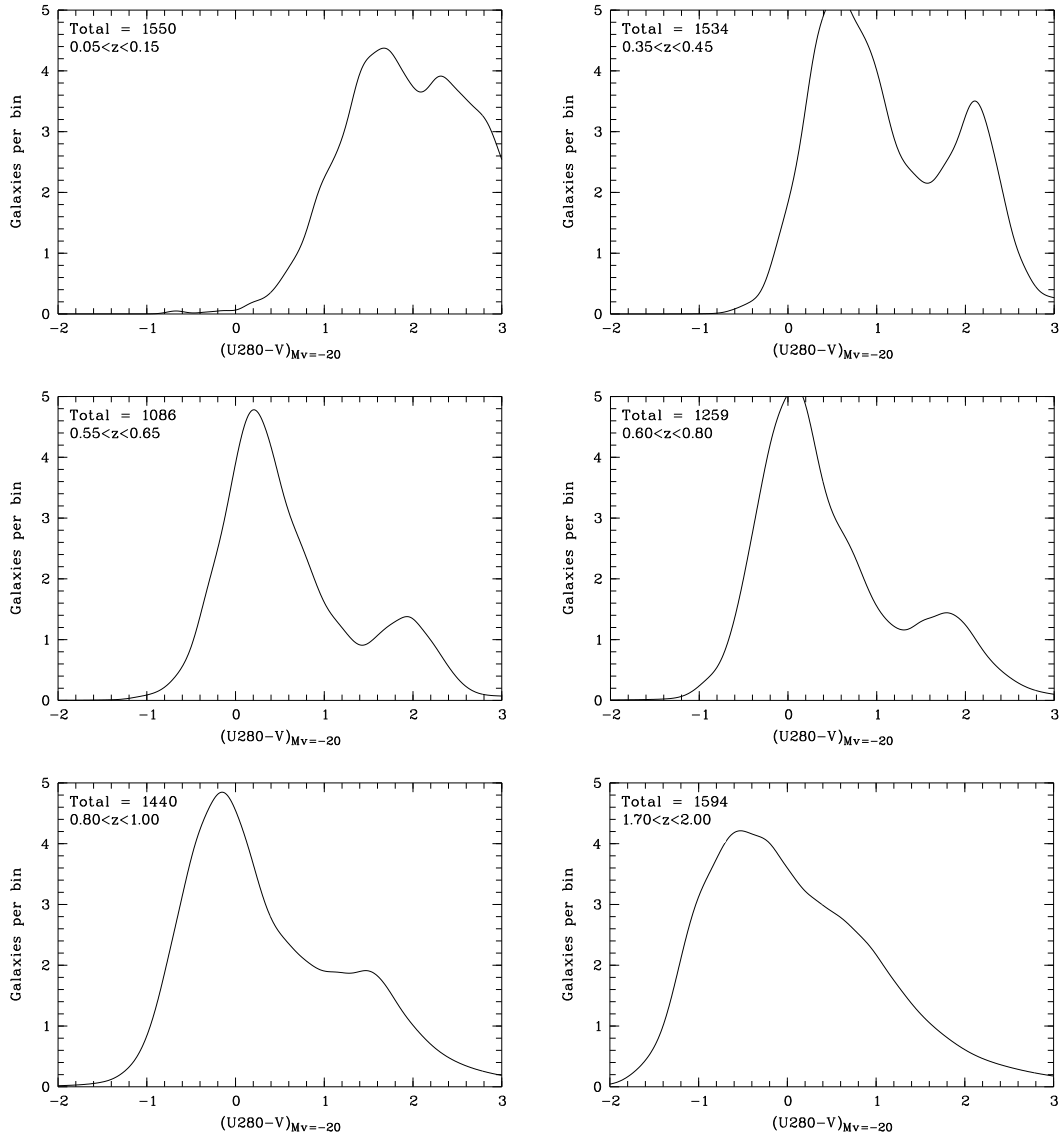

Figure 5.3: Several error-weighted color histograms for the A226 field, which are used to study the evolution of the red sequence in color (see Figure 5.5). The total number of galaxies and upper and lower end of the redshift interval are given for each redshift slice. Up to a redshift of $z \sim 1$ a red galaxy population can be seen, which is separated from the blue population through a valley. At higher redshift this valley and therefore also the separation vanishes.

still only galaxies within our limiting magnitude ranges are used. In many histograms at redshifts $z < 1.2$ two clear peaks are visible: the bluer peak indicates the galaxies of the blue cloud and the redder peak the existence of a separated red sequence. The position of both peaks is moving to bluer colors at higher redshifts which supports the cosmological picture of an evolution from a young, gas rich galaxy population at higher redshift to a less gas rich, older

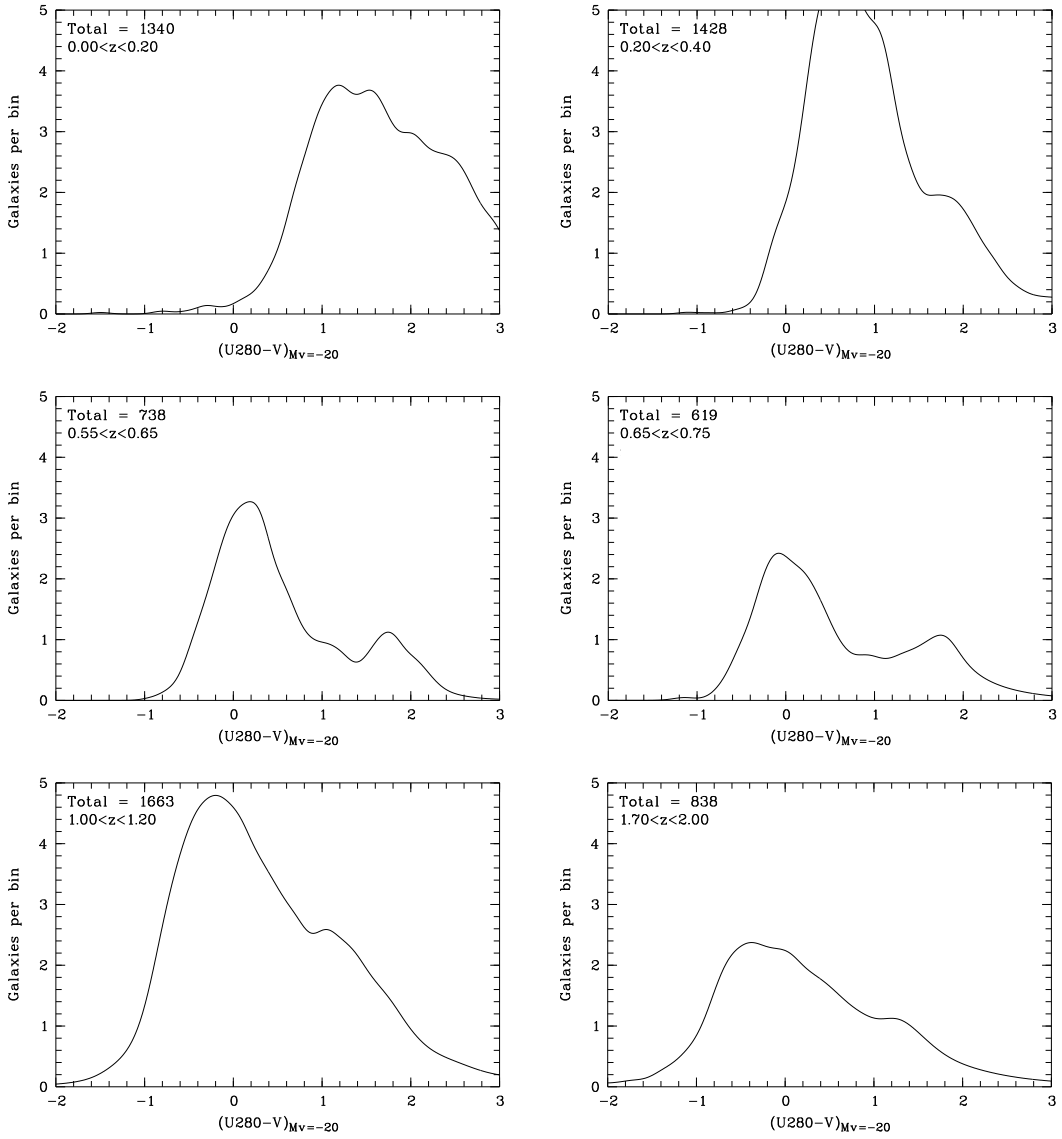

Figure 5.4: Several error-weighted color histograms for the S11 field, which are used to study the evolution of the red sequence in color (see Figure 5.5). The total number of galaxies and upper and lower end of the redshift interval are given for each redshift slice. Up to a redshift of $z \sim 1$ a red galaxy population can be seen, which is separated from the blue population through a valley. At higher redshift this valley and therefore also the separation vanishes.

population in the modern Universe. However, the red sequence cannot be seen in all histograms at lower redshifts. As it disappears in different redshift areas in the three different fields of the COMBO-17+4 survey we are sure that it is the result of cosmological variations and not real evolutionary effect. However, this result shows the need to study different fields of view for cosmological studies.

In the A226 field we prove the existence of the red sequence up to a redshift of $z \sim 1.2$ and in the S11 field up to a redshift of $z \sim 1.3$. In the S11 field we can also see a little bump in the histogram for the redshift range $1.7 < z < 2.0$ (see Figure 5.4, panel on the bottom right) but the bump is not distinctive enough to measure the position of its peak. Nicol (2009) found a red sequence for the A901 field up to $z = 1.6$. Our results are supported by those of Bell et al. (2004b) who found a clear evidence of the red sequence at $0.1 < z < 1.1$ using data from the COMBO-17 survey. Also Taylor (2008) found the red sequence up to $z = 1.2$ using the MUSYC survey. Franzetti et al. (2006) found evidences for the red sequence up up $z = 1.5$ using the VVDS survey. However, we are not able to verify the results of Kriek et al. (2008) and Williams et al. (2009) who both found indications for a red sequence up to $z = 2$. While Kriek et al. (2008) only used a small, preselected sample of red galaxies from the MUSYC survey, Williams et al. (2009) analyzed 90,000 galaxies from the UKIDSS data which means they had double the amount of galaxies than we have in the COMBO-17+4 survey. Still, the bump in the redshift bin $1.70 < z < 2.00$ in the S11 field indicates, that the red sequence might exits at $z > 1.3$.

5.4 Evolution of Galaxies in the Color-Magnitude Plane

To distinguish between galaxies in the blue cloud and galaxies in the red sequence we use the same method as Nicol (2009). She used the error-weighted color histograms from the Abell 901 field to distinguish between the two galaxy populations, using the measured $(U_{280} - V)$ color with $M_V = -20$ as pivot point:

$$(U_{280} - V)_{M_V=-20} = (U_{280} - V) + 0.3(M_V + 20). \tag{5.1}$$

With the error-weighted color histograms she found a linear evolution of the red sequence in color: $(U_{280} - V)_{M_V=-20} = 2.57 - 0.195 \times t_{\text{lookback}}$. A linear approximation for the lookback time of $t_{\text{lookback}} = 15$ Gyrs $z(1+z)^{-1}$ was assumed. Using the error-weighted color histograms for the Abell 226 and S11 fields (see Figures 5.3 and 5.4) the general evolution of the red sequence is verified. However, we find a large offset to the red in the evolution in the Abell 226 field, which leads to the following evolution of the red sequence:

$$(U_{280} - V)_{M_V=-20} = 2.92 - 0.192 \times t_{\text{lookback}}. \tag{5.2}$$

On the other hand, the evolution of the red sequence in S11 is almost identical to the evolution of the red sequence identified in the A901 field by Nicol

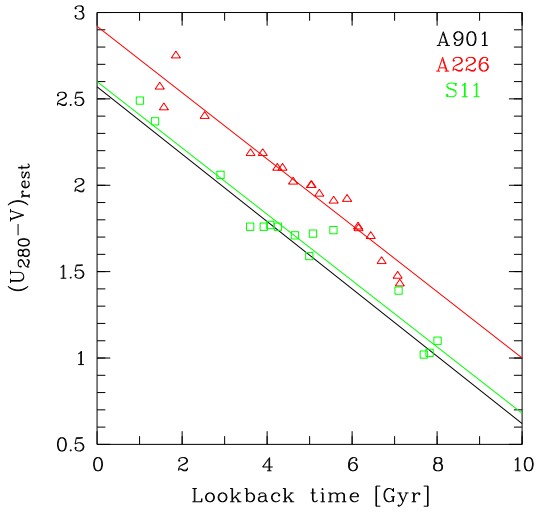

Figure 5.5: The red line indicates the evolution of the red sequence in the Abell 226 field and the green line in the S11 field. The lines are based on measurements in the error-weighted color histograms at different lookback times (red triangles for A226 and green squares for S11). The black line indicates the evolution found by Nicol (2009) in the Abell 901 field.

(2009):

$$(U_{280} - V)_{M_V=-20} = 2.60 - 0.192 \times t_{\text{lookback}}. \tag{5.3}$$

The measured evolutions of the red sequence in the A226 and the S11 field, as well the one measured by Nicol (2009) are compared in Figure 5.5. Here, the offset between the red sequence in the fields of Abell 901 and S11 to the Abell 226 field is obvious. However, the slope of the lines is almost identical.

Using Equation 5.1 and the resulting equations from A226 and S11 (Equations 5.2 and 5.3) an accurate limiting color, which distinguish the blue cloud from the red sequence in the color-magnitude plane is established. However, because Equations 5.2 and 5.3 show the evolution of the center of the red sequence we use a separating line which is 0.47 mag bluer than this evolutionary line. This empirically determined value will guarantee, that our separating line is placed in the green valley. This leads to the limiting colors for A226 and S11:

$$(U_{280} - V)_{\text{lim}_{\text{A226}}} = 2.45 - 0.3(M_V + 20) - \frac{2.88z}{1+z}, \tag{5.4}$$

$$(U_{280} - V)_{\text{lim}_{\text{S11}}} = 2.13 - 0.3(M_V + 20) - \frac{2.88z}{1+z}. \tag{5.5}$$

Galaxies are defined as red, if $(U_{280} - V) > (U_{280} - V)_{\rm lim}$ and defined as blue if $(U_{280} - V) < (U_{280} - V)_{\rm lim}$. A separation between the two populations using $(U_{280} - V)$ was also used by Phleps et al. (2006) and Simon et al. (2009) for the COMBO-17 survey so we are able to compare our results up to $z = 1$ with previous ones. We compare our resulting Equations 5.4 and 5.5 with the evolving magnitude relation derived by Bell et al. (2004a). Bell et al. used a sample of 1,500 galaxies from the GEMS project in conjunction with the COMBO-17 survey. We find a very good agreement between our result from the S11 (Equation 5.5) and the A901 field and the results by Bell et al. (2004b), with the only difference that the relation between color and magnitude derived for S11 and A901 are a bit steeper.

A reason for the offset of the red sequence in the A226 field compared to the other two fields cannot be found. However, in checking the color magnitude diagrams of the A226 field in different areas of redshift we discover that in using the limiting color of the S11 field, we still will not include galaxies from the blue cloud to the red sequence. It therefore seems that the red sequence in the A226 field is redder than in the other two fields – out of unknown reasons –, but the blue cloud is found in the same color-magnitude area in all three fields. As we want to combine all three fields of the COMBO-17+4 survey to one catalog we decide to use the separating color of the S11 field for all three fields of the survey:

$$(U_{280} - V)_{\rm lim_{COMBO\text{-}17+4}} = 2.13 - 0.3(M_V + 20) - \frac{2.88z}{1+z}. \qquad (5.6)$$

5.4.1 Galaxies in Color-Magnitude Diagrams

Using Equation 5.6 we are able to create color-magnitude diagrams for the galaxies in the COMBO-17+4 survey in different redshift slices in the range of $0 < z < 2$. Within the diagrams we also show the separating line between the red sequence and the blue cloud in green and we highlight the galaxies of the red sequence in red. We create CMDs for ten redshift bins, covering the redshift range from $z = 0.0$ to $z = 2.0$. In the redshift range from $z = 0.2$ to $z = 1.3$ the bins enclose equal comoving volumes, whereas the three highest redshift bins enclose a comoving volume 2.5 times larger than the others.

Due to large errors in the color of $\sigma > 0.5$ mag at redshifts larger $z > 1$ it is not easy to identify galaxies which are clearly members of the red sequence. To exclude galaxies with large errors, we only plot objects with $\sigma(U_{280} - V) < 0.5$ mag in the CMDs. As we now have established a selection criteria for red and blue galaxies, we also create a histogram, which showes the distribution of galaxies in both fields between $0 < z < 2$ (see Figure 5.6). This distributions already shows that the number of red galaxies in general is low compared to

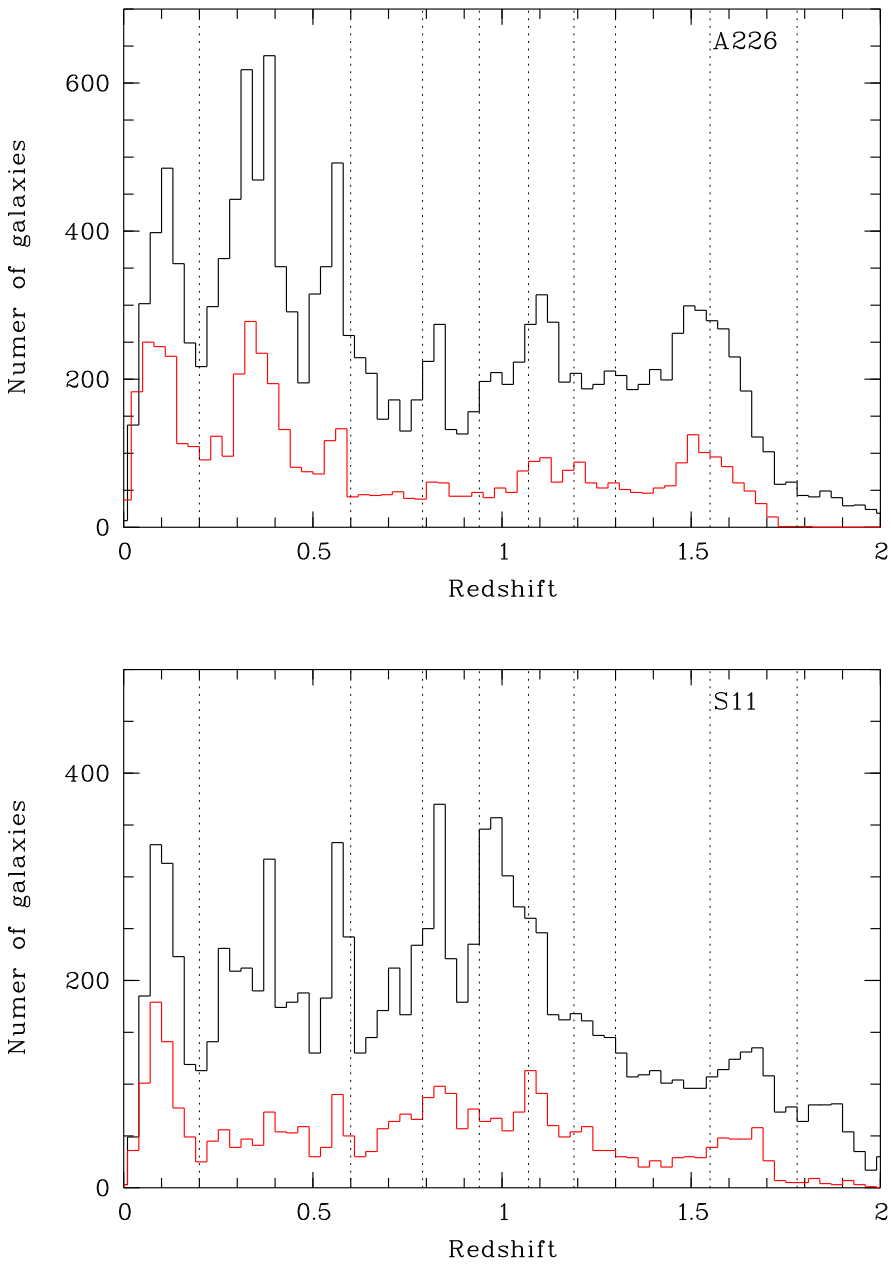

Figure 5.6: The plot shows the distribution of galaxies in the red sequence (red) of the A226 and S11 field in z as well as the distribution of all galaxies which are analyzed in the corresponding fields. The dotted line indicate the redshift slices which are used to plot the color-magnitude diagrams in the Figures 5.7 to 5.10.

the total number of galaxies, and that there are hardly any red galaxies left at redshifts $z > 1.5$. At $z > 1.7$ we do not see any red galaxies in the Abell 226 field at all, which means that the red sequence disappeared within the analyzed redshift range.

The ten different redshift bin we analyze for the A226 field can be seen in Figures 5.7 and 5.8. The separating green line is based on Equation 5.5 from the S11 field. As comparison the separating line based on the A226 field is shown as well (black dashed line). As we used the mean redshift of each redshift bin to calculate the position of the dividing line, a few galaxies of the red sequence can be found beyond the limiting color magnitude and blue galaxies can be found above the line.

We find red galaxies in all our redshift bins. However in the redshift range of $1.78 < z < 2.00$ only two red galaxy can be seen. The red sequence itself is clearly visible in other redshift slices at lower redshifts. The sequence seems to get fainter at $z > 1$ and eventually disappears completely in the redshift slice $1.19 - 1.30$. This means that in the Abell 226 field the red sequence is visible until higher redshifts than in the Abell 901 where the sequence in the CMDs seemed to disappear at $z \sim 1.10$ (Nicol, 2009).

To analyze the S11 field we use the same redshift slices as for the A226 field. The corresponding results can be seen in Figures 5.9 and 5.10. Only the separating line based on Equation 5.5 is shown. As in the A226 field we find red galaxies in all redshift bins. However, we find a larger population of 25 red galaxies in the redshift range of $1.78 < z < 2.00$. The red sequence itself is visible (and measurable) up to a redshift of $z \sim 1.30$. Remarkable is the redshift slice in the interval $0.79 < z < 0.94$ in which the red sequence seems to be separated differently from the blue cloud as in the other redshift intervals, as it is ~ 0.2 mag redder than the separating line. However, no galaxies which are definitely from the blue cloud seem to be added to the red sequence in the redshift interval.

We use the CMDs not only to verify our calculated separating line of the red sequence but also to check and exclude further objects from our catalogs. We check the measured fluxes of very bright, blue objects, as these objects do not exist in the known Universe. Most of these galaxies are indeed false classified stars or artifacts, but we also find some false classified galaxies within these objects. All of these objects are removed from the catalogs.

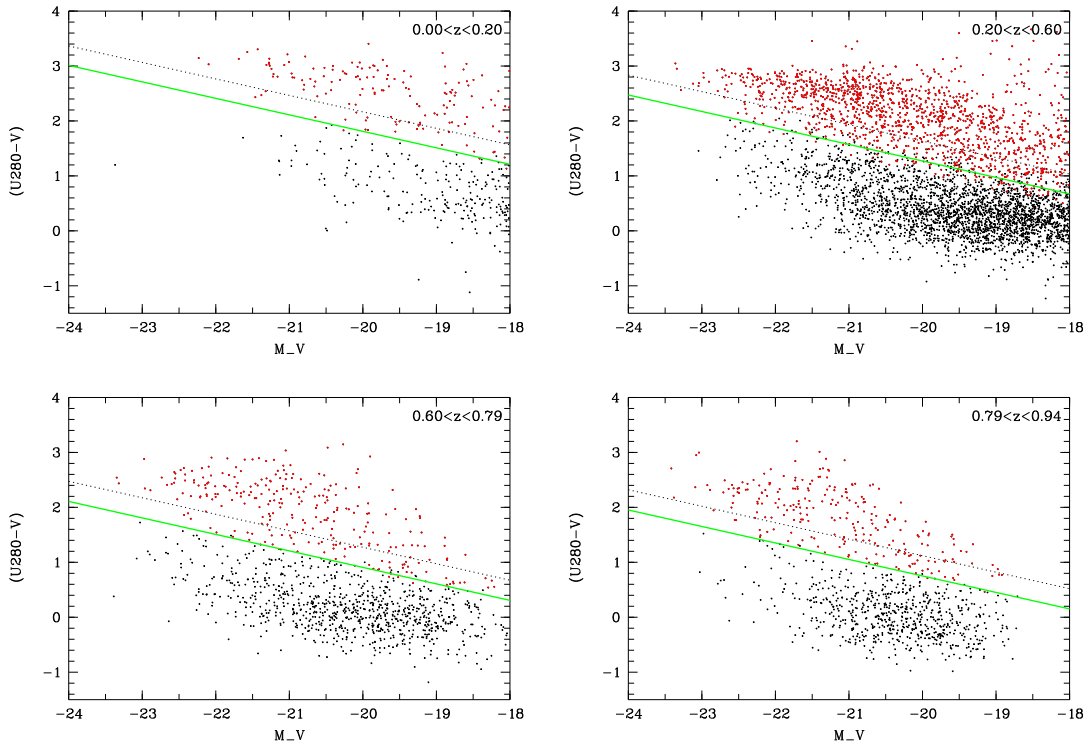

Figure 5.7: CMDs for galaxies in the Abell 226 field for different redshift bins as indicated on each panel. Only galaxies within the limiting magnitudes and with an error $\sigma < 0.5$ in color are shown. The green line – calculated using Equation 5.6 – shows the separation line between the blue cloud and the red sequence. The black dotted line shows the separation based on Equation 5.4. Galaxies above the separating line are members of the red sequence and highlighted in red.

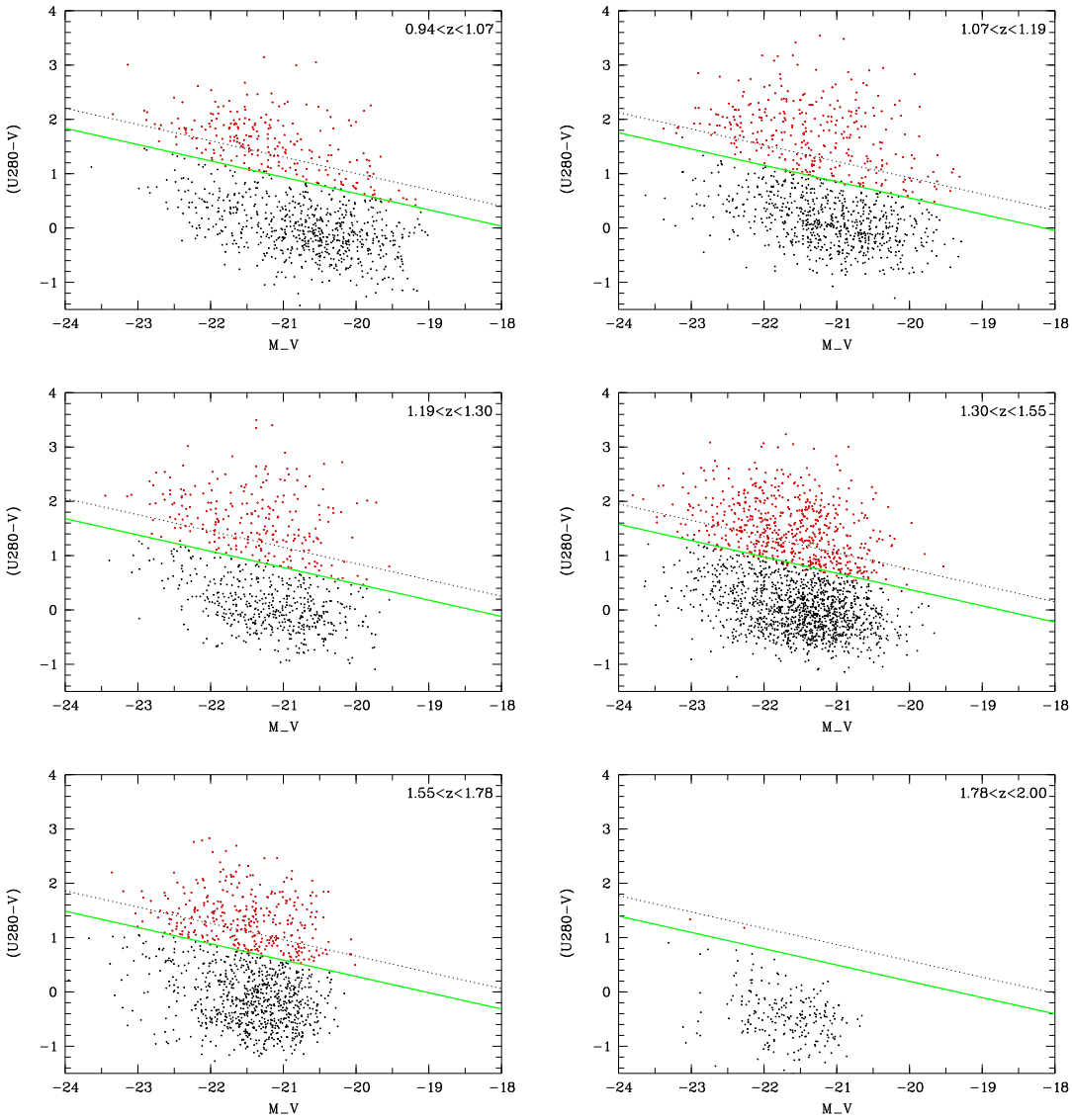

Figure 5.8: CMDs for galaxies in the Abell 226 field for different redshift bins as indicated on each panel. Only galaxies within the limiting magnitudes and with an error $\sigma < 0.5$ in color are shown. The green line – calculated using Equation 5.6 – shows the separation line between the blue cloud and the red sequence. The black dotted line shows the separation based on Equation 5.4. Galaxies above the separating line are members of the red sequence and highlighted in red.

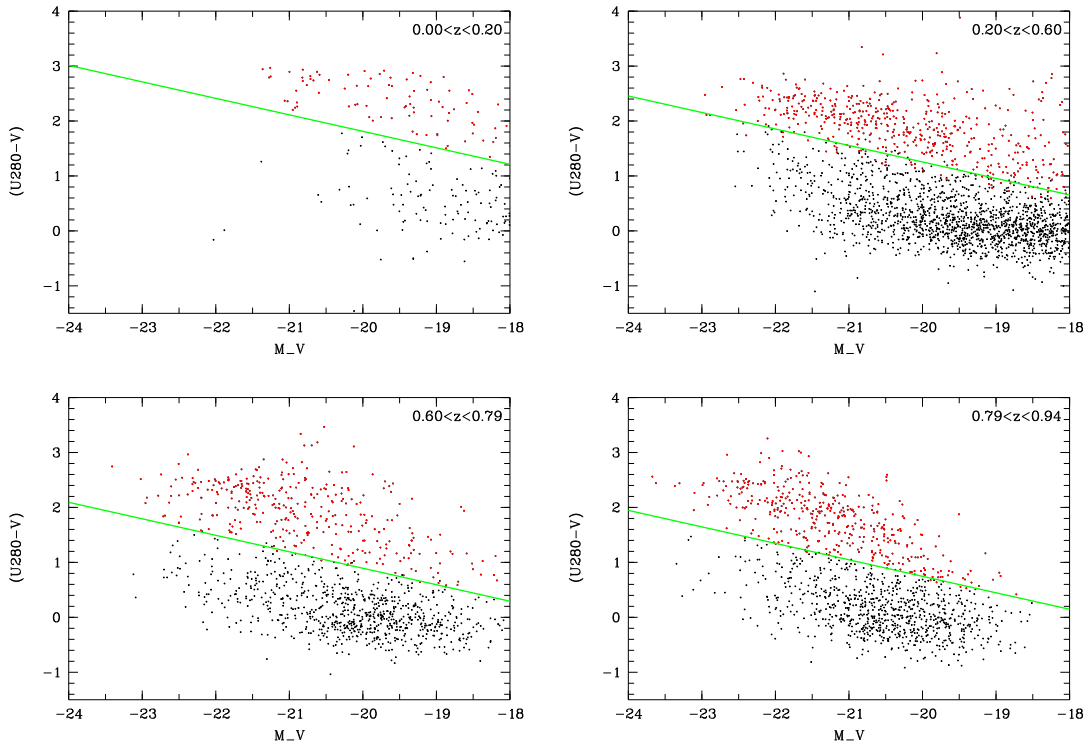

Figure 5.9: CMDs for galaxies in the S11 field for different redshift slices as indicated on each panel. Only galaxies within the limiting magnitudes and with an error $\sigma < 0.5$ in color are shown. The green line – calculated using Equation 5.6 – shows the separation line between the blue cloud and the red sequence. Galaxies above the separating line are members of the red sequence and highlighted in red.

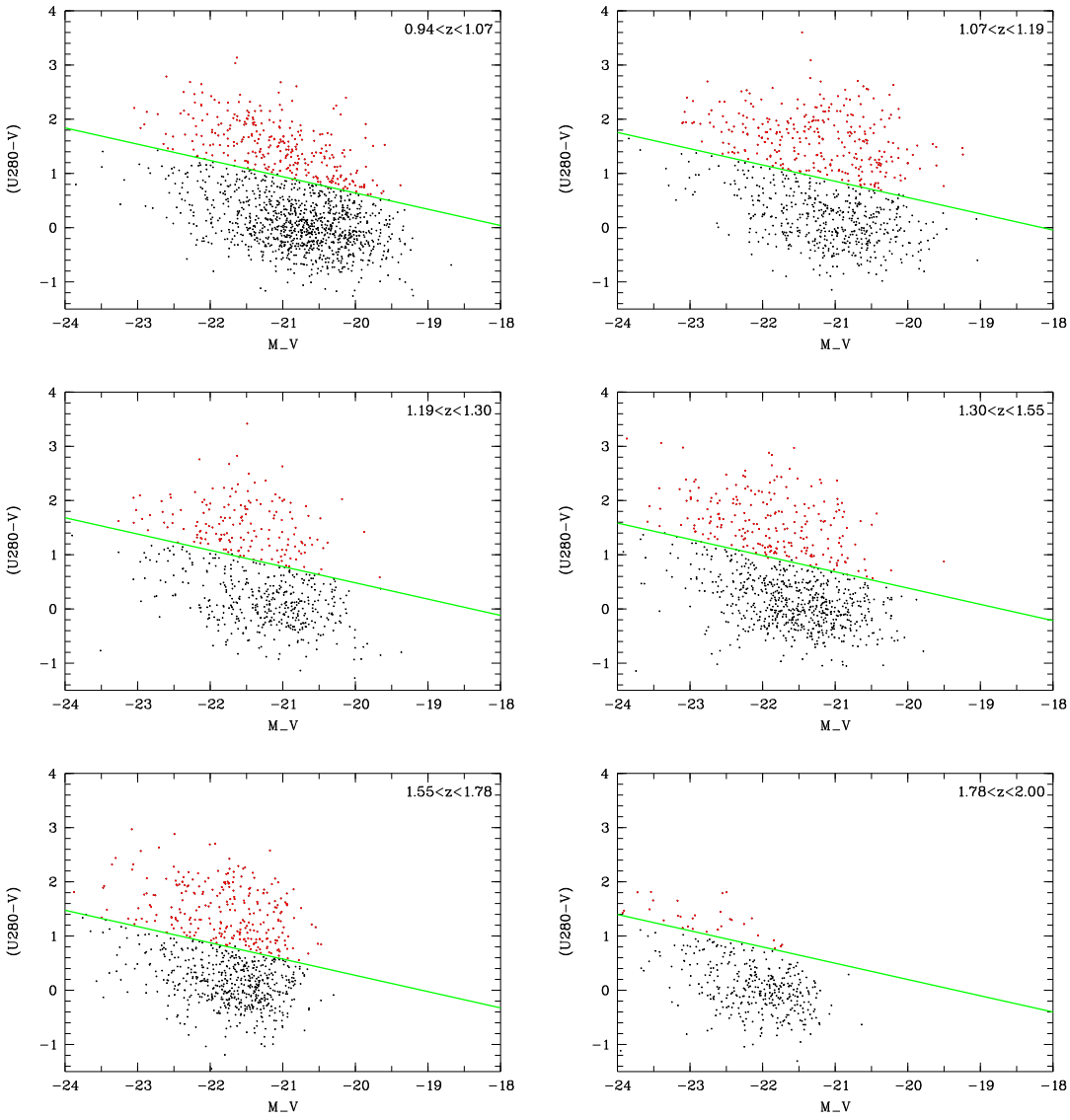

Figure 5.10: CMDs for galaxies in the S11 field for different redshift slices as indicated on each panel. Only galaxies within the limiting magnitudes and with an error $\sigma < 0.5$ in color were used. The green line – calculated using Equation 5.6 – shows the separation line between the blue cloud and the red sequence. Galaxies above the separating line are members of the red sequence and highlighted in red.

Chapter 6

Luminosity Function

After classifying the detected objects and separating them into a blue and a red population we investigate the luminosity functions of the galaxies in the different fields of COMBO-17+4. We analyze the blue and the red galaxy population separately as previous studies showed a different evolution of these two populations. In this chapter we are going to investigate the change of the characteristic magnitude M^* the normalization factor Φ^* and the number density over cosmic time.

6.1 Definition and Calculation of the Luminosity Function

The study of the luminosity function in cosmic time helps us to understand the evolution of the galaxies themselves, as the luminosity functions are directly tied to the stellar populations and star formation histories of the galaxies. This means if we analyze the evolution of the luminosity function in different redshift slices it will help us to understand how the galaxies in our survey evolved since $z = 2$.

6.1.1 Definition of the Luminosity Function

The luminosity function was first created by Schechter (1976) – for this reason it is often also called the Schechter function:

$$\Phi(L) = \left(\frac{\Phi^*}{L^*}\right)\left(\frac{L}{L^*}\right)^{\alpha} \exp\frac{-L}{L^*} \tag{6.1}$$

where Φ^* is defined as the normalization of the distribution, L^* is the characteristic luminosity, $\Phi(L)$ is the number density of galaxies in the luminosity range [L, L+dL] and α describes the slope at the faint end of the luminosity function. The Schechter function can also be expressed in magnitudes:

$$\Phi(M) = (0.4 \ln 10)\Phi^* 10^{0.4(\alpha+1)(M^*-M)} \exp(-10^{0.4(M^*-M)}) \tag{6.2}$$

In this equation the luminosity is replaced with magnitudes, meaning that L^* is replaced with the characteristic magnitude M^* and $\Phi(L)$ with $\Phi(M)$ – the number density of galaxies in the magnitude range [M, M+dM]. Already Schechter (1976) mentioned that the correct calculation of the luminosity is not easy as for a representative function, a large number of galaxies in a large volume has to be studied. However, this should not be a problem for the creation of luminosity functions in the COMBO-17+4 survey.

The galaxy function itself is defined as the number of galaxies in a magnitude range and is expressed in units of galaxies per Mpc^3. Binney and Merrifield (1998) normalized the function so that:

$$\int_{-\infty}^{\infty} \Phi(M) dM = \nu, \tag{6.3}$$

where ν is the total number of galaxies per unit volume. The shape of the luminosity function describes the distribution of galaxies with different magnitudes in the corresponding redshift bins and in general shows that the number of galaxies is decreasing with increasing magnitudes. Therefore, the shape of the luminosity function supports the bottom up scenario of modern cosmology. From the faintest to the brightest galaxies the luminosity function decreases with a power law index α until it reaches the characteristic magnitude M^* from where on it is cut off rapidly. These two free parameters are also connected with the normalization factor Φ^* – which is also a free parameter. For the analysis of the luminosity function one parameter is normally fixed to determine the other two more easily. We decide to use a fixed slope α like it was already done by Nicol (2009) to make our results comparable.

6.1.2 Calculation of the Luminosity Function

There are several methods to calculate the luminosity function with different advantages and disadvantages; Binggeli et al. (1988) alone list 13 different methods and in their historic overview, Willmer (1997) describe 15 methods and their variations. The first determinations of the luminosity function were made with the now so called classical method in which the number of objects in a given volume is simply counted (Hubble, 1936). This method is very simple, however assumed a very uniform distribution of galaxies in space.

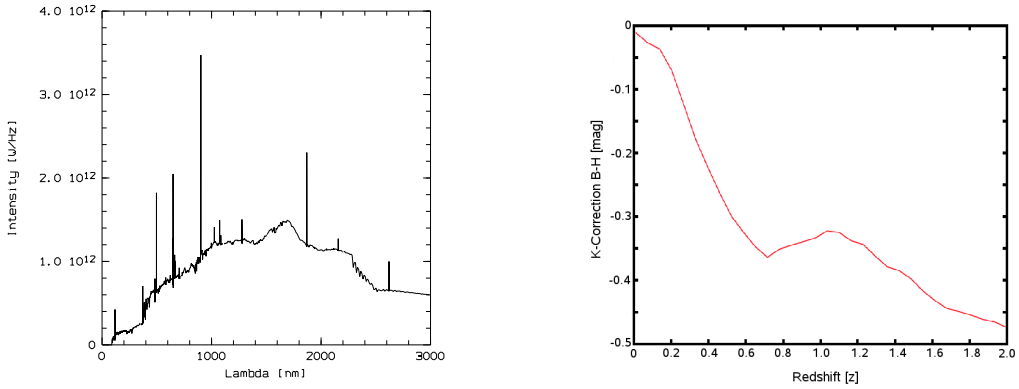

Figure 6.1: **Left panel:** The spectral energy distribution of SED #30 which is used to calculate the k-correction in order to get $z_{\max}$. **Right panel:** The k-correction which is used to calculate $z_{\max}$ as a function of redshift. The function is normalized so that $K(z = 0) = 0$ (Bartelmann, priv. communication).

The first method which tried to overcome the assumption of an uniform distribution is the C^--method by Lynden-Bell (1971). This maximum likelihood method has the disadvantage that the same shape of the luminosity function for all points along the line of sight is assumed. One of the first methods which allowed for the correction of incompleteness and canceled out the contribution of density distribution is the STY[1] method by Sandage et al. (1979). This method uses a parametric maximum-likelihood estimator and is often used for the calculation of luminosity functions until today.

For the analysis of the luminosity function in the COMBO-17+4 survey the non parametric estimator $1/V_{\max}$ by Schmidt (1968) – which was originally created to study quasars – is used to calculate the luminosity function in different redshift areas. The great advantage of this method is the fact, that it takes into account a weight inversely proportional to the luminosity of the analyzed objects. It corrects for galaxies, which are too faint to be observed at the redshift of interest and which are excluded from our sample due to the magnitude limits we established. In addition the method allows us to determine the shape and the normalization parameter Φ^* of the luminosity function simultaneously. However, $1/V_{\max}$ in contrast to the STY and similar methods is sensitive for inhomogeneities in the distribution of the galaxy population as it assumes uniformly distributed objects. Since we analyze three different fields in the COMBO-17+4 survey cover 0.625 square degrees in total, the uncertainties should be small as long as we are looking at the whole survey at once and not only at a single field.

The luminosity function by the $1/V_{\max}$ method is given as the sum of the density contribution of each galaxy in a specific SED, magnitude and redshift

[1]STY: **S**andage, **T**ammann, **Y**ahil

bin:

$$\Phi(M)dM = \sum_i \frac{1}{V_i(M, z, SED)} \tag{6.4}$$

where $V_i(M, z, SED)$ is defined as the total comoving volume in which the galaxy i can be detected. The comoving volume itself is defined as

$$V_i(M, z, \mathrm{SED})_{\geq} = \Delta\Omega \int_{z_{\mathrm{lower}}}^{z_{\mathrm{upper}}} \frac{dV}{d\Omega dz} dz \Big\{ \text{ for } z_{\mathrm{max}} \geq z_{\mathrm{upper}}, \tag{6.5}$$

$$V_i(M, z, \mathrm{SED})_{<} = \Delta\Omega \int_{z_{\mathrm{lower}}}^{z_{\mathrm{max}}} \frac{dV}{d\Omega dz} dz \Big\{ \text{ for } z_{\mathrm{max}} < z_{\mathrm{upper}}. \tag{6.6}$$

In these equations the comoving volume $V_i(M, z, \mathrm{SED})_{\geq}$ is delimited by z_{lower} and z_{upper} (lower and upper and of analyzed redshift bin). For the size of the comoving volume also $\Delta\Omega$, the effective solid angle of the field, is necessary. Finally, z_{max} gives the maximum redshift up to which a galaxy with certain (M, z, SED) will be detected within the limiting magnitudes of the survey.

Using the $1/V_{\mathrm{max}}$ method, each galaxy in our survey is tested if it is bright enough to be seen up to z_{upper} ($z_{\mathrm{max}} \geq z_{\mathrm{upper}}$) of the redshift bins we are interested in. If the galaxy is visible until z_{upper} we count 1 galaxy per $V_i(M, z, \mathrm{SED})_{\geq}$ (see Equation 6.5). However, if the galaxy is not visible in all redshift bins we are interested in ($z_{\mathrm{max}} < z_{\mathrm{upper}}$) we count 1 galaxy per $V_i(M, z, \mathrm{SED})_{<}$. In this case the comoving volume has an upper limit of z_{max} instead of z_{upper} (see Equation 6.6).

To determine the errors we use the same method as Nicol (2009) which makes it easier to include the data from the Abell 901 field into the fields of Abell 226 and S11. Nicol (2009) only considered a statistical Poisson noise for the galaxy counts into the determination of the errors of $\Phi(M)dM$: $\sigma_\Phi = \sqrt{\sum_i 1/V_i^2(M, z, \mathrm{SED})}$.

6.1.3 Calculation of z_{max}

The calculation of z_{max} for each galaxy in our two fields was done by Bartelmann (priv. communication) who already calculated the z_{max} for the Abell 901 field. Since a galaxy at z_{max} would be observed in a rest-frame B magnitude calculated from a different filter than at its real z, a k-correction is applied. For simplicity the SED template # 30 is used to calculate the k-correction for each galaxy, as # 30 is the average SED type (see Figure 6.1, left panel). Of

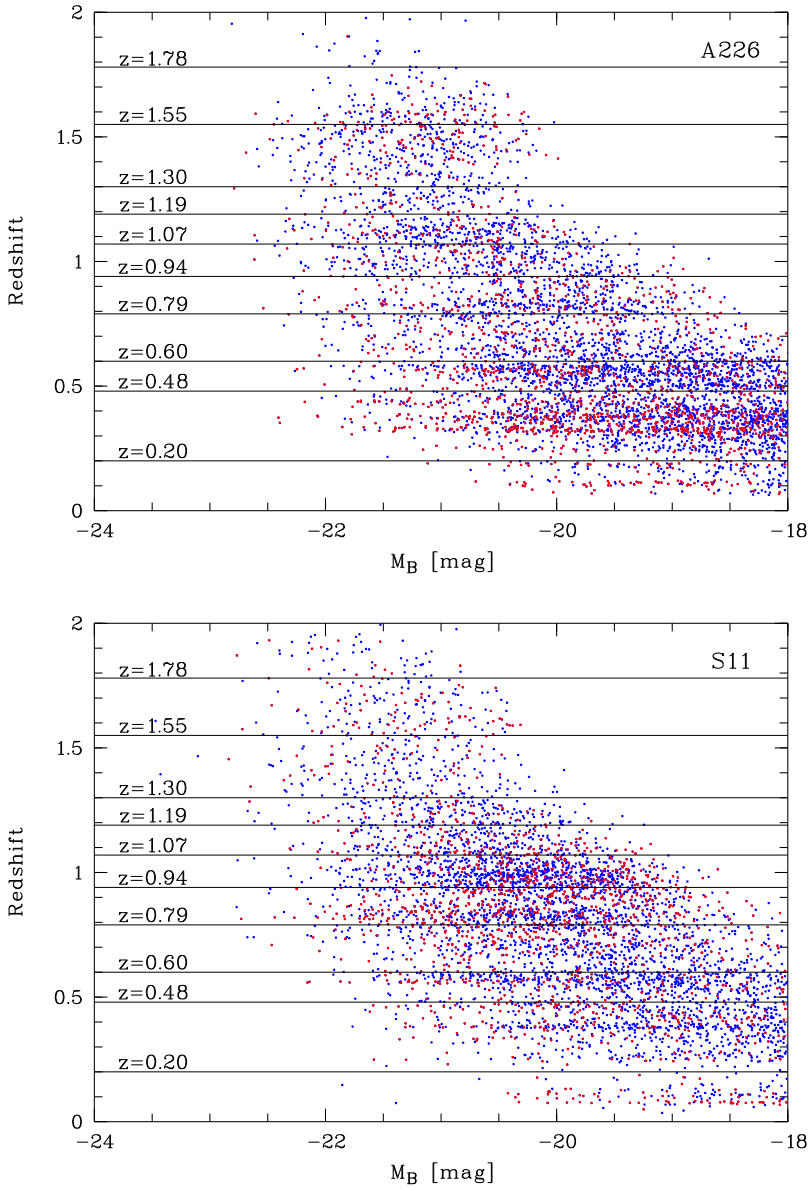

Figure 6.2: Absolute magnitude M_B versus redshift. The two separated populations of red and blue galaxies are shown in their corresponding colors. Only objects within the magnitude limits are shown. The horizontal lines give the redshift boundaries which are used to calculate the comoving volumes.

course, it would be more accurate to calculate a k-correction for each SED type individually. The program by Bartelmann starts by computing a H band k-correction for the redshift range $0 < z < 2$. This k-correction is normalized so that $K(z = 0) = 0$ (see Figure 6.1, right panel). In a second step the program calculates the rest frame color $(B - H)$ using the template SED # 30. The color is used to convert M_B into M_H. With the so calculated magnitude M_H we calculate the maximum luminosity distance $D_{L_{\max}}$. $D_{L_{\max}}$ describes at what

distance our objects will be too faint to be still within our magnitude limits. For this Equation 1.4 is used in which D_L is replaced with $D_{L_{\max}}$, m is defined as the magnitude limit of our field and $K(z)$ is given by Figure 6.1 (left panel). From the luminosity $D_{L_{\max}}$ the $z_{\max}$ is calculated using the definition of D_L in Equation 1.5.

6.2 Evolution of the Luminosity Function

In order to study the luminosity function of the galaxies in the COMBO-17+4 survey we divide the galaxies into a blue and a red populations as numerous previous studies showed that in these two populations the parameters M^* and Φ^* evolve differently (Fried et al., 2001; Wolf et al., 2003a; Bell et al., 2004b; Faber et al., 2007; Cool et al., 2012). The limiting $(U_{280} - V)$ color established in Equation 5.6 is used to separate the two populations. In addition each field was divided into 10 redshift bins, ranging from $z = 0.2$ to $z = 2.0$. The limits of the different redshift bins can be seen as horizontal lines in Figure 6.2. Due to the low number of objects at high redshift the three bins above $z > 1.3$ contain a volume 2.5 times larger than the other redshift bins – as already explained in Section 5.4.1. Because of the large numbers of galaxies at low redshifts we also divide the redshift bin of $0.2 < 0.6$ into two bins (separated at $z = 0.48$). As Nicol (2009) used the same redshift bins for the Abell 901 field we are able to compare the results between the Abell 901 field and the two other fields directly.

The evolution of the luminosity function of the two analyzed fields and the different redshift bins can be seen in the Figures 6.3 to 6.6. Luminosity functions containing the combined data from all three COMBO-17+4 fields (A226, A901 and S11) can be seen in the Figures 6.7 and 6.8.

For each redshift bin and each galaxy population we calculate an individual Schechter function to get the corresponding Φ^* and M^*. As already mentioned above we decide to fix the third free parameter α to get better values for the other two. Nicol (2009) used the values by Faber et al. (2007) who created luminosity functions up to $z = 1$ (also separately for blue and red galaxies) using data from the DEEP2 as well as from the COMBO-17 survey. When Faber et al. (2007) compared the luminosity functions from the DEEP2 data and the data acquired by COMBO-17 they found good agreement. As the data from the COMBO-17 survey they used only contained information from the Abell 901 and S11 fields (Abell 226 was not available in 2007), which are exactly the fields of the COMBO-17+4 survey, it seems reasonable to use the parameter α they found as a fixed value. In addition these value agree very well with the data acquired by the VVDS (Faber et al., 2007), and CADIS (Fried et al., 2001) which makes our results comparable to other published datasets. Specifically for this

we are using the value $\alpha = -0.05$ for red galaxies and the value $\alpha = -1.3$ for blue galaxies.

The dotted vertical lines in the Figures 6.3 to 6.8 give the magnitude limit for the fit of the Schechter function – galaxies fainter than these limits are not used to fit the function because we consider the sample to be incomplete at these magnitudes. In some cases this magnitude limit is different for the red and the blue population. In this case two vertical lines (in red and blue) are given, which show the limiting magnitudes for the corresponding populations. In the A226 field we are not able to fit a Schechter function for the blue population in the redshift bins of $1.55 < z < 1.78$ and $1.87 < z < 2.00$ due to small number counts. The same problem occurred for the red galaxy population in the redshift bin of $1.78 < z < 2.00$. Information on the galaxies per redshift, the calculated M_B^*, Φ^* (in units of 10,000 galaxies per Mpc) and the α are collected in the Tables 6.1, 6.2 (for A226 and S11) and 6.3 (for the combined COMBO-17+4 survey).

The analysis of the luminosity functions of the A901 field by Nicol (2009) showed, that the blue galaxies are dominating the bright end of the function in the redshift $1.00 < z < 2.00$, whereas at lower redshifts ($0.60 < z < 0.94$) the bright end is dominated by red galaxies. The two lowest redshift bins ($0.20 < z < 0.60$), finally, are populated by both red and blue galaxies at the bright end. For the A226 field we also find a dominant blue population at redshift $z > 1.00$. However, due to small numbers we cannot be sure for the redshifts $1.55 < z < 2.00$. At lower redshifts ($0.20 < z < 0.94$) the bright end of the galaxy population in A226 is populated by red and blue galaxies likewise. S11 also shows more and brighter galaxies in blue at higher redshifts ($0.94 < z < 2.00$). In the redshift range of $0.79 < z < 0.94$ the functions for the blue and the red population are almost identical, but at lower redshifts the blue populations gets more dominant again.

The difference in the luminosity functions in the three fields once more shows, how essential it is to observe different fields, to reduce the effects of inhomogeneities. Therefore we combine the three fields and create luminosity functions for the combined data (see Figures 6.7 and 6.8). The figures show that the blue galaxies are dominating again the bright end at redshift $0.94 < z < 2.00$. At lower redshifts ($0.20 < z < 0.94$) the bright population contains red as well as blue galaxies.

6.3 Analysis of the Characteristic Magnitude

The evolution of the characteristic magnitude M_B^* of the red and the blue galaxy population in the three fields of the COMBO-17+4 survey, as well as for the combined data, can be seen in Figure 6.9. Both the red and the blue

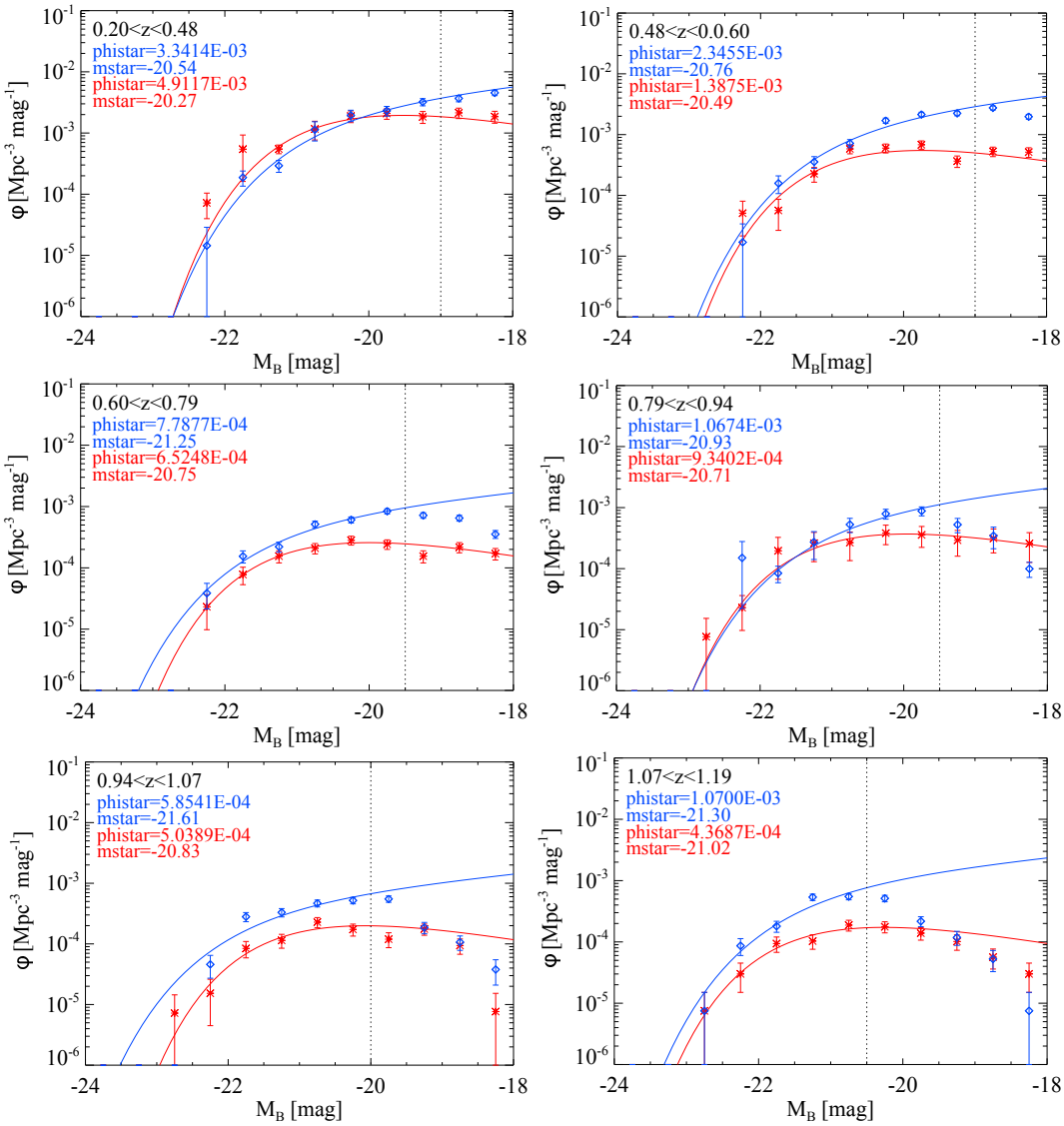

Figure 6.3: Luminosity function for different redshift bins in Abell 226. The calculated Φ^* and M^* for the blue and the red population are given. The vertical line indicates the magnitude limit which is used to calculate the luminosity function in each redshift bin.

population show a dimming since $z = 2$. However, the evolution of M_B^* in the individual fields does not show a constant slope, due to cosmic variances. From $z = 2$ to $z = 0.2$ the blue population dimmed by $\sim$1.0 mag and the red population by $\sim$1.7 mag.

However, we have to be careful in interpreting the value for our highest redshift bin, as the number of galaxies therein is still low. In addition the number of faint galaxies is incomplete for $z \gtrsim 1.3$ which is affecting the results of M_B^* and Φ^*. Now we can compare these numbers with the few available

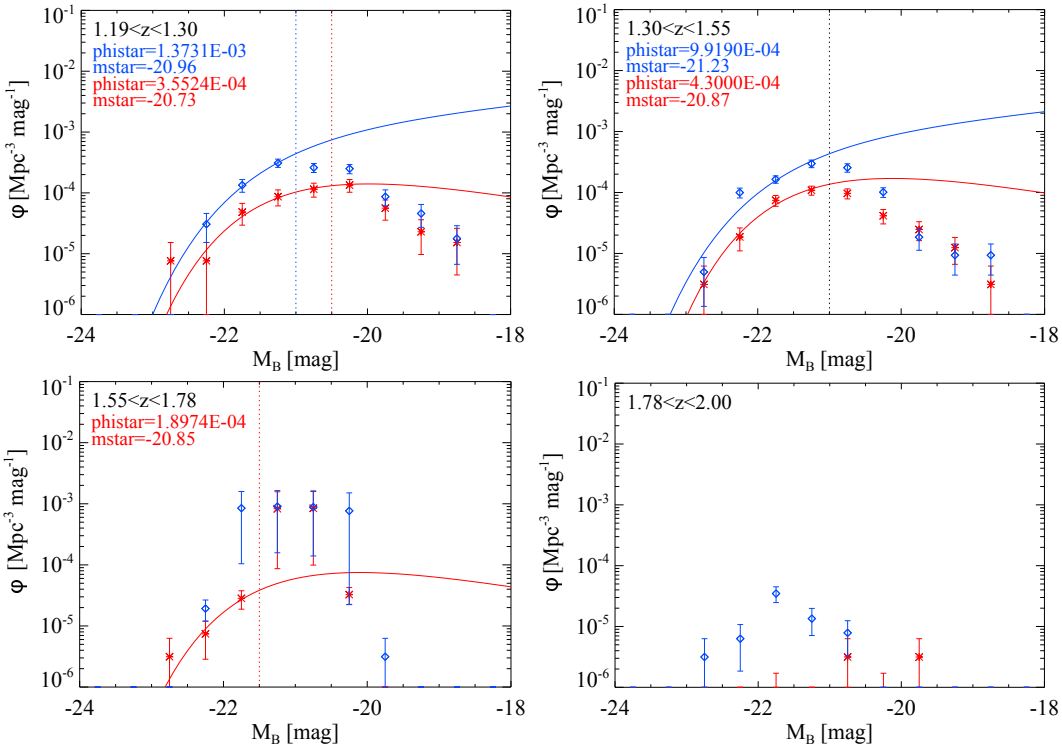

Figure 6.4: Luminosity function for different redshift bins in Abell 226. The calculated Φ^* and M^* for the blue and the red population are given. The vertical line indicates the magnitude limit which is used to calculate the luminosity function in each redshift bin. In the redshift bin $1.19 < z < 1.30$ we use different magnitude cuts for the red and the blue galaxy population. It is not possible to fit a function for the blue population in the $1.55 < z < 1.78$ bin. Due to small numbers no functions are fitted in the redshift bin $1.78 < z < 2.00$.

numbers of separated luminosity functions based on M_B in the literature:

Bell et al. (2004b) created a luminosity function in the redshift range $0.2 < z < 1.1$ for the red galaxy population of the COMBO-17 survey. To separate the red galaxies from the blue ones they also used an evolving separating line in the $(U - V)$ rest-frame color. To calculate the luminosity function they used a fixed $\alpha = 0.60$. They derived a M_B^* which dimmed in the analyzed redshift range by $\sim$0.8 mag. In the same redshift range the calculated M_B^* in the COMBO-17+4 survey dimmed only by $\sim$0.58 mag. The reason for this discrepancy can easily be explained by the different (fixed) slopes α which are used in this thesis and in the work by Bell et al. (2004b).

Our resulting M_B^*s are also in good agreement with the results of Faber et al. (2007), who created luminosity functions for redshift $0.3 < z < 1.3$ using the DEEP2 survey. Their results indicate a dimming of 1.50 mag for their blue galaxy population and 0.51 mag for their red population. Within this red-

shift range we measure a dimming of $\sim$1.02 mag for the blue population and of $\sim$0.76 mag for the red galaxy population. These results show that we are able to create luminosity functions based on a photometric survey which are comparable to the results based on a spectroscopic survey.

Faber et al. (2007) also recalculated the luminosity function for the COMBO-17 survey: They received an even stronger dimming compared to Bell et al. (2004b) for the red population. Their functions indicate, that the red galaxies got fainter by 0.95 mag from $z = 1.1$ to $z = 0.2$. The discrepancy between both analysis can again be explained by different slopes α used. Taking into account that we are using a H band selected catalog of objects for the COMBO-17+4 survey and a R band selected catalog is used for the COMBO-17 survey, the results also agree with ours.

Our resulting characteristic magnitudes, which are supported by the above mentioned works, indicate that blue as well as red galaxies were brighter at higher redshifts and since then dimmed continuously (see Figure 6.10, bottom panel). Because brightness in blue wavelengths is mainly caused by young stars our results lead to the conclusion that star formation has reduced drastically from $z = 2.0$ to $z = 0.2$. Especially the red galaxies showed a higher star formation rate in earlier times than today.

6.4 Analysis of the Normalization Factor

Due to large uncertainties due to cosmic variance, Nicol (2009) was not able to analyze the evolution of Φ^* for her luminosity functions in detail. With the complete dataset of the COMBO-17+4 survey available we hope to minimize the effects of cosmic variance and make an analysis of Φ^* possible.

The evolution of the normalization factor Φ^* of the red and the blue galaxy population in the three fields of the COMBO-17+4 survey, as well as for the combined data, can be seen in Figure 6.10. Φ^* is given in 1000 galaxies per Mpc^3. The behavior of Φ^* in the three different fields is very different in blue as well as in red. The large number of galaxies in both colors at low redshifts in the A226 field, caused by the large amount of galaxies in this redshift bin (see also Figure 4.1) is remarkable. The second remarkable feature is the rise of of Φ^* at $z = 1.0$ in the fields of A901 and S11.

The evolution of Φ^* of the combined COMBO-17+4 data shows a general trend for the blue and the red population towards lower numbers. From redshift $z \sim 1$ to $z = 0.2$ the normalization factor of the red galaxies is enhanced by a factor of 3.8 and of the blue galaxies by a factor of 2.3. These numbers are in good agreement with the values available in the literature: Bell et al. (2004b) measured a reduction by a factor of 4.43 for red galaxies in COMBO-17 and

Faber et al. (2007) calculated for galaxies in the DEEP2 survey a factor of 2.5 for the blue and of 2.4 for the red population.

From $z = 2$ to $z = 0.2$ we measure an increase in normalization factor by a factor of 7.9 for the blue galaxies and a factor of 53.3 for red galaxies. However, the value for red galaxies is contaminated by the large number of galaxies at $z \sim 0.2$ in the A226 field and also by the almost complete absence of red galaxies at $z > 1.75$ in the same field. Still we see a general trend to higher Φ^* at lower redshifts, with the red populations rising by a factor of 53 and the blue population by a factor of 7.9.

6.5 Analysis of the Number Density

To analyze the evolution of the number density ρ for red and blue galaxies we have to take into account that the three highest redshift bins do not have the same comoving volume as the lower redshift bins and the fact that our completeness limit changes at higher redshift. Therefore we analyze the number density of our galaxies again, this time within the completeness limit and corrected for the larger comoving volume at larger redshift. For the redshift $0.20 < z < 1.07$ we use a completeness limit of $M_B < -20$ mag, whereas we use a limit of $M_B < -21.0$ for the comparison of the galaxy populations at $z = 0.2$ and $z = 2.0$ – we have to take into account that our data is incomplete in the highest redshift bin for the second sample. The evolution for both samples can be seen in Figure 6.11. The numbers for the sample with a limiting magnitude of $M_B < -21.5$ are listed in the Table 6.3.

For the first sample, covering the redshift range from $z = 1$ to $z = 0.2$, we measured an increase in the number of red galaxies by a factor of 1.75. Within the same redshift range the number of blue galaxies decreased by a factor of 1.6. The second sample, which includes galaxies with $M_B < 21.0$ mag from $z = 2$ to $z = 0.2$, shows a constant increase for the red population since $z = 2$. In our lowest redshift bin we see double the amount of galaxies per Mpc compared to the highest redshift bin. The peak visible at $z \sim 0.8$ can be explained with the redshift focusing which was identified in Section 4.3.3. The rise in the number of red galaxies at lower redshifts is expected: There should be more evolved red galaxies in an older universe than in a younger one. The results of the evolution in number density of the blue galaxy population is more difficult to understand. We expect to find a lower number of blue galaxies at lower redshifts, because of the same arguments as for the red population. We find indeed a decrease by a factor of three from $z = 1.3$ to $z = 0.2$ but our results indicate lower numbers in the number density at $z > 1.3$. We can interpret this result in two ways: Either the decrease at $z > 1.3$ is caused by cosmological variance or we face an incompleteness of the blue population

Table 6.1: Fitted Schechter parameters for both galaxy populations in the A226 field. The characteristic magnitudes M_B^*, the number density Φ^* and the fixed slope α, adapted from Faber et al. (2007), are given.

Redshift $[z]$	Galaxies [nr]	M_B^* [mag]	Φ^* $[\times 10^{-4}$ Mpc$^{-3}]$	α_{fixed}
A226 RED				
0.20-0.48	1225	-20.27 $\pm$ 0.11	49.12 $\pm$ 6.49	-0.5
0.48-0.60	258	-20.49 $\pm$ 0.11	13.87 $\pm$ 1.34	-0.5
0.60-0.79	215	-20.75 $\pm$ 0.13	6.52 $\pm$ 0.71	-0.5
0.79-0.94	197	-20.71 $\pm$ 0.15	9.34 $\pm$ 2.11	-0.5
0.94-1.07	139	-20.83 $\pm$ 0.15	5.04 $\pm$ 0.79	-0.5
1.07-1.19	129	-21.02 $\pm$ 0.19	4.37 $\pm$ 0.91	-0.5
1.19-1.30	69	-20.73 $\pm$ 0.22	3.55 $\pm$ 1.01	-0.5
1.30-1.55	130	-20.87 $\pm$ 0.15	4.30 $\pm$ 1.04	-0.5
1.55-1.78	76	-20.85 $\pm$ 0.43	1.90 $\pm$ 1.78	-0.5
1.78-2.00	4			
A226 BLUE				
0.20-0.48	1858	-20.54 $\pm$ 0.11	33.41 $\pm$ 4.91	-1.3
0.48-0.60	781	-20.76 $\pm$ 0.10	23.46 $\pm$ 2.24	-1.3
0.60-0.79	565	-21.25 $\pm$ 0.14	7.79 $\pm$ 0.97	-1.3
0.79-0.94	394	-20.93 $\pm$ 0.18	10.67 $\pm$ 2.15	-1.3
0.94-1.07	343	-21.61 $\pm$ 0.18	5.85 $\pm$ 0.95	-1.3
1.07-1.19	318	-21.30 $\pm$ 0.13	10.70 $\pm$ 1.85	-1.3
1.19-1.30	164	-20.96 $\pm$ 0.24	13.73 $\pm$ 6.18	-1.3
1.30-1.55	315	-21.23 $\pm$ 0.12	9.92 $\pm$ 2.27	-1.3
1.55-1.78	138			
1.78-2.00	26			

in the three highest redshift bins. As we only know of an incompleteness in the redshift bin $1.78 < z < .200$, the reason has to be cosmological variance - besides the fact, that we used three different fields of view.

Table 6.2: Fitted Schechter parameters for both galaxy populations in the S11 field. The characteristic magnitudes M_B^*, the number density Φ^* and the fixed slope α, adapted from Faber et al. (2007), are given.

Redshift $[z]$	Galaxies [nr]	M_B^* [mag]	Φ^* $[\times 10^{-4}\ \mathrm{Mpc}^{-3}]$	α_{fixed}
S11 RED				
0.20-0.48	442	-20.35 $\pm$ 0.12	17.28 $\pm$ 1.69	-0.5
0.48-0.60	160	-20.44 $\pm$ 0.13	14.51 $\pm$ 1.61	-0.5
0.60-0.79	245	-20.60 $\pm$ 0.11	11.23 $\pm$ 1.13	-0.5
0.79-0.94	411	-20.77 $\pm$ 0.10	20.61 $\pm$ 2.27	-0.5
0.94-1.07	266	-20.24 $\pm$ 0.13	16.74 $\pm$ 2.71	-0.5
1.07-1.19	169	-20.66 $\pm$ 0.17	9.11 $\pm$ 2.04	-0.5
1.19-1.30	71	-20.85 $\pm$ 0.24	4.84 $\pm$ 1.32	-0.5
1.30-1.55	91	-21.25 $\pm$ 0.23	2.16 $\pm$ 0.61	-0.5
1.55-1.78	91	-20.81 $\pm$ 0.31	4.88 $\pm$ 3.42	-0.5
1.78-2.00	29	-21.34 $\pm$ 0.48	0.96 $\pm$ 0.68	-0.5
S11 BLUE				
0.20-0.48	1196	-20.35 $\pm$ 0.12	28.11 $\pm$ 3.44	-1.3
0.48-0.60	529	-20.97 $\pm$ 0.14	20.12 $\pm$ 2.32	-1.3
0.60-0.79	563	-21.16 $\pm$ 0.12	11.66 $\pm$ 1.37	-1.3
0.79-0.94	559	-21.23 $\pm$ 0.12	14.49 $\pm$ 1.88	-1.3
0.94-1.07	649	-21.00 $\pm$ 0.13	27.83 $\pm$ 3.18	-1.3
1.07-1.19	247	-21.25 $\pm$ 0.20	11.21 $\pm$ 2.78	-1.3
1.19-1.30	178	-21.33 $\pm$ 0.18	9.21 $\pm$ 2.11	-1.3
1.30-1.55	210	-21.93 $\pm$ 0.23	3.84 $\pm$ 0.97	-1.3
1.55-1.78	128	-21.42 $\pm$ 0.23	4.07 $\pm$ 1.41	-1.3
1.78-2.00	60	-21.38 $\pm$ 0.32	3.77 $\pm$ 2.37	-1.3

Table 6.3: Fitted Schechter parameters for both galaxy populations in the combined data of the COMBO-17+4 survey. The characteristic magnitudes M_B^*, the number density Φ^* and the fixed slope α, adapted from Faber et al. (2007), are given. The last column gives the number density ρ in units of 10,000 galaxies per Mpc^{-3} for galaxies brighter $M_B < -21.0$.

Redshift $[z]$	Galaxies [nr]	M_B^* [mag]	Φ^* [$\times 10^{-4}$ Mpc^{-3}]	α_{fixed}	ρ [Gal^4 Mpc^{-3}]
C17p4 RED					
0.20-0.48	2111	-20.33 $\pm$ 0.07	31.46 $\pm$ 2.59	-0.5	1.01
0.48-0.60	607	-20.64 $\pm$ 0.07	14.60 $\pm$ 0.83	-0.5	0.86
0.60-0.79	759	-20.93 $\pm$ 0.07	9.16 $\pm$ 0.48	-0.5	0.83
0.79-0.94	1037	-20.87 $\pm$ 0.06	15.82 $\pm$ 0.97	-0.5	1.21
0.94-1.07	714	-20.66 $\pm$ 0.07	11.93 $\pm$ 0.84	-0.5	0.71
1.07-1.19	556	-20.91 $\pm$ 0.08	8.18 $\pm$ 0.78	-0.5	0.80
1.19-1.30	315	-21.06 $\pm$ 0.10	5.98 $\pm$ 0.64	-0.5	0.69
1.30-1.55	403	-21.38 $\pm$ 0.08	3.26 $\pm$ 0.32	-0.5	0.49
1.55-1.78	324	-21.30 $\pm$ 0.19	2.98 $\pm$ 1.28	-0.5	0.49
1.78-2.00	73	-21.98 $\pm$ 0.20	0.59 $\pm$ 0.13	-0.5	0.13
C17p4 BLUE					
0.20-0.48	4472	-20.67 $\pm$ 0.08	26.11 $\pm$ 2.07	-1.3	0.75
0.48-0.60	1811	-20.85 $\pm$ 0.06	21.93 $\pm$ 1.23	-1.3	1.14
0.60-0.79	1812	-21.23 $\pm$ 0.07	10.79 $\pm$ 0.70	-1.3	1.14
0.79-0.94	1767	-21.34 $\pm$ 0.11	13.39 $\pm$ 1.44	-1.3	1.37
0.94-1.07	1895	-21.30 $\pm$ 0.06	18.77 $\pm$ 1.16	-1.3	2.09
1.07-1.19	1068	-21.55 $\pm$ 0.08	11.51 $\pm$ 1.08	-1.3	1.97
1.19-1.30	862	-21.69 $\pm$ 0.08	10.70 $\pm$ 1.01	-1.3	2.23
1.30-1.55	929	-21.73 $\pm$ 0.08	6.64 $\pm$ 0.75	-1.3	1.29
1.55-1.78	424	-21.69 $\pm$ 0.24	7.12 $\pm$ 4.96	-1.3	0.88
1.78-2.00	242	-21.71 $\pm$ 0.12	3.29 $\pm$ 0.70	-1.3	0.50

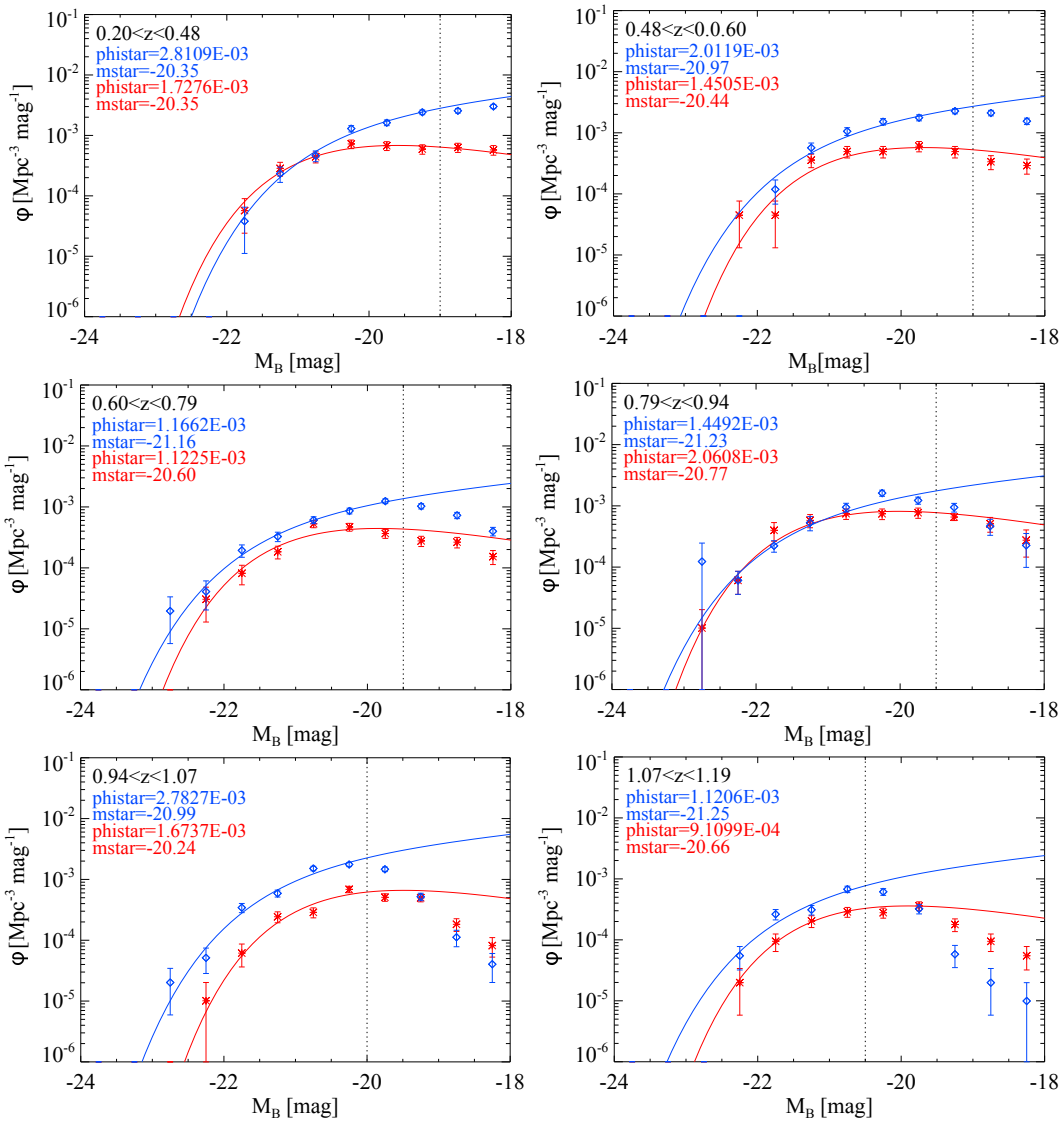

Figure 6.5: Luminosity function for different redshift bins in S11. The calculated Φ^* and M^* for the blue and the red population are given. The vertical line indicates the magnitude limit which is used to calculate the luminosity function in each redshift bin.

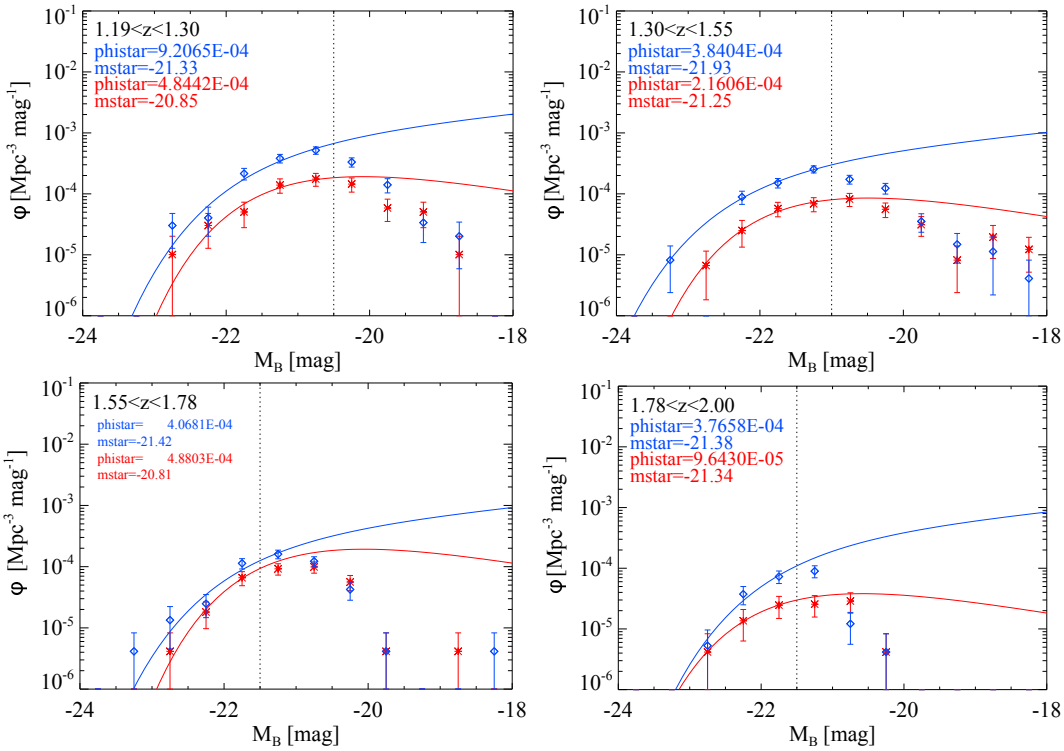

Figure 6.6: Luminosity function for different redshift bins in S11. The calculated Φ^* and M^* for the blue and the red population are given. The vertical line indicates the magnitude limit which is used to calculate the luminosity function in each redshift bin.

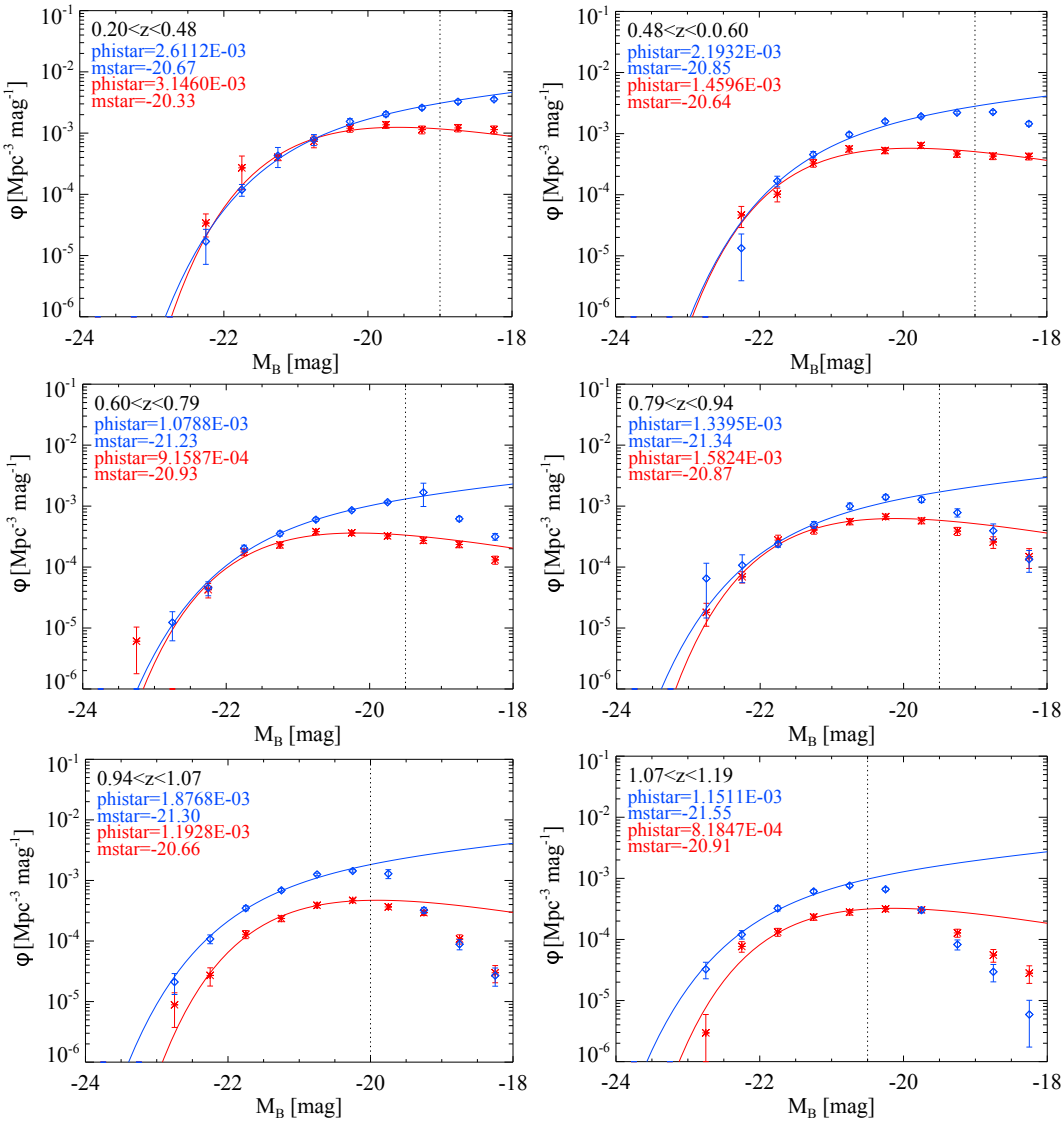

Figure 6.7: Luminosity function for different redshift bins for the combined data from the COMBO-17+4 survey. The calculated Φ^* and M^* for the blue and the red population are given. The horizontal line indicates the magnitude limit which is used to calculate the luminosity function in each redshift bin.

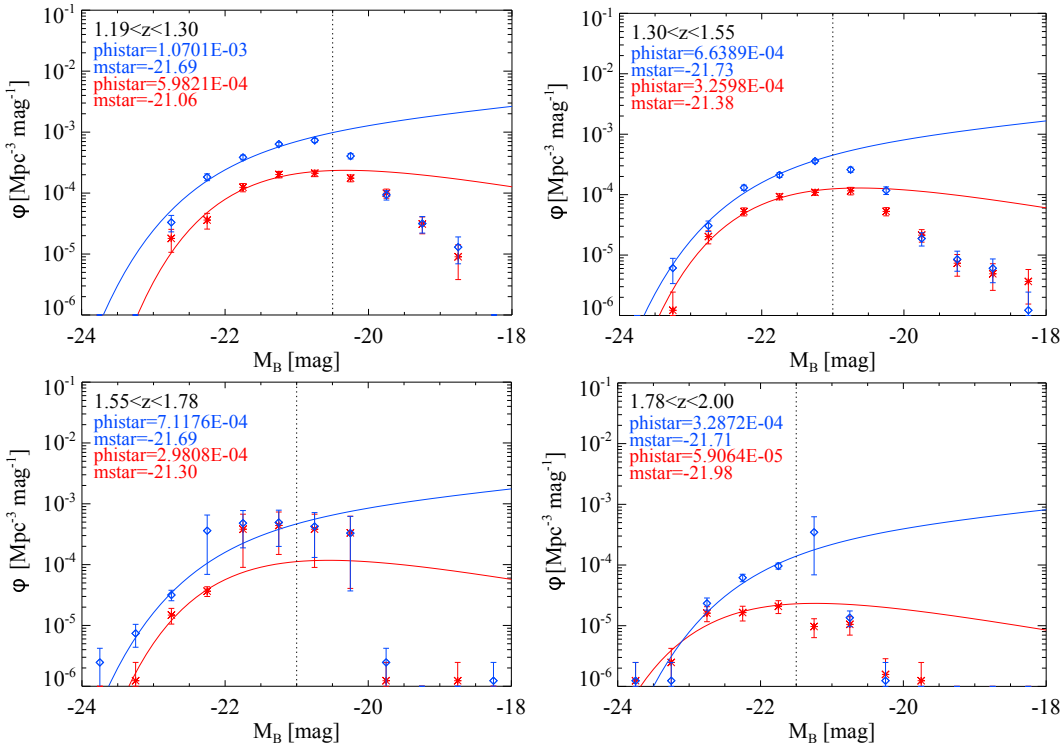

Figure 6.8: Luminosity function for different redshift bins for the combined data from the COMBO-17+4 survey. The calculated Φ^* and M^* for the blue and the red population are given. The horizontal line indicates the magnitude limit which is used to calculate the luminosity function in each redshift bin.

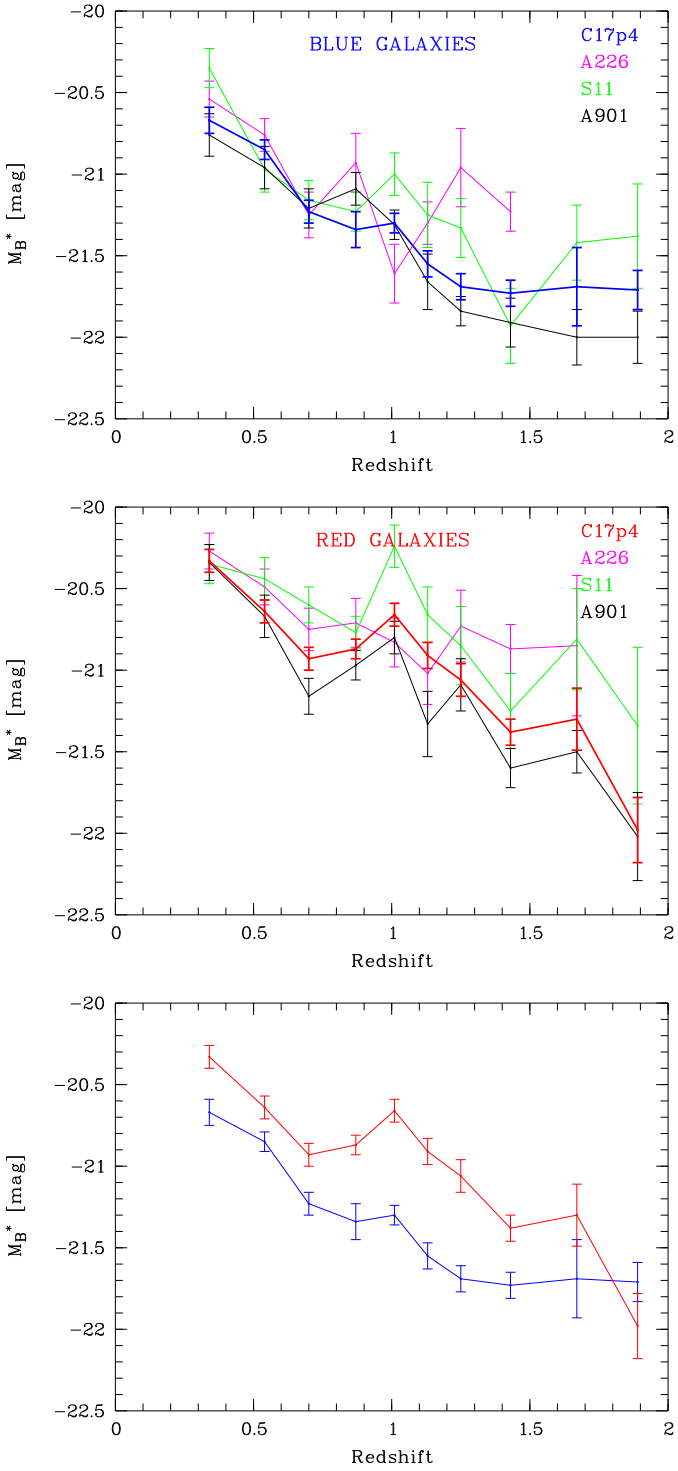

Figure 6.9: Evolution of M_B^* in redshift. The top panel shows the evolution of M_B^* for the blue and the middle panel for the red galaxy population in the three different field as well as in the combined COMBO-17+4 survey. The bottom panel compares the evolution of M_B^* in the red and blue galaxy population of the total COMBO-17+4 survey.

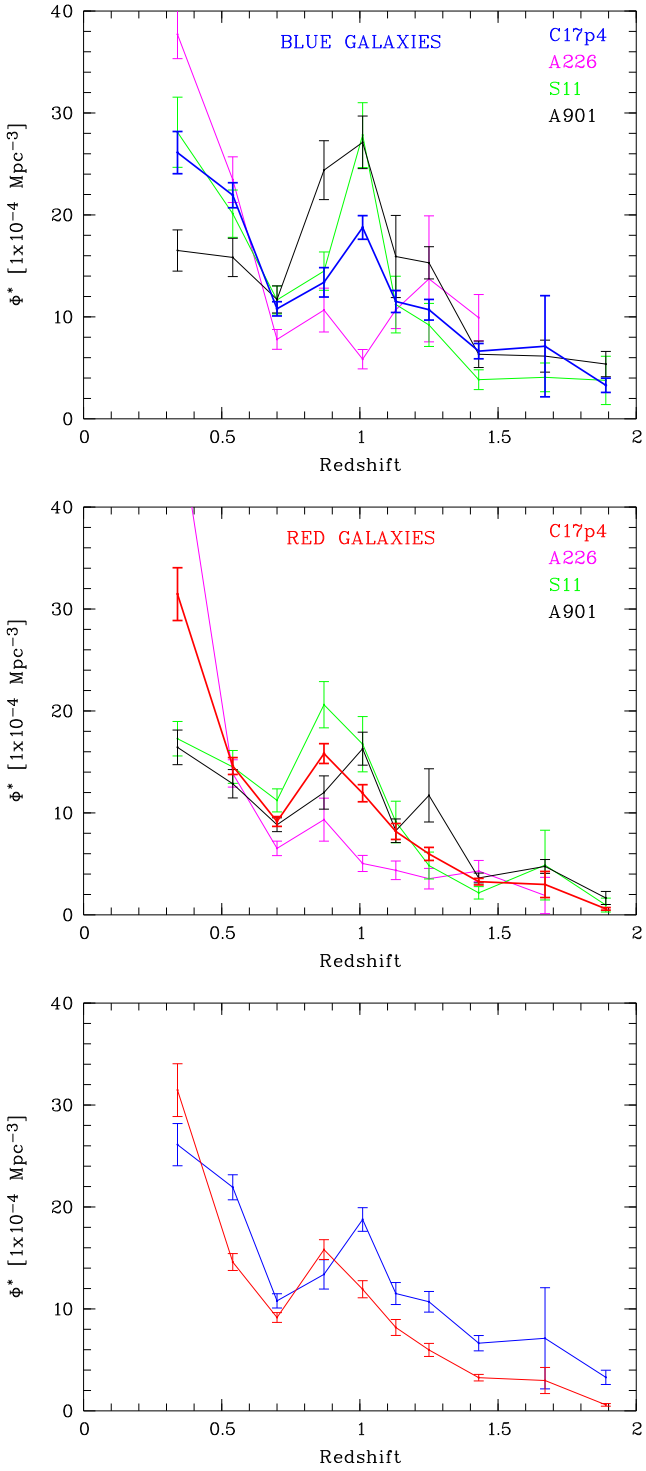

Figure 6.10: Evolution of Φ^* in redshift. The top panel shows the evolution of Φ^* for the blue galaxy population and the middle panel the evolution for the red galaxy population in the three different field as well as in the combined COMBO-17+4 survey. The bottom panel compares the evolution of Φ^* in the red and blue galaxy population of the total COMBO-17+4 survey.

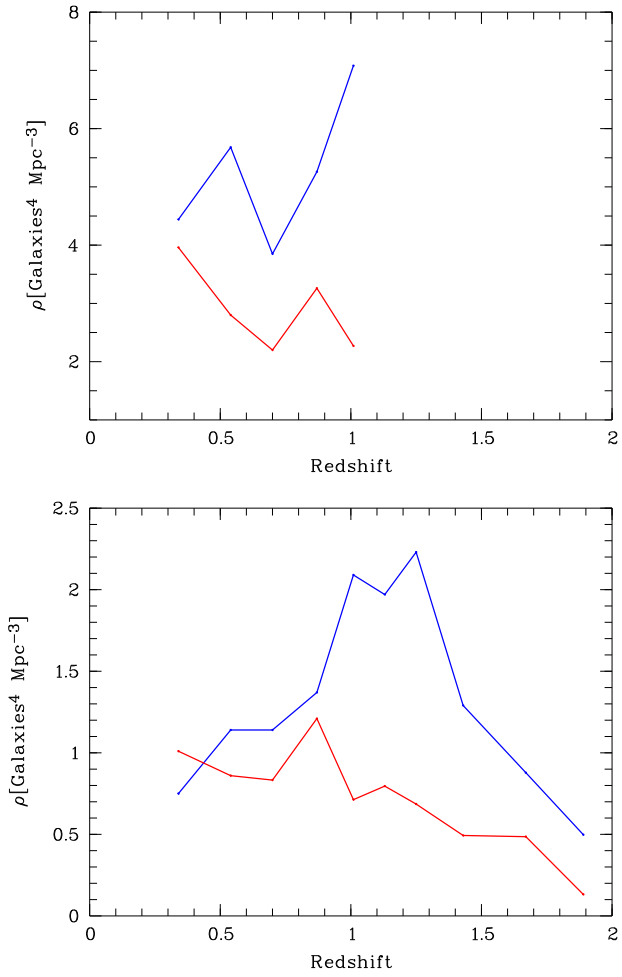

Figure 6.11: The evolution of the number density ρ in redshift for the combined COMBO-17+4 survey. The top panel only includes galaxies at $z < 1.07$ and with $M_B < -20$ The bottom panel shows ρ at $z < 2.0$ with a minimum magnitude of $M_B < -21.0$.

Chapter 7

Mass Function

After the successful determination and analysis of the luminosity function we also create stellar mass functions and study their evolution in the redshift range of $0.2 < z < 2.0$. The mass function, like the luminosity function, allows us to study the evolution and build up of the red sequence, as evolved galaxies with an old stellar population tend to be more massive than their star forming counterparts. In addition we are able to identify high massive, red galaxies at $z > 1$ – objects which should not exist in the classical bottom-up scenario but which are detected in several surveys. As Nicol et al. (2011) identified several high massive objects in the Abell 901 field, it is highly likely that we also find some of these rare objects in the fields of Abell 226 and the S11.

7.1 Calculation of Masses

We calculate the stellar masses of the galaxies using their stellar mass-to-light ratios (M_*/L). We get these ratio from the galaxy templates in the population synthesis package PEGASE (see section 4.1.1). To calculate the mass we first calculate the rest-frame magnitude M_V to get the luminosity L_V:

$$\frac{L_V}{L_{V\odot}} = 10^{-0.4(M_V - M_{V\odot})} \tag{7.1}$$

In the second step we calculate the mass, based on the luminosity of the galaxy in the V band. Therefore we multiply the mass-to-light ratio in solar units ($M_\odot$ and $L_\odot$) by the luminosity L_V:

$$M_{*V} = \left(\frac{M_*}{L}\right)_V \times L_V \tag{7.2}$$

The V band is used for the mass calculation as it leads to the best results. Therefore it was also already used for the calculation of masses in the Abell 901 field by Nicol (2009). The use of the V band makes the results from the COMBO-17+4 survey also comparable to many studies available in the literature, where L_V is also often used for the mass calculation. However, most studies use only the direct measured L_V to determine the masses of the galaxies, whereas for the COMBO-17+4 survey the information on the history of the star formation in the galaxy is used. This information is available because of the use of the PEGASE templates. The resulting mass-to-light ratios versus the color $(U_{280} - V)$ can be seen in Figure 7.1. We see that red galaxies have a higher mass-to-light ratio as blue ones.

7.2 Color Mass Diagrams

After the calculation of the masses of the galaxies we create color to stellar mass diagrams (CM_*Ds). For this, the same galaxies with the same redshift bins are used as for the luminosity functions. This also means that we are analyzing the same volumes as for the luminosity function. We again separate our galaxies in a red and a blue population based on the separating color, which was calculated in Equation 5.4.

Within the CM_*Ds we use $(U_{280} - V)$ as color, which we plot versus their calculated stellar masses. Figures 7.2 to 7.5 show the galaxies in the 10 redshift bins for the A226 field and the S11 field. The blue galaxy population is shown in blue and the red galaxy population in red. We can see immediately that galaxies with redder colors tend to have higher masses. We can also see the general trend that at a specific mass galaxies tend to be bluer at higher redshifts than at lower redshifts. This fits our picture of an evolving and aging universe.

We see that red galaxies dominate mass rich population at $z < 1$. At higher redshift we detect an increasing number of blue galaxies with high masses. We also see the almost non existing population of red galaxies in the A226 field at $1.78 < z < 2.00$ which was already discussed in Section 5.4.1. The evolution from a large number of blue galaxies with high masses at $z \sim 2$ to a large number of red galaxies with high masses at low redshifts is in agreement with the common cosmological picture and therefore was expected.

In particular we use the CM_*Ds to identify the completeness in mass in each redshift bin – the limit is indicated as black line in each redshift bin. We use these empirical determined lines to get the limiting masses for the mass functions (see Section 7.3). We also use the CM_*Ds to check for outliers (objects with very red colors and / or very low or very high masses). We check the fitted SED template of these objects and exclude objects with wrong fitted templates from the sample. Otherwise these objects are contaminating our mass

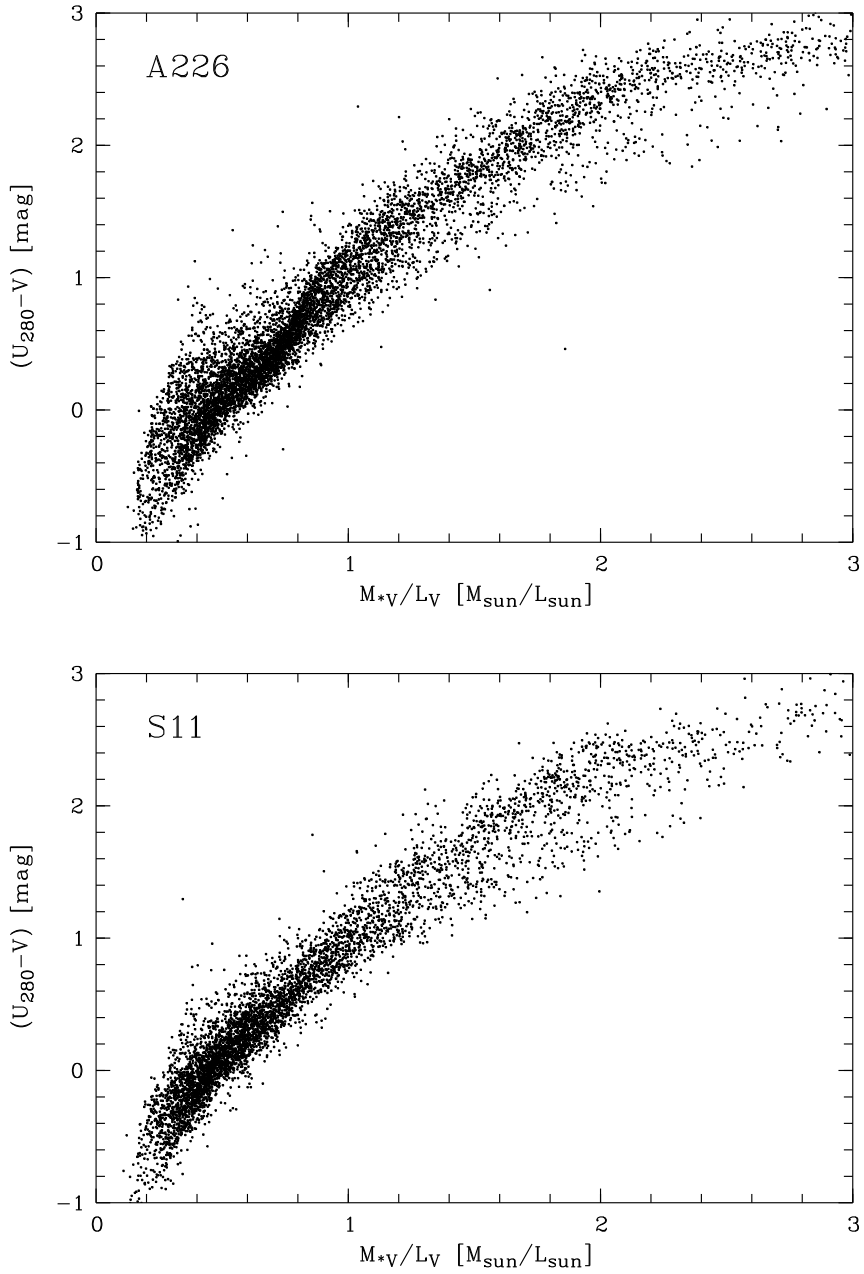

Figure 7.1: $(U_{280} - V)$ color as a function of of the stellar mass-to-light ratio, which is derived from the galaxy SED templates. Only objects with a redshift lower than $z_{\max}$ (calculated for the luminosity functions, see Section 6.1.3) and $\sigma(U_{280} - V) < 0.3$ mag are shown. It can clearly be seen that galaxies with redder colors have a higher mass-to-light ratio as bluer galaxies.

functions.

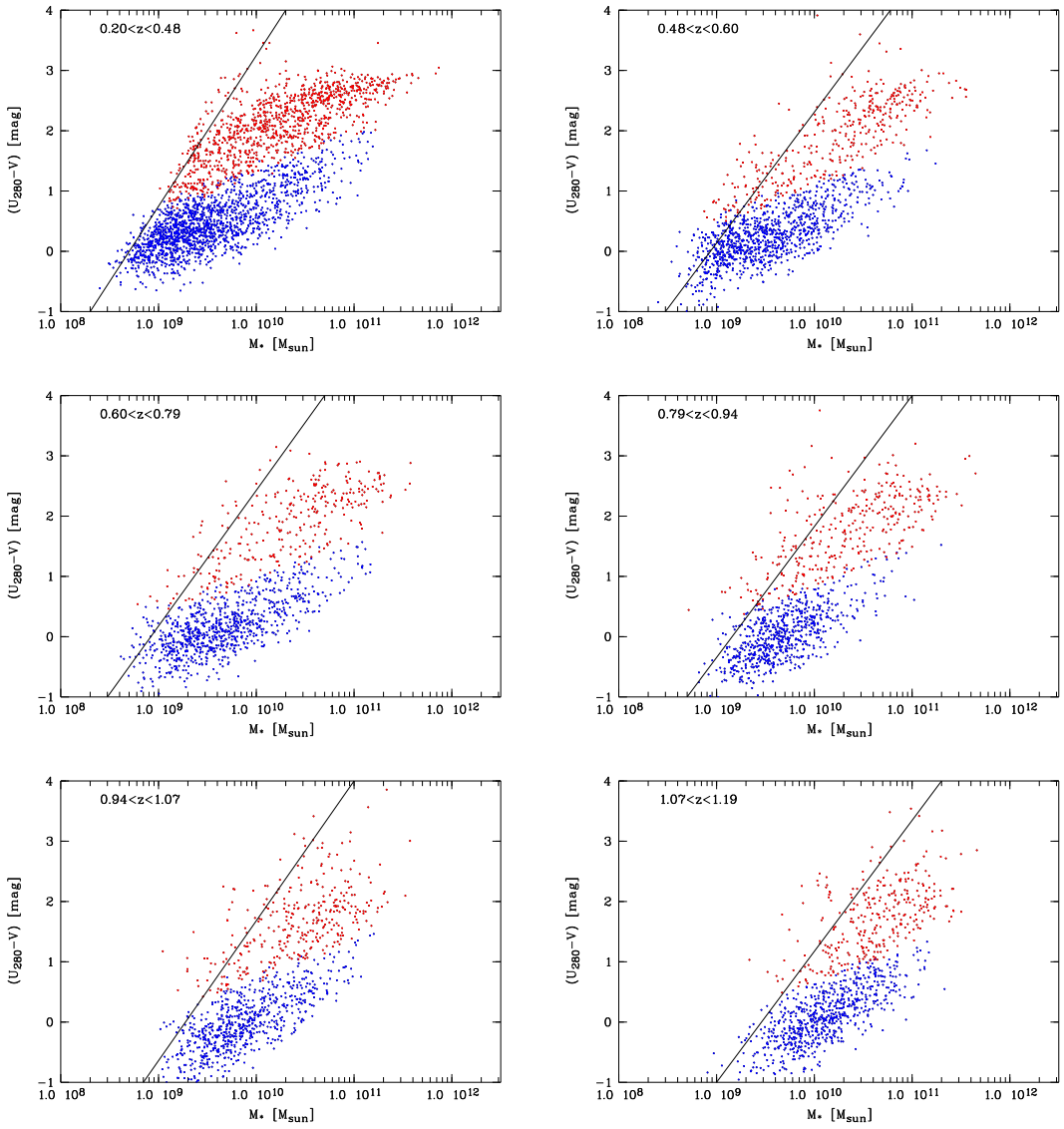

Figure 7.2: Color-mass diagrams for different redshift bins in Abell 226. Galaxies populating the red sequence and the blue cloud are colored in their corresponding colors.

7.3 Massfunction

To analyze the evolution in mass for our galaxy populations in detail we create mass functions. The mass functions for the COMBO-17+4 survey are, very much like the luminosity functions, calculated with a Schechter function

$$\Phi(M_*) = \left(\frac{\Phi^+}{M^+}\right)\left(\frac{M_*}{M^+}\right)^{\beta} \exp\frac{-M_*}{M^+}. \tag{7.3}$$

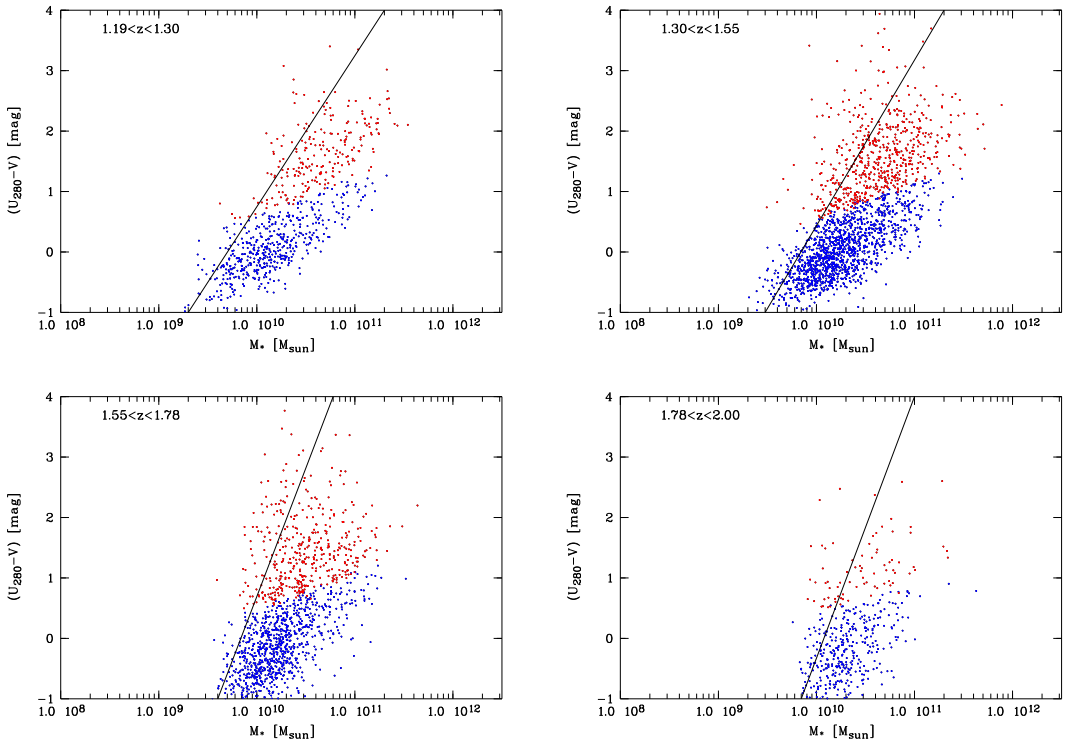

Figure 7.3: Color-mass diagrams for different redshift bins in Abell 226. Galaxies populating the red sequence and the blue cloud are colored in their corresponding colors.

Where Φ^+ is defined as the normalization of the distribution, M^+ is the characteristic mass, $\Phi(M_*)$ is the number density of galaxies in the mass range $[M_*, M_* + dM_*]$ and β describes the slope at the low-mass end of the mass function.

Like for the luminosity functions we use the non parametric estimator $1/V_{\max}$ by Schmidt (1968) for the analysis of the data. The differential mass function by the $1/V_{\max}$ method is:

$$\Phi(M_*)dM_* = \sum_i \frac{1}{V_i} dM_*. \tag{7.4}$$

7.4 Evolution of the Mass Function

We study the evolution of the masses for the red and the blue separately in 10 different redshift bins. However, in contrast to the luminosity function we do not study the evolution of the galaxies in the three fields separately because Nicol (2009) showed in the analysis of the A901 field, that one field does not contain enough galaxies (especially at high redshifts) and is too much influ-

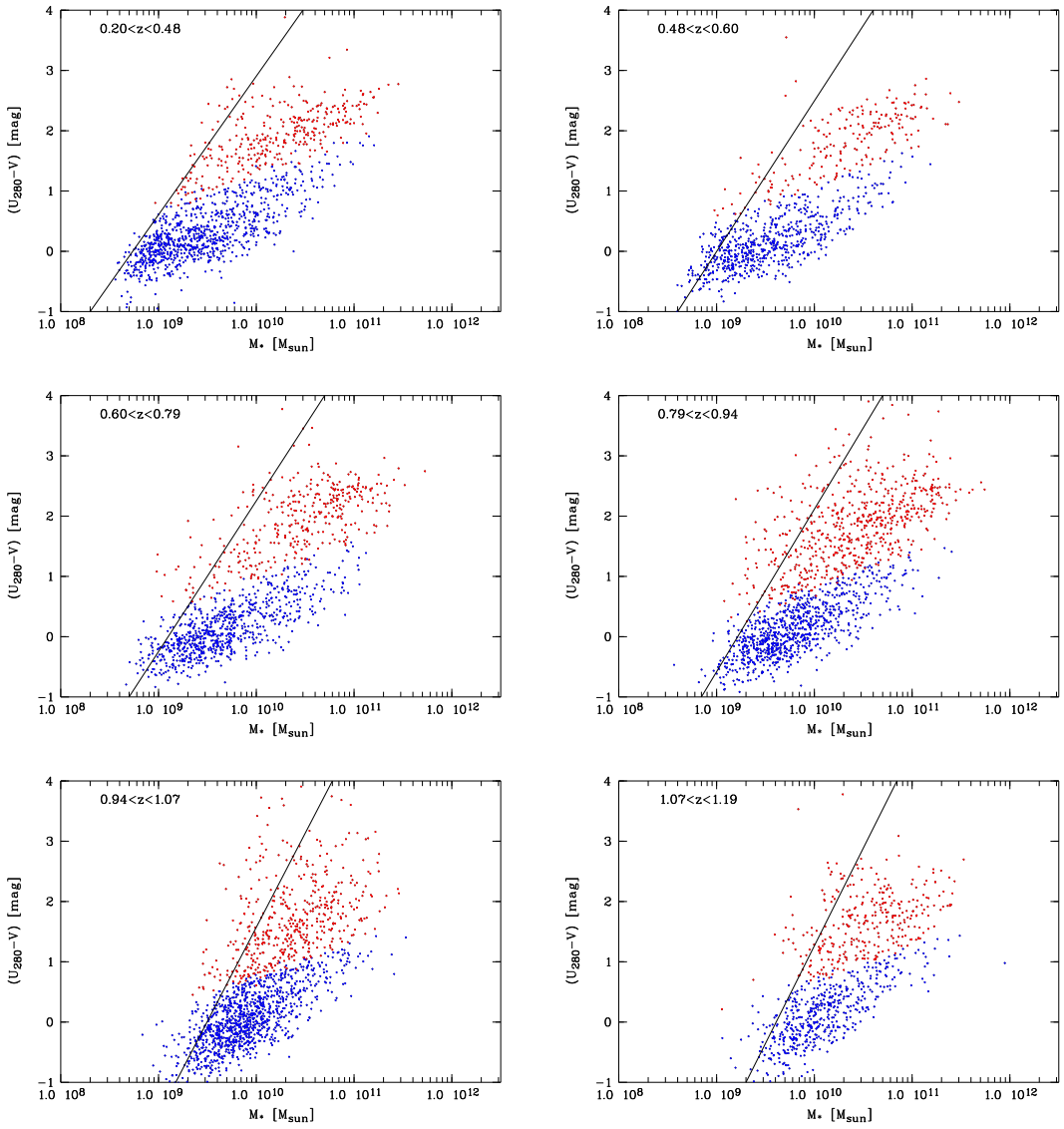

Figure 7.4: Color-mass diagrams for different redshift bins in S11. Galaxies populating the red sequence and the blue cloud are colored in their corresponding colors.

enced by large scale cosmological structures (i.e. galaxy clusters) to calculate a useful mass function. Like for the luminosity functions we use fixed values for β for both populations ($\beta_{\mathrm{red}} = 0.3$, $\beta_{\mathrm{blue}} = -0.45$). The values are taken from Borch et al. (2006) who created and analyzed mass functions for three fields (A901, S11 and CDFS[1]) of the COMBO-17 survey up to $z = 1$. The resulting functions for the combined COMBO-17+4 survey can be seen in the Figures 7.6 and 7.7. Vertical lines in the figures indicate the completeness limits which are used to calculate the mass functions. The limits are based on the results seen in the CM$_*$Ds. Table 7.1 lists the results for M^+ and Φ^+, as well as the

[1]Chandra Deep Field South

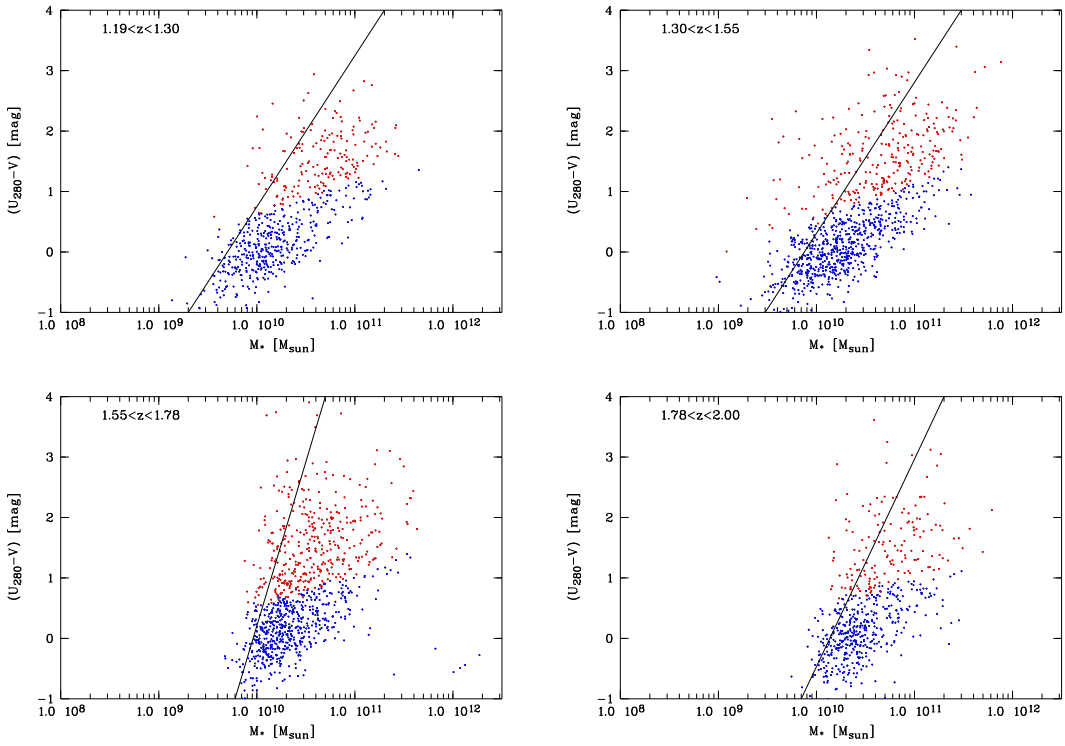

Figure 7.5: Color-mass diagrams for different redshift bins in S11. Galaxies populating the red sequence and the blue cloud are colored in their corresponding colors.

corresponding errors, for both populations in all 10 redshift bins.

We see that the red galaxies dominate the mass-rich end of the mass functions. We also see that at the low mass end that blue galaxies are more abundant than the red ones – this result is predetermined by the fixed values of β. In addition our results indicate the same amount of red and blue galaxies at a mass of $\sim 3 \times 10^{10} M_{\odot}$ at $z < 1$. Our results are supported by the results of Borch et al. (2006).

7.4.1 Analysis of the Characteristic Mass

The evolution of the characteristic mass M^{+} for the red and the blue galaxy population in the COMBO-17+4 survey can be seen in Figure 7.8 (top panel). The figure shows that the characteristic masses for red galaxies stay constant from $z = 0.2$ to $z \sim 1.55$. Just our one data point for the characteristic mass in the redshift bin of $1.78 < z < 2.00$ is increased by a factor of $\sim$2.5 compared to lower redshifts. However, we only use three data points in this redshift bin to fit the Schechter function, therefore we have to treat this result carefully. The evolution of the characteristic mass for the blue population shows a slightly curved structure. The characteristic mass rises from $z = 1.0$ to $z = 0.2$ by a fac-

Table 7.1: Fitted Schechter parameters for both galaxy populations in the combined data of the COMBO-17+4 survey. The characteristic masses M^+, the normalization factor Φ^+ and the fixed slope β, adapted from Borch et al. (2006), are given.

Redshift	Galaxies [nr]	M^+ [$M_\odot$]	Φ^+ [$\times 10^6$ Mpc^{-3} Mass^{-1}]	β_{fixed}
C17p4 RED				
0.20-0.48	2111	8.03E+10 $\pm$ 4.59E+09	36.08 $\pm$ 2.01	0.30
0.48-0.60	607	9.13E+10 $\pm$ 6.55E+09	19.10 $\pm$ 1.30	0.30
0.60-0.79	759	1.10E+11 $\pm$ 6.41E+09	13.13 $\pm$ 0.77	0.30
0.79-0.94	1037	1.12E+11 $\pm$ 7.91E+09	22.90 $\pm$ 1.69	0.30
0.94-1.07	714	8.20E+10 $\pm$ 4.99E+09	11.42 $\pm$ 0.65	0.30
1.07-1.19	556	1.07E+11 $\pm$ 9.18E+09	12.00 $\pm$ 0.79	0.30
1.19-1.30	315	1.05E+11 $\pm$ 1.04E+10	22.66 $\pm$ 1.79	0.30
1.30-1.55	403	1.37E+11 $\pm$ 1.10E+10	5.32 $\pm$ 0.36	0.30
1.55-1.78	324	7.85E+10 $\pm$ 1.66E+10	8.22 $\pm$ 3.63	0.30
1.78-2.00	73	1.96E+11 $\pm$ 4.43E+10	1.66 $\pm$ 0.28	0.30
C17p4 BLUE				
0.20-0.48	4472	1.15E+11 $\pm$ 1.74E+10	11.15 $\pm$ 0.87	-0.45
0.48-0.60	1811	8.11E+10 $\pm$ 8.91E+09	6.75 $\pm$ 0.37	-0.45
0.60-0.79	1812	9.20E+10 $\pm$ 1.17E+10	4.59 $\pm$ 0.25	-0.45
0.79-0.94	1767	6.11E+10 $\pm$ 7.94E+09	5.85 $\pm$ 0.37	-0.45
0.94-1.07	1895	7.28E+10 $\pm$ 6.10E+09	7.17 $\pm$ 0.25	-0.45
1.07-1.19	1068	1.01E+11 $\pm$ 1.06E+10	6.00 $\pm$ 0.27	-0.45
1.19-1.30	862	1.10E+11 $\pm$ 1.21E+10	17.81 $\pm$ 0.84	-0.45
1.30-1.55	929	1.22E+11 $\pm$ 1.21E+10	3.20 $\pm$ 0.15	-0.45
1.55-1.78	424	1.16E+11 $\pm$ 2.13E+10	2.82 $\pm$ 0.34	-0.45
1.78-2.00	242	1.79E+11 $\pm$ 5.03E+10	1.41 $\pm$ 0.14	-0.45

tor of ∼1.8. However, from $z = 2.0$ to $z = 1.0$ M^+ decreases by a factor of 2.9. Even if we exclude the highest redshift bin – because of the large errors caused by only four data points to calculate the mass function – the characteristic mass still decreases by a factor of 1.9. Taking into account that we still have to face cosmic variances (which are not included in our error bars) we can say that our results support an almost constant value of M^+ for the blue population. The overall picture resulting from the measured M^+ shows no growth in the charactersitic mass neither for the blue nor for the red galaxy population.

We can compare our results in the redshift range of $z = 0.2$ to $z = 1$ with the results by Borch et al. (2006), who almost used the same fields of view. The S11 and A901 field are identical in both sets but we are using the A226 field instead of the CDFS. We still have to take into account that the data for the COMBO-17+4 is based on an H band selected catalog, whereas Borch et al. (2006) used the R band selected catalog from the COMBO-17 survey. The results for the evolution of M^+ for the red population match perfectly between both surveys (see Figure 7.8 middle panel). The results by Borch et al. (2006) for the blue population in the COMBO-17 survey is afflicted with high error bars in all analyzed redshifts bins. Therefore it is difficult to compare our results with theirs. However, within the error bars our results agree very well, besides the fact that the results by Borch et al. (2006) do not indicate a decrease in M^+ at $z \sim 1$ (see Figure 7.8 bottom panel). In fact, Borch et al. (2006) wrote that M^+ stays constant for blue galaxies up to $z = 1$. If we are looking at our results for the redshift range $0.2 < z < 1.0$ we would not be able to confirm that, but as already mentioned above, the overall trend from $z = 0.2$ to $z = 2.0$ in our results also indicates a constant value of M^+.

Within the last years several studies for mass functions at $z > 1.0$ were accomplished. Ilbert et al. (2010) used the COSMOS survey to create mass functions from $z = 0.2$ to $z = 2.0$. They separated their galaxy sample into a quiescent, a moderate star forming and a heavy star forming population. Their results with respect to the characteristic mass M^+ for the blue population are in good agreement with our results. Their population of galaxies with a high star forming activity shows a constant M^+ from $z = 2$ to $z = 0$. However, their population with an intermediate star forming activity even grows in M^+ with lower redshift. These two separate populations by Ilbert et al. (2010) are combined in our blue population. As Ilbert et al. (2010) do not present a combined mass function for both star forming populations in their sample we are not able to verify, if a growth in M^+ would still be visible in such a mass function. Ilbert et al. (2010) also detected an increase of the characteristic mass M^+ for the quiescent galaxies in their sample from $z = 2$ to $z = 0$. This means that their results regarding the red population are in contradiction with the ones made by Borch et al. (2006) using the COMBO-17 and with the results from the COMBO-17+4 data in this thesis. In fact, a growth of the characteristic mass M^+ of red galaxies would be expected because of the growing mass density at

lower redshift (see Section 7.4.2). The discrepancy between Ilbert et al. (2010) and the COMBO-17+4 survey with respect to the characteristic mass M^+ for the red population is not understood.

7.4.2 Analysis of the Mass Density

We also analyze the evolution of the mass density ρ_* from $z = 2$ to $z = 0.2$ in both populations. For this, we integrate the masses of all galaxies within our completeness limit. Because this limit only includes massive galaxies with $M > 3 \times 10^{10} M_\odot$ in blue and $M > 10^{11} M_\odot$ in red we decided to analyze the evolution twice: Once in the redshift area of $0.2 < z < 1.0$ – a sample which also includes galaxies with lower masses – and once a sample, covering the total redshift regime $0.2 < z < 2.0$, which includes only massive galaxies.

To get comparable numbers we have to correct our redshift slices for different volumes and normalize the density on solar masses per Mpc. For the redshift bin $0.2 < z < 1.0$ we limit the sample to galaxies with masses $M > 10^{10} M_\odot$ for the red population and $M > 4 \times 10^9 M_\odot$ for the blue population. For the second sample we demand a minimum mass of $M = 3 \times 10^{10} M_\odot$ for both populations. This means that the second sample is incomplete for the red galaxy population at $z > 1.78$. The results for both samples can be seen in Figure 7.9.

The mass density for the blue population stays almost constant from $z = 1.0$ to $z = 0.2$ but the mass density for red galaxies increases in the same redshift range by a factor of 3. These results are in agreement with the results by Borch et al. (2006). If we take a look at the total evolution of the mass density since $z = 2.0$ we see that there is 4.5 times more mass accumulated in blue galaxies today than at $z = 2.0$. Red galaxies show an even more drastic evolution: We see an increase by a factor of 18 in the mass density from $z = 2.0$ to $z = 0.2$ for the red galaxies. Taking the incompleteness for the red population at high redshift into account we can assume an even higher factor. This increase is indeed expected as red, evolved galaxies should become more numerous in an aging universe. These results also indicate that the total stellar mass density doubled since $z = 1$. This result was also mentioned by Borch et al. (2006).

Ilbert et al. (2010) analyzed the S-COSMOS survey and found an increase in the stellar mass density of quiescent galaxies between $z = 2.0$ and $z = 1.2$ by a factor of 10, which would imply a dramatic change in the mass density in a time period of only ~ 2 Gyr. Within the same time period we only measure an increase by a factor of ~ 4.5 – in the COMBO-17+4 survey the largest increase in the mass density of the red galaxies happens at lower redshifts. This is in contradiction to the results by Ilbert et al. (2010) who do not measure any large

changes in the mass density for the red galaxies at $z < 1.0$. Brammer et al. (2011) also investigated the mass density of blue and red galaxies at $z < 2.0$, using the NEWFIRM survey. Their results for the red galaxies are in agreement with ours (increase in mass density by a factor of ~ 10). Like in the COMBO-17+4 they found almost no evolution of the blue galaxy population. The data from the NEWFIRM survey also show that the mass density of blue and red galaxies is almost identical at $z \sim 2.0$. This is also discovered in our data.

7.5 Massive red galaxies at high redshifts

Several studies made in the last years identified massive, red galaxies at $z = 2$ (Kriek et al., 2008; Williams et al., 2009; Brammer et al., 2011). van Dokkum et al. (2006) postulates that there is a significant population of massive ($M > 2 \times 10^{11} M_{\odot}$) galaxies in place at $2 < z < 3$. With respect to these results we look for a population of massive, red galaxies in the COMBO-17+4 survey.

Therefore we analyze massive galaxies in the redshift bin $1.78 < z < 2.0$. Within this redshift range we find 46 galaxies with masses $M > 2 \times 10^{11} M_{\odot}$. Out of these 27 are classified as red. 17 of them are detected in the A901 field, 8 in S11 and 2 in A226. One red galaxy in the S11 field has to be excluded because it was obviously a misclassification. Still, half the population of massive galaxies at $z \sim 2$ in our survey already has red colors.

The most massive galaxy is located in the A901 field ($M = 10^{12} M_{\odot}$ and $(U_{280} - V) = 1.7$). Its properties, as well as these of the other massive red galaxies in the A901 field, were already discussed by Nicol (2009). Within the A226 field both detected galaxies have a mass of $M = 2 \times 10^{11} M_{\odot}$. The masses of the selected galaxies in the S11 field range between 2-3 $\times 10^{11} M_{\odot}$, with two galaxies being more massive: One object at $z = 1.9$ has a calculated stellar mass of $M = 5 \times 10^{11} M_{\odot}$ and a color of $(U_{280} - V) = 1.1$. The other object is found at $z = 1.9$ with a stellar mass of $M = 6.2 \times 10^{11} M_{\odot}$ and a color of $(U_{280} - V) = 1.2$. Both of them are therefore neither as massive nor as red as the most massive red galaxy detected in the A901 field.

Our results are supported by those of the works mentioned above. However, to verify the redshift of these objects in the COMBO-17+4 survey and to learn more about their properties spectroscopic data are necessary. van de Sande et al. (2011) already used the X-shooter spectrograph which was mounted on the VLT to confirm the results of the high massive red galaxies in the NEWFIRM survey. Until we have verified the distance and the masses of these galaxies we have to speculate if we miscalculated their masses or if they are just very rare objects which are very unlikely to find.

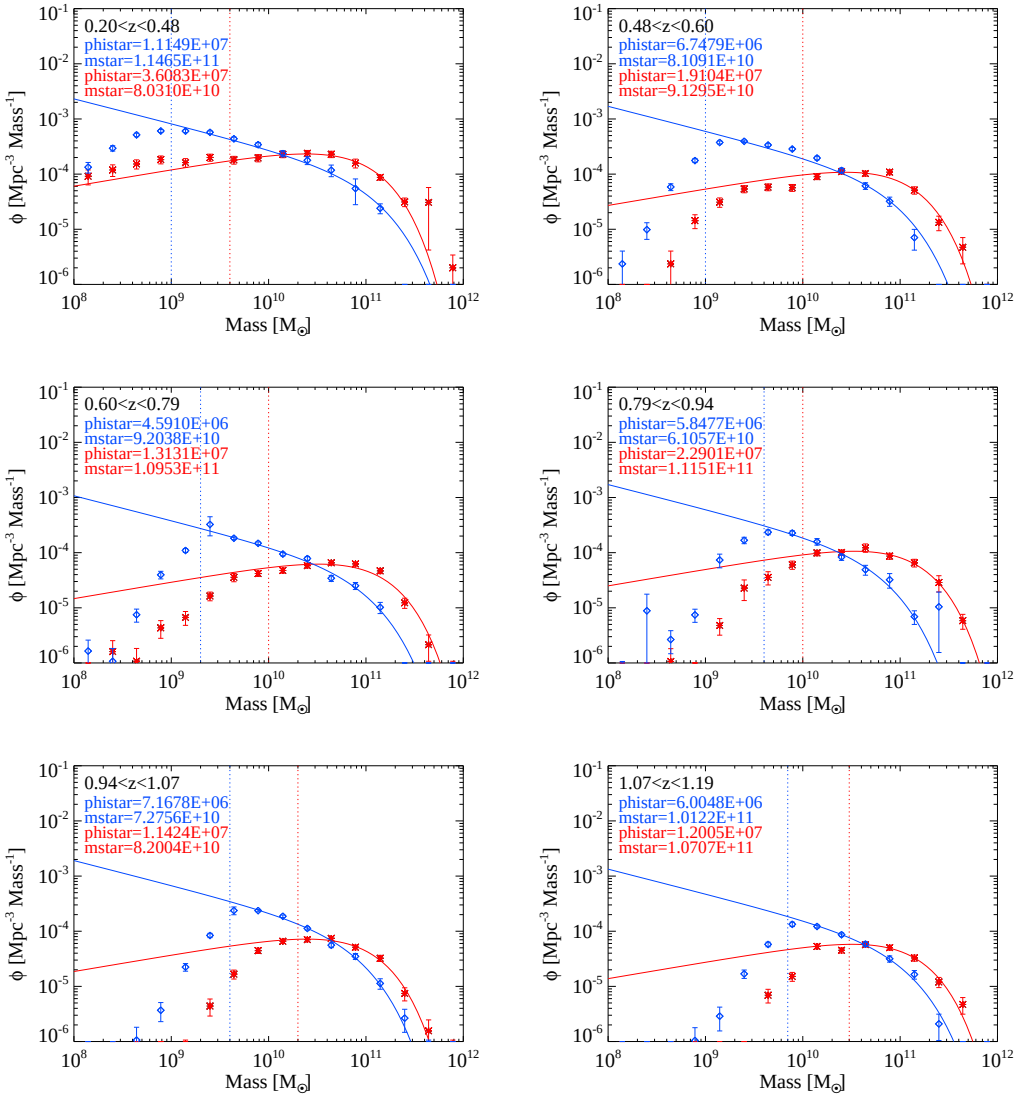

Figure 7.6: Mass functions for different redshift bins for the combined data from the COMBO-17+4 survey. The calculated characteristic masses M^+ as well as Φ^+ for the blue and the red population are given. The vertical line indicates the magnitude limit which is used to calculate the luminosity function in each redshift bin.

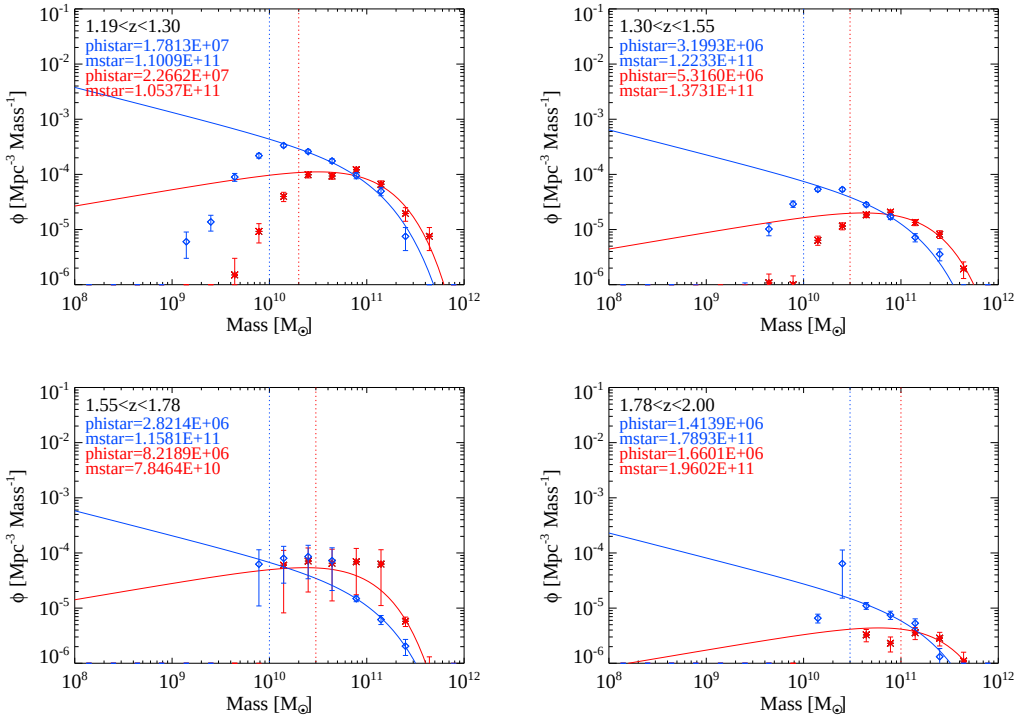

Figure 7.7: Mass functions for different redshift bins for the combined data from the COMBO-17+4 survey. The calculated characteristic masses M^+ as well as Φ^+ for the blue and the red population are given. The vertical line indicates the magnitude limit which is used to calculate the luminosity function in each redshift bin.

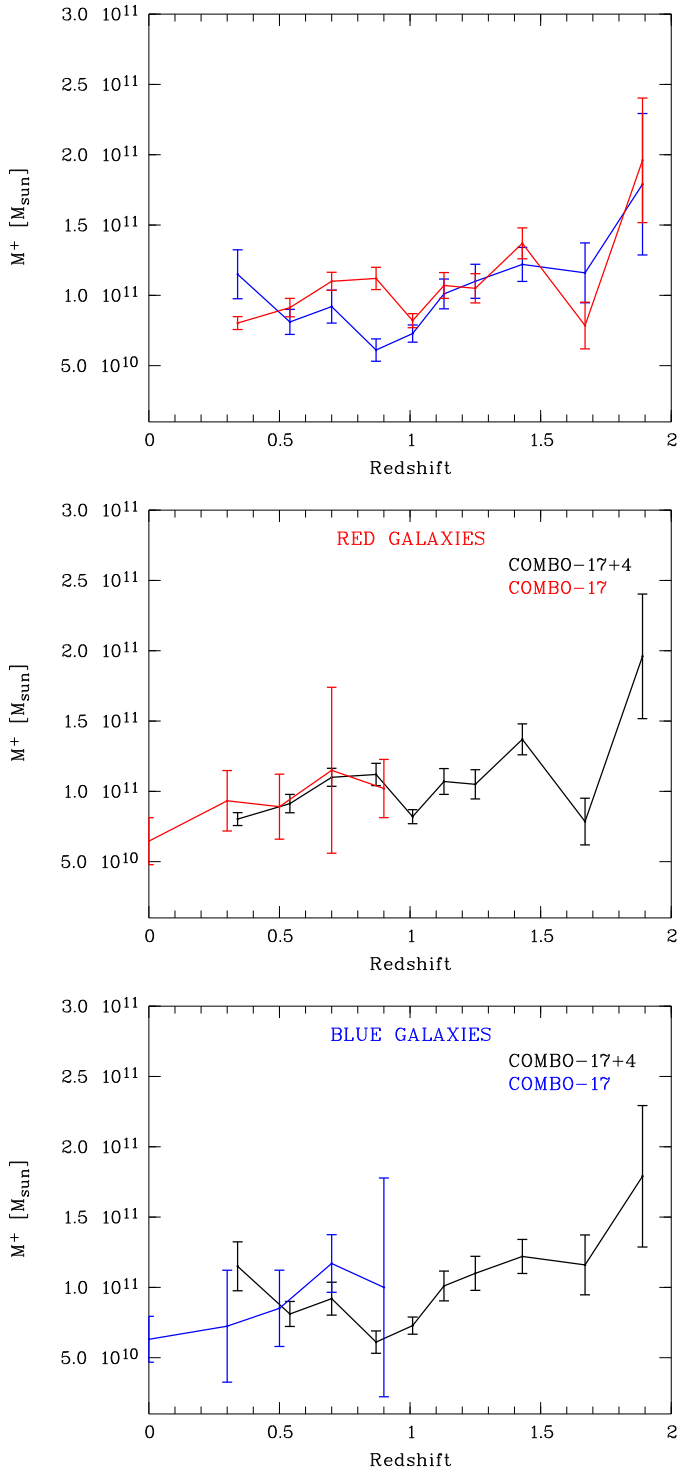

Figure 7.8: Evolution of the characteristic mass M^+ in redshift. The top panel shows the results from the blue and the red population in the combined COMBO-17+4 survey. The lower two panels compare our results with those from the COMBO-17 survey, analyzed by Borch et al. (2006).

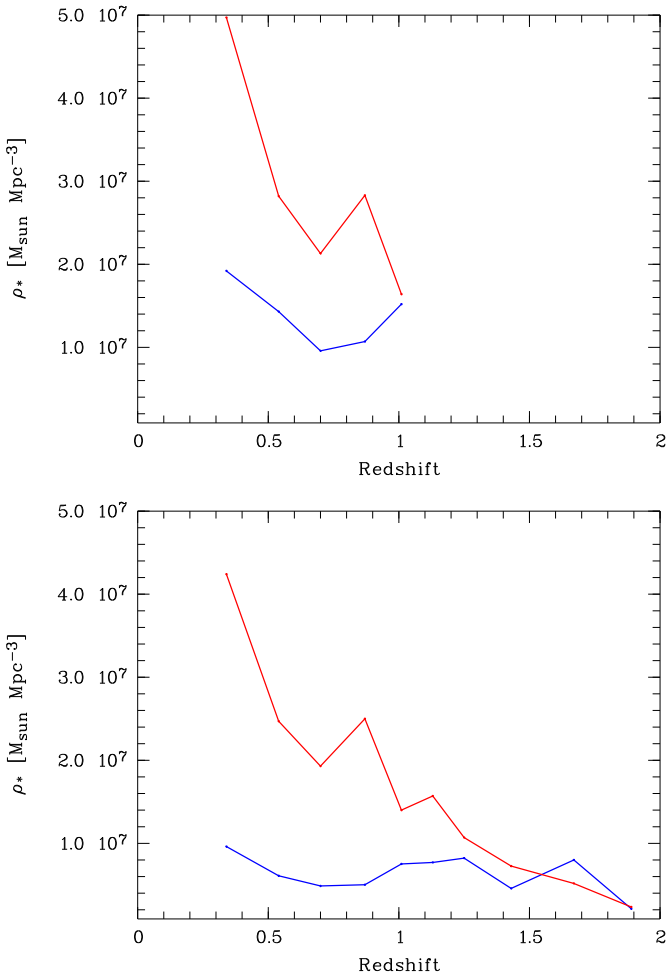

Figure 7.9: The evolution of the mass density ρ_* in redshift. The top panel only includes galaxies at $z < 1.07$ and with masses $M > 10^{10} M_\odot$ for the red galaxies, respectively $M > 4 \times 10^9 M_\odot$ for the blue galaxies. The bottom panel shows ρ_* at $z < 2.0$ with a minimum stellar mass of the galaxies of $M = 3 \times 10^{10} M_\odot$.

Chapter 8

Summary

This thesis described the data analysis of two fields (Abell 226 and S11) in the COMBO-17+4 survey – a multi-wavelength survey, which combines 17 optical with 4 near infrared filters – including the explanations in the changes of the data reduction pipeline. For both fields we created a H band selected catalog and combined the analyzed data from Abell 226 and S11 with the already by Nicol (2009) analyzed data from Abell 901. The combined catalog covers 0.625 square degrees and contains 42,134 galaxies at $z < 2.0$ and 452 QSOs. We separated the galaxies detected in the survey into a red and a blue population. This way we analyzed the evolution of the red sequence in the redshift of $0 < z < 2$. In addition we created separate luminosity functions for the red and the blue galaxy population for the two analyzed fields as well as for the complete COMBO-17+4 survey. At last we studied the evolution of the mass function, again separate for the blue and the red galaxy population.

In this summary we want to answer the questions asked at the beginning of this thesis in Section 1.5, based on the results of our data:

Are the photometric measurements from the COMBO-17+4 survey useful? We do not have spectroscopic measurements of our objects to verify the calculated redshifts and the determined classes. However, the analysis of suspicious overdensities, the distribution of the SEDs in redshift, as well as the positions of our galaxies in the color-magnitude diagrams support our results. Still a careful selection of the analyzed objects in case of magnitude limits had to be done. In addition we are aware of of redshift focuses which were identified at three different redshifts. If we take these disadvantages into account very good statistics can still be done with the data from the COMBO-17+4 survey. For the analysis of individual objects a careful analysis of the fitted SED template should be done.

Up to which redshift can we see the red sequence? We were able to identify the red sequence in both analyzed fields up to a redshift of $z > 1$. In both fields we found the red sequence following a linear evolution in $(U_{280} - V)$

over time, but we also found that the red sequence in the Abell 226 field is about 0.3 mag redder than in the other to fields of the survey. In the same field we also detected only a very small number of red galaxies at $z > 1.75$. In the Abell 226 field we measured the existence of the red sequence at $z = 1.2$. In the S11 field we were able to measured the sequence at $z = 1.3$ and we found indications of its existence to $z \approx 1.60$. However, due to small number statistics we were not able to measure the peak in the error-weighted color distribution of these galaxies. To verify the existence of the red sequence at $z > 1.3$ a larger number of objects is required.

How is the luminosity function evolving and are there differences between the blue and the red galaxy population? We were able to create luminosity functions for 22,181 galaxies at $z < 2.0$. By analyzing the functions for the red and the blue galaxy populations (separated by their color bimodality in $(U_{280} - V)$) in 10 redshift bins for both analyzed fields and the COMBO-17 survey in total we got information on the evolution of both populations from $z = 2.0$ to $z = 0.2$. We found a dimming in M_B in the blue galaxy population of ~ 1 mag and in the red population of ~ 1.6 mag from $z = 2.0$ to $z = 0.2$ and a rise in the number density of red galaxies. However, the number density of blue galaxies stayed constant. The results are in agreement with the ΛCDM model: With the age of the universe raising, the star formation rates is lowering the total number of evolved galaxies rises.

How is the stellar mass function evolving and are there differences between the blue and the red galaxy populations? We studied the evolution in stellar mass of the blue and the red population separately in ten redshift bins from $z = 2.0$ to $z = 0.2$. Our data showed that the characteristic mass M^+ stays almost constant over the observed redshift range for both populations which indicate no growth in the mass for neither the blue nor the red galaxies. An investigation of the mass density for galaxies with masses of $M > 3 \times 10^{10} M_\odot$ showed that the mass density for blue galaxies stays almost constant from $z = 2.0$ to $z = 0.2$ whereas the mass density for red galaxy was growing by a factor of $\sim$15. These results are in agreement with our cosmological picture of an evolving and aging universe.

Can we find high massive, red galaxies at high redshifts? Using the calculated stellar masses we were able to identify a few red galaxies at $z > 1.78$ with masses of $M > 10^{11} M_\odot$. Two massive red galaxies with $M \approx 2 \times 10^{11} M_\odot$ were identified in the Abell 226 field. Additionally seven massive red galaxies were detected in the S11 field. The most massive red galaxy detected contains a stellar mass of $M = 6.2 \times 10^{11} M_\odot$ and a distance of $z = 1.9$. We were not able to detect a galaxy with $M \approx 10^{12} M_\odot$ as Nicol (2009) in the Abell 901 field. Our results indicate that these objects are indeed very rare and the objects detected still have to be verified.

The resulting catalog of the COMBO-17+4 survey which is now available

with this thesis can be used for further scientific projects: Within this thesis we did not analyze the population of QSOs which were detected in the survey. We also only took a brief look of specific interesting objects. In addition the data can be used to study gravitational lensing. A further topic is the gathering of spectra for the identified high redshift galaxies to verify their calculated redshift and their passive nature.

Appendix A

Photometric setup file

Table A.1: Setup file for the MPIAPHOT routine EVALUATE/IMAGE. The same setup has already been used to analyze the data of the Abell 901 field and is very similar to the setup file of the COMBO-17 survey.

0	2			>	(TEST,CLEAN,POL),FIX_PSF,EFF_PSF
22	0	2.27	0.00	>	SUM:(W_SUM,SUM),-,APERT,PSF:SX,SY,AL
0	20	0.0000		>	FIT:(yes/no),ITER,CHI_LIM,SATUR/1000
1	21	0.0000		>	BACK:(FIT,L,HST),HW,S_LOC,B_OFF/1000
1	2	4.00	0.00	>	PROF:(DIRT,EDGE),R_MIN,X,S_DIRT,-
11	20	0.00	0.00	>	MAXI:(FIX,FILT),ITER,RAD,X0,Y0,-

Appendix B

Step by Step Data Reduction

B.1 Preparation of the Data Reduction

Transform the data (stored in the catalog raw.cat) from *fits to *bdf files, following the MANOS name convention.

```
@@ combo_name o2k YYMM = raw:  O2k_YYYYMM_run ./
```

Runs from the years 2003 and 2004 are using older headers which have to be updated to the actual format:

```
@@ PM:O2k_fix_descrs
```

In addition some headers don not have the descriptor O_POS or the descriptor is written wrong:

```
@@ PM:O2k_corr_opos
```

B.2 Creation of a Bad Pixel Mask

Frames using the filters NB2122, NB1207 or NB1083 are used. A catalog named flat.cat, containing all flatfield images.

```
create/icat flat
```

The descriptor epsilist, which contains information about the used filters (in the example the filter NB2122), is written:

```
process/ima write/desc flat:  epsilist/c/1/80
mirror,O2k_optics,O2k_fpa77,NB2122
```

The bias is measured, using the files in the flat.cat catalog. In addition three files with the prefix BPM_flat, are created.

```
bias/extrapolation BPM_flat = flat:
```

Using the new created files the slope, rms and const can be measured. The median and σ value are written down manually:

```
stat/ima BPM_flat_slope.bdf

plot/histo BPM_flat_slope

stat/ima BPM_flat_rms.bdf

plot/histo BPM_flat_rms.bdf

stat/ima BPM_flat_const.bdf

plot/histo BPM_flat_const.bdf
```

Now the slope, rms and const images are cutted at their 3 σ values. The names of the new images contain the σ-values, year and the month of the run:

```
replace/ima BPM_flat_slope BPM_3s_yymm_slope mean-3σ,mean+3σ=0,1

replace/ima BPM_flat_rms BPM_3s_yymm_rms 0,mean+3σ=0,1

replace/ima BPM_flat_const BPM_3s_yy_mm_const mean-3σ,mean+3σ=0,1
```

The three BPMs are combined and normed to pixel values of 0 or 1:

```
compute/ima BPM_yymm_combine = BPM_3s_yymm_slope + BPM_3s_yymm_rms
+ BPM_3s_yymm_const

replace/ima BPM_yymm_combine BPM_yymm_final 1,3=1,0
```

The file ***_final** is used for the data reduction.

B.3 Creation of a Main Domeflat

Two types of files are available. Either the illumination in the dome was on or off. For both we create a separate catalog (raw_on and raw_off) and write the corresponding epsilist descriptor (in our example we use the H filter):

```
create/icat raw_on raw_filteron*

create/icat raw_off raw_filteroff*

process/ima write/desc raw_on:  episilist/c/1/80
mirror,O2k_optics,O2k_fpa77,H_O2k

process/ima write/desc raw_off:  episilist/c/1/80
mirror,O2k_optics,O2k_fpa77,H_O2k
```

All images with an activated illumination are now summed up in the image

dome_on_sum_filter (whereas filer is replaced with the actual filter name):

```
compute/ima dome_on_sum_filter = raw_filteron_Domeyymmxxx1 + ...
+ raw_filteron_Domeyymmxxx1
```

Now the saturation level of the images has to be changed according to the number of summed up images. The forth value of the descriptor ccd_para should have the value 30.000 x Ncoadds, x number of dome_on-files:

```
write/desc dome_on_sum_filter ccd_para/r/4/5 forth value
```

In the next step dome_off files are summed up in the image dome_off_sum_filter. An adaption of the saturation level is not necessary, as the dome_off files are not saturated.

```
compute/ima dome_off_sum_filter = raw_filterof_Domeyymmxxx1 + ...
+ raw_filterof_Domeyymmxxx1
```

Now the summed up file with a not activated illumination are subtracted from the summed up file with an active illumination. This so created catalysator image, named dome_cata_filter is then normalized using its median value. The normalized catalysator image is stored with the name dome_cata_norm_filter:

```
compute/ima dome_cata_filter = dome_on_sum_filter -
dome_off_sum_filter

read/desc dome_cata_filter fr_stat

compute/ima dome_cata_norm_filter = dome_cata_filter /
median_value
```

B.4 Reduction of a Flatfield in the H Band

All flatfields are stored in the catalog raw.cat. The descriptor epsilist is updated according to the H band filter. In a third step the counts of the flatfield images are transformed into electrons. The transformed images have the prefix prp_:

```
create/icat raw *bdf

process/ima write/desc raw:  episilist/c/1/80
mirror,O2k_optics,O2k_fpa77,O2k_filter

prep/ccd prp_ = raw:
```

The transformed images are stored in the catalog prep.cat:

```
create/icat prep prp_*
```

Now an averaged flatfield (named dusk_average.bdf) is created using the normalized dome-flat of the filter as catalysator file to reduce the fixed pattern noise. Afterwards the flatfield is normalized using its median value, which can be read out by the stat/background command. The name of the normalized flatfield contains the filter and the year (YY) and the month (MM) of the observation run:

```
flat/catal dusk_average.bdf = prep:  5.,3 X WINDOW 0
dome_cata_norm_H

stat/background dusk_average.bdf

compute/ima duskH_yymm_norm.bdf = dusk_average.bdf / median_value
```

B.4.1 Reduction of Dusk and Dawn Flatfields in J1, J2 and Y

The reduction of flatfields in the filter J1, J2 and Y are identical to the H band with the exception of the reduction of the reflection of the main mirror on the images. Only the last steps - which are different - are shown here.

The normalized flaltfield gets the name dusk_ring.bdf.

```
compute/ima dusk_ring.bdf = dusk_average.bdf / median
```

Now the image is loaded into the display to measure the background of the ring, which is done manually. The background is saved in the image flat_ring. Afterwards the background is subtracted and the identified reflection is stored in the image ring_ring.bdf. The identified ring is then subtracted from the normalized flatfield. The final flatield is then stored with the same name convention as for the H band:

```
load/ima dusk_ring.bdf

fit/flat flat_ring = dusk_ring cursor 2,2 background

find/ring ring = flat_ring cen=1024,1024

compute/ima duskY_yymm_norm.bdf = dusk_ring.bdf - ring_ring.bdf
```

B.5 Reduction of Science Frames

For a reduction of the science images, a flatfield, BPM and dark (dummy) file have to be available. The name of the used filter has to be adapted in the file names. First the raw files for each run and each filter are stored in a separate catalog (named raw.cat). The images in these catalogs are then updated with

the epsilist (containing the correct filter name), opt_axis and lambda (containing the correct wavelengths according to the used filter) descriptor:

```
create/icat raw raw*bdf

process/ima write/desc raw:  epsilist/c/1/80
mirror,O2k_optics,O2k_fpa77,O2k_filter

process/ima write/desc raw:  opt_axis/d/1/2 1024,1024

process/ima write/desc raw:  lambda/r/1/4 λc,Δλ,λ3,λ4
```

The Omega2000 context is activated:

```
set/cont omega2k
```

The Omega2000 pipeline is stared, using the standard parameters, the correct flatfield (dusk_norm.bdf), a Bad Pixel Mask (BPM_final.bdf) and a dummy file, containing no real information, for the dark (dark.fits):

```
o2k/science icatalog=raw frames=5,1.5,0 mode=2,3 sum=9,0,1
kappa_sum=5

flatfield=dusk_norm.bdf,BPM_final.bdf,dark.fits
```

The output files of the pipeline with the prefix re2_ are stored in a new catalog, named red2.cat. Then these images are transformed from counts to electrons:

```
create/icat red2 re2_*

prep/ccd prp_ = red2:
```

The transformed images are stored in the catalog prep.cat and the coordinate system is changed to word coordinates:

```
create/icat prep prp_*

corr/ima cor_ = prep:
```

The images with the new coordinates are stored in the catalog corr.cat. As the images therein still can contain a quadrant structure from the Omega2000 detector, they get flattened:

```
create/icat corr cor_*

@@ PM:O2k_flatten_quadrants qua_ = corr:
```

The output images from the flattening routine have the prefix qua_ and are now stored in the catalog quadrant.cat:

```
create/icat quadrants qua_
```

The images in the quadrant.cat catalog get a new descriptor, containing the

name of the corresponding Bad Pixel Mask:

```
process/ima write/desc quadrants:  bpm_id/c/1/80 BPM_ID
```

For all following steps all quadrant-corrected images of one filter have to be in one folder; including their BPMs. The images are changed to gnomonic projections, the reference position of the images is determined using the 2MASS catalog.

To be able to change the images later to gnomonic projections a reference position is needed, which we get using the 2MASS catalog. Afterwards we have to give the center of the field of view ([Ra DEC]):

```
create/table Field_2MASS 14 376 2MASS_input.dat jaeger.fmt

set/refpos Field_2MASS = other [RA DEC]
```

Now the coordinates are transformed in η and ξ and these two columns are added to the table. As well as the descriptor tab_form, which is containing the name of the used filter.

```
@@ PM:radec2xy_tab A226_2MASS

write/desc A226_2MASS.tbl tab_form/c/1/8 H
```

To shift every single image within the quadrant.cat catalog to the reference catalog we identify the brightest objects on each image and use them as reference points to calculate the shifts:

```
find/obj quadrants:  200 keep psf

find/move Filter_2MASS quadrants:  all 60

mosaic/gnomima gno_ = quadrants:  0.33
```

The gnomonic projected images have the prefix gno_ and are stored in the catalog gnom.cat:

```
create/icat gnom gno_*
```

Using the gnomonic projectes images we create a median image named median_ID. Whereas the file with the name median_ID should contain the name of the field and the filter (e.g. A226_H). The two created images have the prefixes med_ and rms_:

```
mosaic/median median_ID = gnom:
```

Using these images and the gnomonic projected frames cosmics are removed:

We write the new descriptors bpm_root and remove cosmics from the gnomonic projected images using the median image median_ID (without the

prefixes med_ or rms_):

```
process/ima write/desc gnom:  bpm_root/c/1/4 qua_

mosaic/rmcosmics cos_ = gnom:  median_ID 1
```

The output images have the prefix cos_ and are stored in the catalog cosm.cat. The identified cosmics are now removed from the images in the quadrant catalog:

```
create/icat cosm cos_*

mosaic/copycos out_ = cosm:  qua_
```

The output images with the prefix out_ are now flatfielded, do not contain dark current, bad pixels or cosmics and are stored in the catalog output.cat:

```
create/icat output out_*
```

The images in the output.cat catalog can now be summed up. As they are no longer gnomonic projected, this procedure has to be done again (this time using the prefix gn2_ and the catalog gnom2.cat). The name of the summed up image contains the prefix sum_, the name of the field and the Name of the filter:

```
find/obj output:  200 keep psf

mosaic/gnom gn2_ = output:

create/icat gnom2 gn2_*

mosaic/sumup sum_Field_filter = gnom2:  0,0,0,0
```

B.6 Photometric Calibration of the Frames

We start with measuring the seeing on the summed up image (in setting the parameter *psf*) and adding the descriptor mosaic:

```
find/obj sum_Field_filter 800 keep psf

write/desc sum_Field_H mosaic/I/1/1 1
```

Now a Source Extractor table (with the prefix sex_) is created, identifying all objects visible on the deep H band image. Contaminating objects at the borders of the image (the borders have to be defined manually in giving the cuts x1,y1,x2,y2) and in the halos of bright stars are then removed from the table. The cutted table is stored with the name Master_Field_table:

```
find/sex sex_ = sum_Field_H 5.5 ?  ?  BACKGROUND weight
```

```
select/sex cut_ = sum_Field_H.bdf sex_ x1,y1,x2,y2 yes

halos/sex cut_Field_H 12 5 X 3

master/sex Master_Field_table = cut_Field_H
```

The master table contains a coordinate system which is projecting the object on the celestial sphere. These coordinates have to be recalculated for the individual images (stored in the catalog output.cat). The so created tables, with the prefix mark, contain only objects which are visual on the individual frames:

```
master/section mark = output:  Master_Field_table
```

The absolute value of photons above the background is measured on each frame, using the evaluate procedure. Therefore the photometric setup file with the name e17o.eval has to be available (see Appendix A for the content of this file). The output files of this procedure also have the prefix e17o and are stored in the catalog phot.cat:

```
eval/ima e17o = output:  mark

create/tcat phot e17o*tbl
```

Now the measured fluxes have to be calibrated. Therfore the context flux_cal is started and the Mastercatalog is defined:

```
set/cont flux_cal

flux/refer Master_field_table
```

The stars which are going to be used as standard stars are now flagged in the master table and a name for each star is given (see Table 3.4 for the list of used standard stars):

```
flux/std Master_Field_table column_nr Field_01
```

Now calibration stars are searched on each table in the phot.cat catalog. In addition a reference table for each subfield is defined (in the examples the 1st, 10th, 20th and 30th table in th catalog):

```
flux/selnorm phot:  = N 1 0.9,0.005,15.0,20.0,4.0 check

flux/setnorm phot:1,10,20,30 set
```

The data is now checked for all necessary descriptors and the presence of the images containing information about bad pixels and cosmics. Afterwards the individual tables in the phot.cat catalog are united in a singe flux table, named flux_field_filter.tab:

```
flux/verify output:  cmsk

flux/unite flux_field_filter = phot:
```

The fluxes in the table are now normalized using the normalization stars and then calibrated using the standard stars. The information for our standard stars was stored in the table standards.tbl:

```
flux/norm flux_Field_filter all 10 150 10

flux/integ flux_Field_filter = /photo/user/tbl/PHOTSTDS/standards.tbl
```

B.7 Photometry of the COMBO-17 Data

The images containing the optical data from the COMBO-17 survey have to be sorted by their filter and runs. As they are already reduced, only a few things have to be done. First the WFI context has to be activated and as the images were stored in the *.fits format they have to be transformed into the midas intern *.bdf format:

```
set/cont WFI

indisk/fits all_fits.cat all_bdf.cat
```

The images for each filter and each run are then stored in two separate catalogs named cosm.cat (containing the science frames) and cmsk.cat (containing the information in bad pixels and cosmics):

```
create/icat cosm cosm*.bdf

create/icat cmsk cmsk*.bdf
```

Now the images are updated for the use within the COMBO-17+4 survey, whereas it is important to give the filters names of four signs. The fourth name has to be the name of the run (e.g. 915a):

```
@@ prepare_test sum_field_filter.bdf cosm:  wfi_filter filter

process/ima write/desc cosm:  ccd_para/r/5/5 105000

process/ima write/desc cmsk:  ccd_para/r/5/5 105000
```

On each science frame the brightest 40 objects are now identified and used to calculate the shift to the summed up H band image:

```
@@ findobj_test cosm:  40

@@ fimove_test sum_Field_H.bdf cosm:  s ?  ?  0.005,0.01,0.3,0.1
```

The following command is identical withe the command `master/section` from the COMBO-17+4 survey and creates tables for the objects found on each individual image:

```
@@ project_test mark = cosm:  Master_Field_table.tbl
```

We start again the evaluation procedure and store the output tables in the phot.cat catalog. We also have to update two descriptors in the evaluate tables:

```
eval/ima e17w = cosm:  mark

create/tcat phot e17w*.tbl

process/ima write/desc phot:  oa_pix/d/1/2 5694,4051

process/ima write/desc phot:  borders/r/1/4x1,y1,x2,y2
```

At last one of the descriptors xy_move_xx has to be changed int the descriptor xy_move. Therefore a subprogram is necessary:

```
@@ PM:listname phot: I
write/key I_part/i/1/1/ 1
do i_part = 1 {no_names}
 run PM:get_name
  copy/dd {part_nn} xy_move_a01/r/1/6 {part_nn} xy_move/r/1/6
enddo
```

We activate the flux_cal context and define the Master table:

```
set/cont flux_cal

flux/refer Master_field_table.tbl
```

Now we search for normalization stars in the evaluate tables and define a reference table (the 1st one, in the example):

```
flux/selnorm phot:  = N 1 0.92,0.003,15.0,0.20.0,4.0

flux/setnorm phot 1
```

At last we verfiy the existence of all necessary descriptors and the presence of the cmsk-images. Then we can unite the evalute table in one flux table, normalize the fluxes using the normalization stars and then the standard stars (again the information of the standard stars was stored in the table standards.tbl):

```
flux/verify cosm:  cmsk

flux/unite flux_Field_filter_run = phot:

flux/norm flux_Field_filter_run all 10 150 10

flux/integ flux_Field_filter_run = /photo/user/tbl/PHOTSTDS/standards.tbl
```

Finally we are computing the column scratch1 by dividing the error of the Flux by the Flux:

```
comp/table flux_Field_filter_run.tbl :scratch1 = sFcFilterRUN /
:_F_FilterRUN
```

B.8 Flux calibration and Objects Analysis

We put the flux tables of all filters and runs in one directory and create a catalog which contains all these fluxables. Then we combine all fluxes into one table:

```
create/tcat flux_tables flux*tbl
```

```
flux/combine flux_Field_combine = flux_tables:  50 "‘COMBO-17+4
Field"’ enable
```

To run all further programs appropriately we have to create additional columns (varflag, FI_1, FI_2, morph1 and morph2). Therefore we also need the master table:

```
comp/table flux_Field_combine.tbl :varflag = 0
```

```
copy/tt Master_Field_table :FI_1 flux_Field_combine.tbl
```

```
copy/tt Master_Field_table :FI_2 flux_Field_combine.tbl
```

```
comp/table flux_Field_combine.tbl :morph1 = :FI_1
```

```
comp/table flux_Field_combine.tbl :morph2 = :FI_2
```

We also have to rewrite the descriptor filter, as the filters are stored beneath each other and not next to each other:

```
@@ filter_update.prg flux_Field_combine
```

We also have to rewrite the entries in the column class for our standard stars, which contains at the moment the given name of the star, back to star:

```
@@ class_update.prg flux_Field_combine Master_Field_table
```

Now we are able to estimate the error in flux, calculate the colors of our objects and correct for variability. As a lot of things were different between the A226 and the S11 field two separate programs (i.e. mc_colors_A226 and mc_colors_S11) are available:

```
@@ mc_colors_Field flux_Field_combine uppl yes yes yes
```

To check if our detected stars are positioned on the main sequence we compare them with the stars in the Pickles (1998) library. If they do not fit the correction factors for the color indicies in the mc_colors_Field program have to be adapted:

```
@@ mc_mainseq_Field flux_Field_combine 20 2 ?  ?  R
```

After successfully calculating the color indices we can classify the objects in the table. Therefore a feature file (feature_manos_Field.par) is necessary which lists the used colors and the reference libraries:

```
@@ mc_classify flux_Field_combine ?  feature_manos_Field.par
```

In the next step the rest-frame magnitudes of the detected objects are calculated. Again, there are two separate programs for both subfields, because of the different extinction:

```
@@ mc_rest_lummass_C17p4_Field flux_Field_combine NIR
fKcorr_2D_2burst
```

Before we can continue, a zero-point correction has to be done. Therefore we need information from the master table, which is added as new columns to our flux table (columns are named mag_best and add_m_best). The zero_point_correction is the mean value of add_m_best and can either be determined for the whole field or for each subfield separately:

```
comp/table Master_Field_table :mag_best_err = 1 / :mag

comp/table flux_Field_combine :mag_best = :mag0

comp/table flux_Field_combine :add_m_best = :mag_best - :_M_H__

copy/tt Master_Field_table :mag_best_err flux_Field_combine

comp/table flux_Field_combine :add_m_best = :add_m_best -
zero_point_correction
```

With the added columns we can calculate the absolute magnitudes of our objects:

```
@@ mc_Mabs_C17p4.prg flux_Field_combine :add_m_best
```

Having the absolute magnitudes available we can finally calculate the masses of our objects:

```
@@ mc_masses_C17p4 flux_Field_combine
```

Bibliography

Barrado, D., Thiele, U., Aceituno, J., Pedraz, S., Sanchez, S. F., Aguirre, A., Alises, M., Bergond, G., Galadi, D., Guijarro, A., Hoyo, F., Mast, D., Montoya, L., Sengupta, C., de Guindos, E., and Solano, E. (2010). The Calar Alto Observatory: current status and future instrumentation. *ArXiv e-prints*.

Baum, W. A. (1962). Photoelectric Magnitudes and Red-Shifts. In McVittie, G. C., editor, *Problems of Extra-Galactic Research*, volume 15 of *IAU Symposium*, page 390.

Baumeister, H., Bizenberger, P., Bayler-Jones, C. A. L., Kovács, Z., Röser, H.-J., and Rohloff, R.-R. (2003). Cryogenic engineering for OMEGA2000: design and performance. In Iye, M. and Moorwood, A. F. M., editors, *Society of Photo-Optical Instrumentation Engineers (SPIE) Conference Series*, volume 4841 of *Society of Photo-Optical Instrumentation Engineers (SPIE) Conference Series*, pages 343–354.

Bell, E. F., McIntosh, D. H., Barden, M., Wolf, C., Caldwell, J. A. R., Rix, H., Beckwith, S. V. W., Borch, A., Häussler, B., Jahnke, K., Jogee, S., Meisenheimer, K., Peng, C., Sanchez, S. F., Somerville, R. S., and Wisotzki, L. (2004a). GEMS Imaging of Red-Sequence Galaxies at $z \sim 0.7$: Dusty or Old? *ApJL*, 600:L11–L14.

Bell, E. F., Wolf, C., Meisenheimer, K., Rix, H., Borch, A., Dye, S., Kleinheinrich, M., Wisotzki, L., and McIntosh, D. H. (2004b). Nearly 5000 Distant Early-Type Galaxies in COMBO-17: A Red Sequence and Its Evolution since $z \sim 1$. *ApJ*, 608:752–767.

Bertin, E. and Arnouts, S. (1996). SExtractor: Software for source extraction. *aaps*, 117:393–404.

Binggeli, B., Sandage, A., and Tammann, G. A. (1988). The luminosity function of galaxies. *Annu.Rev.Astron.Astrophys.*, 26:509–560.

Binney, J. and Merrifield, M. (1998). *Galactic Astronomy*.

Borch, A., Meisenheimer, K., Bell, E. F., Rix, H., Wolf, C., Dye, S., Kleinheinrich, M., Kovacs, Z., and Wisotzki, L. (2006). The stellar masses of 25 000 galaxies at 0.2 z 1.0 estimated by the COMBO-17 survey. *A&A*, 453:869–881.

Brammer, G. B., Whitaker, K. E., van Dokkum, P. G., Marchesini, D., Franx, M., Kriek, M., Labbé, I., Lee, K.-S., Muzzin, A., Quadri, R. F., Rudnick, G., and Williams, R. (2011). The Number Density and Mass Density of Star-forming and Quiescent Galaxies at $0.4 < z < 2.2$. *ApJ*, 739:24.

Cassata, P., Cimatti, A., Kurk, J., Rodighiero, G., Pozzetti, L., Bolzonella, M., Daddi, E., Mignoli, M., Berta, S., Dickinson, M., Franceschini, A., Halliday, C., Renzini, A., Rosati, P., and Zamorani, G. (2008). GMASS ultradeep spectroscopy of galaxies at $z \sim 2$. III. The emergence of the color bimodality at $z \sim 2$. *A&A*, 483:L39–L42.

Cirasuolo, M., , R. J., Dunlop, J. S., Almaini, O., Foucaud, S., Smail, I., Sekiguchi, K., and Simpson, C. (2007). The Evolution of the Near-IR Galaxy Luminosity Function and Colour Bimodality up to $z \sim 2$. In J. Afonso, H. C. Ferguson, B. Mobasher, & R. Norris, editor, *Deepest Astronomical Surveys*, volume 380 of *Astronomical Society of the Pacific Conference Series*, pages 495–+.

Cool, R. J., Eisenstein, D. J., Kochanek, C. S., Brown, M. J. I., Caldwell, N., Dey, A., Forman, W. R., Hickox, R. C., Jannuzi, B. T., Jones, C., Moustakas, J., and Murray, S. S. (2012). The Galaxy Optical Luminosity Function from the AGN and Galaxy Evolution Survey. *ApJ*, 748:10.

de Vaucouleurs, G. (1959). Classification and Morphology of External Galaxies. *Handbuch der Physik*, 53:275.

Faber, S. M., Willmer, C. N. A., Wolf, C., Koo, D. C., Weiner, B. J., Newman, J. A., Im, M., Coil, A. L., Conroy, C., Cooper, M. C., Davis, M., Finkbeiner, D. P., Gerke, B. F., Gebhardt, K., Groth, E. J., Guhathakurta, P., Harker, J., Kaiser, N., Kassin, S., Kleinheinrich, M., Konidaris, N. P., Kron, R. G., Lin, L., Luppino, G., Madgwick, D. S., Meisenheimer, K., Noeske, K. G., Phillips, A. C., Sarajedini, V. L., Schiavon, R. P., Simard, L., Szalay, A. S., Vogt, N. P., and Yan, R. (2007). Galaxy Luminosity Functions to z˜1 from DEEP2 and COMBO-17: Implications for Red Galaxy Formation. *ApJ*, 665:265–294.

Fassbender, R. (2003). . *Diploma Thesis*.

Ferré-Mateu, A., Vazdekis, A., Trujillo, I., Sánchez-Blázquez, P., Ricciardelli, E., and de la Rosa, I. G. (2012). Young ages and other intriguing properties of massive compact galaxies in the local Universe. *MNRAS*, 423:632–646.

Fioc, M. and Rocca-Volmerange, B. (1997). PEGASE: a UV to NIR spectral evolution model of galaxies. Application to the calibration of bright galaxy counts. *A&A*, 326:950–962.

Forbes, D. A., Lasky, P., Graham, A. W., and Spitler, L. (2011). Erratum: Uniting old stellar systems: from globular clusters to giant ellipticals. *MNRAS*, 415:2976–2976.

Franzetti, P., Scodeggio, M., Maccagni, D., Garilli, B., and the VVDS collaboration (2006). Rest-frame color bimodality up to $z \sim 2$ in the VIMOS-VLT Deep Survey. *Memorie della Societa Astronomica Italiana Supplementi*, 9:297–+.

Fried, J. W., von Kuhlmann, B., Meisenheimer, K., Rix, H.-W., Wolf, C., Hippelein, H. H., Kümmel, M., Phleps, S., Röser, H. J., Thierring, I., and Maier, C. (2001). The luminosity function of field galaxies and its evolution since z=1. *A&A*, 367:788–800.

Gray, M. E., Taylor, A. N., Meisenheimer, K., Dye, S., Wolf, C., and Thommes, E. (2002). Probing the Distribution of Dark Matter in the A901/902 Supercluster with Weak Lensing. *ApJ*, 568:141–162.

Hinshaw, G., Weiland, J. L., Hill, R. S., Odegard, N., Larson, D., Bennett, C. L., Dunkley, J., Gold, B., Greason, M. R., Jarosik, N., Komatsu, E., Nolta, M. R., Page, L., Spergel, D. N., Wollack, E., Halpern, M., Kogut, A., Limon, M., Meyer, S. S., Tucker, G. S., and Wright, E. L. (2009). Five-Year Wilkinson Microwave Anisotropy Probe Observations: Data Processing, Sky Maps, and Basic Results. *ApJS*, 180:225–245.

Hogg, D. W. (1999). Distance measures in cosmology. *ArXiv Astrophysics e-prints*.

Hopkins, P. F., Bundy, K., Murray, N., Quataert, E., Lauer, T. R., and Ma, C.-P. (2009). Compact high-redshift galaxies are the cores of the most massive present-day spheroids. *MNRAS*, 398:898–910.

Hubble, E. P. (1925). Cepheids in Spiral Nebulae. *Popular Astronomy*, 33:252.

Hubble, E. P. (1926). Extragalactic nebulae. *ApJ*, 64:321–369.

Hubble, E. P. (1936). *Realm of the Nebulae*.

Ilbert, O., Salvato, M., Le Floc'h, E., Aussel, H., Capak, P., McCracken, H. J., Mobasher, B., Kartaltepe, J., Scoville, N., Sanders, D. B., Arnouts, S., Bundy, K., Cassata, P., Kneib, J.-P., Koekemoer, A., Le Fèvre, O., Lilly, S., Surace, J., Taniguchi, Y., Tasca, L., Thompson, D., Tresse, L., Zamojski, M., Zamorani, G., and Zucca, E. (2010). Galaxy Stellar Mass Assembly Between $0.2 < z < 2$ from the S-COSMOS Survey. *ApJ*, 709:644–663.

Kajisawa, M., Ichikawa, T., Yamada, T., Uchimoto, Y. K., Yoshikawa, T., Akiyama, M., and Onodera, M. (2010). MOIRCS Deep Survey. VIII. Evolution of Star Formation Activity as a Function of Stellar Mass in Galaxies Since z ˜ 3. *ApJ*, 723:129–145.

Kant, I. (1755). *Allgemeine Naturgeschichte und Theorie des Himmels*.

Kauffmann, G., Heckman, T. M., White, S. D. M., Charlot, S., Tremonti, C., Brinchmann, J., Bruzual, G., Peng, E. W., Seibert, M., Bernardi, M., Blanton, M., Brinkmann, J., Castander, F., Csábai, I., Fukugita, M., Ivezic, Z., Munn, J. A., Nichol, R. C., Padmanabhan, N., Thakar, A. R., Weinberg, D. H., and York, D. (2003). Stellar masses and star formation histories for 10^5 galaxies from the Sloan Digital Sky Survey. *MNRAS*, 341:33–53.

Kinney, A. L., Calzetti, D., Bohlin, R. C., McQuade, K., Storchi-Bergmann, T., and Schmitt, H. R. (1996). Template Ultraviolet to Near-Infrared Spectra of Star-forming Galaxies and Their Application to K-Corrections. *ApJ*, 467:38.

Kleinheinrich, M., Rix, H., Schneider, P., Erben, T., Meisenheimer, K., Wolf, C., and Schirmer, M. (2005). Galaxy-Galaxy Lensing Studies from COMBO-17. In Y. Mellier & G. Meylan, editor, *Gravitational Lensing Impact on Cosmology*, volume 225 of *IAU Symposium*, pages 249–254.

Kormendy, J. and Bender, R. (1996). A Proposed Revision of the Hubble Sequence for Elliptical Galaxies. *ApJL*, 464:L119.

Kovacs, Z. (2006). Test of the Infrared Wide-Field Camera OMEGA2000 and its application for an extragalactic survey. *PhD Thesis*.

Kriek, M., van der Wel, A., van Dokkum, P. G., Franx, M., and Illingworth, G. D. (2008). The Detection of a Red Sequence of Massive Field Galaxies at $z \sim 2.3$ and Its Evolution to $z \sim 0$. *ApJ*, 682:896–906.

Lupton, R. H., Gunn, J. E., and Szalay, A. S. (1999). A Modified Magnitude System that Produces Well-Behaved Magnitudes, Colors, and Errors Even for Low Signal-to-Noise Ratio Measurements. *AJ*, 118:1406–1410.

Lynden-Bell, D. (1971). A method of allowing for known observational selection in small samples applied to 3CR quasars. *MNRAS*, 155:95.

Meisenheimer, K., Beckwith, S., Fockenbrock, H., Fried, J., Hippelein, H., Huang, J., Leinert, C., Phleps, S., Roser, H., Thommes, E., Thompson, D., Wolf, C., and Chaffee, F. (1998). The Calar Alto Deep Imaging Survey for Galaxies and Quasars at $z > 5$. In S. D'Odorico, A. Fontana, & E. Giallongo, editor, *The Young Universe: Galaxy Formation and Evolution at Intermediate and High Redshift*, volume 146 of *Astronomical Society of the Pacific Conference Series*, pages 134–+.

Meisenheimer, K. and Roeser, H.-J. (1987). CCD polarimetry using a Savart plate. In Baluteau, J.-P. and D'Odorico, S., editors, *European Southern Observatory Conference and Workshop Proceedings*, volume 25 of *European Southern Observatory Conference and Workshop Proceedings*, pages 227–236.

Nicol, M.-H. (2009). Investigation of the stellar population in galaxies since z=2 by NIR photometry. *PhD Thesis*.

Nicol, M.-H., Meisenheimer, K., Wolf, C., and Tapken, C. (2011). Red-sequence Galaxies at High Redshift by the COMBO-17+4 Survey. *ApJ*, 727:51–+.

Oke, J. B. (1964). Photoelectric Spectrophotometry of Stars Suitable for Standards. *ApJ*, 140:689.

Phleps, S. and Meisenheimer, K. (2003). Clustering evolution between z=1 and today. *Ap&SS*, 284:377–380.

Phleps, S., Peacock, J. A., Meisenheimer, K., and Wolf, C. (2006). Galaxy clustering from COMBO-17: the halo occupation distribution at z = 0.6. *A&A*, 457:145–155.

Phleps, S., Wolf, C., Peacock, J. A., Meisenheimer, K., and van Kampen, E. (2007). COMBO-17 measurements of the effect of environment on the type-dependent galaxy luminosity function. *A&A*, 468:113–120.

Pickles, A. J. (1998). A Stellar Spectral Flux Library: 1150-25000 Å. *PASP*, 110:863–878.

Quadri, R., Marchesini, D., van Dokkum, P., Gawiser, E., Franx, M., Lira, P., Rudnick, G., Urry, C. M., Maza, J., Kriek, M., Barrientos, L. F., Blanc, G. A., Castander, F. J., Christlein, D., Coppi, P. S., Hall, P. B., Herrera, D., Infante, L., Taylor, E. N., Treister, E., and Willis, J. P. (2007). The Multiwavelength Survey by Yale-Chile (MUSYC): Deep Near-Infrared Imaging and the Selection of Distant Galaxies. *AJ*, 134:1103–1117.

Roeser, H.-J. and Meisenheimer, K. (1991). The synchrotron light from the jet of 3C 273. *A&A*, 252:458–474.

Rowlands, K., Dunne, L., Maddox, S., Bourne, N., Gomez, H. L., Kaviraj, S., Bamford, S. P., Brough, S., Charlot, S., da Cunha, E., Driver, S. P., Eales, S. A., Hopkins, A. M., Kelvin, L., Nichol, R. C., Sansom, A. E., Sharp, R., Smith, D. J. B., Temi, P., van der Werf, P., Baes, M., Cava, A., Cooray, A., Croom, S. M., Dariush, A., De Zotti, G., Dye, S., Fritz, J., Hopwood, R., Ibar, E., Ivison, R. J., Liske, J., Loveday, J., Madore, B., Norberg, P., Popescu, C. C., Rigby, E. E., Robotham, A., Rodighiero, G., Seibert, M., and Tuffs, R. J. (2011). H-ATLAS/GAMA: Dusty early-type galaxies and passive spirals. *ArXiv e-prints*.

Sánchez, S. F., Thiele, U., Aceituno, J., Cristobal, D., Perea, J., and Alves, J. (2008). The Night Sky at the Calar Alto Observatory II: The Sky at the Near-infrared. *PASP*, 120:1244–1254.

Sandage, A. (1961). *The Hubble atlas of galaxies*.

Sandage, A. and Tammann, G. A. (1981). *A revised Shapley-Ames Catalog of bright galaxies*.

Sandage, A., Tammann, G. A., and Yahil, A. (1979). The velocity field of bright nearby galaxies. I - The variation of mean absolute magnitude with redshift for galaxies in a magnitude-limited sample. *ApJ*, 232:352–364.

Schechter, P. (1976). An analytic expression for the luminosity function for galaxies. *apj*, 203:297–306.

Schmidt, M. (1968). Space Distribution and Luminosity Functions of Quasi-Stellar Radio Sources. *ApJ*, 151:393.

Scoville, N., Aussel, H., Brusa, M., Capak, P., Carollo, C. M., Elvis, M., Giavalisco, M., Guzzo, L., Hasinger, G., Impey, C., Kneib, J.-P., LeFevre, O., Lilly, S. J., Mobasher, B., Renzini, A., Rich, R. M., Sanders, D. B., Schinnerer, E., Schminovich, D., Shopbell, P., Taniguchi, Y., and Tyson, N. D. (2007). The Cosmic Evolution Survey (COSMOS): Overview. *ApJS*, 172:1–8.

Silk, J. and Mamon, G. A. (2012). The current status of galaxy formation. *Research in Astronomy and Astrophysics*, 12:917–946.

Simon, P., Hetterscheidt, M., Wolf, C., Meisenheimer, K., Hildebrandt, H., Schneider, P., Schirmer, M., and Erben, T. (2009). Relative clustering and the joint halo occupation distribution of red sequence and blue-cloud galaxies in COMBO-17. *MNRAS*, 398:807–831.

Strateva, I., Ivezić, Ž., Knapp, G. R., Narayanan, V. K., Strauss, M. A., Gunn, J. E., Lupton, R. H., Schlegel, D., Bahcall, N. A., Brinkmann, J., Brunner, R. J., Budavári, T., Csabai, I., Castander, F. J., Doi, M., Fukugita, M., Győry, Z., Hamabe, M., Hennessy, G., Ichikawa, T., Kunszt, P. Z., Lamb, D. Q., McKay, T. A., Okamura, S., Racusin, J., Sekiguchi, M., Schneider, D. P., Shimasaku, K., and York, D. (2001). Color Separation of Galaxy Types in the Sloan Digital Sky Survey Imaging Data. *AJ*, 122:1861–1874.

Taylor, E. N. (2008). The $10^{11} M_{\odot}$ Question: Massive Galaxies at $z_{\rm phot} < 2$ and the Rise of the Red Sequence. In Kodama, T., Yamada, T., and Aoki, K., editors, *Panoramic Views of Galaxy Formation and Evolution*, volume 399 of *Astronomical Society of the Pacific Conference Series*, page 173.

Toomre, A. and Toomre, J. (1972). Model of the Encounter Between NGC 5194 and 5195. In *Bulletin of the American Astronomical Society*, volume 4 of *Bulletin of the American Astronomical Society*, page 214.

van de Sande, J., Kriek, M., Franx, M., van Dokkum, P. G., Bezanson, R., Whitaker, K. E., Brammer, G., Labbé, I., Groot, P. J., and Kaper, L. (2011). The Stellar Velocity Dispersion of a Compact Massive Galaxy at z = 1.80 Using X-Shooter: Confirmation of the Evolution in the Mass-Size and Mass-Dispersion Relations. *ApJL*, 736:L9+.

van Dokkum, P. G., Quadri, R., Marchesini, D., Rudnick, G., Franx, M., Gawiser, E., Herrera, D., Wuyts, S., Lira, P., Labbé, I., Maza, J., Illingworth, G. D., Förster Schreiber, N. M., Kriek, M., Rix, H.-W., Taylor, E. N., Toft, S., Webb, T., and Yi, S. K. (2006). The Space Density and Colors of Massive Galaxies at $2 < z < 3$: The Predominance of Distant Red Galaxies. *ApJL*, 638:L59–L62.

Vanden Berk, D. E., Richards, G. T., Bauer, A., Strauss, M. A., Schneider, D. P., Heckman, T. M., York, D. G., Hall, P. B., Fan, X., Knapp, G. R., Anderson, S. F., Annis, J., Bahcall, N. A., Bernardi, M., Briggs, J. W., Brinkmann, J., Brunner, R., Burles, S., Carey, L., Castander, F. J., Connolly, A. J., Crocker, J. H., Csabai, I., Doi, M., Finkbeiner, D., Friedman, S., Frieman, J. A., Fukugita, M., Gunn, J. E., Hennessy, G. S., Ivezić, Ž., Kent, S., Kunszt, P. Z., Lamb, D. Q., Leger, R. F., Long, D. C., Loveday, J., Lupton, R. H., Meiksin, A., Merelli, A., Munn, J. A., Newberg, H. J., Newcomb, M., Nichol, R. C., Owen, R., Pier, J. R., Pope, A., Rockosi, C. M., Schlegel, D. J., Siegmund, W. A., Smee, S., Snir, Y., Stoughton, C., Stubbs, C., SubbaRao, M., Szalay, A. S., Szokoly, G. P., Tremonti, C., Uomoto, A., Waddell, P., Yanny, B., and Zheng, W. (2001). Composite Quasar Spectra from the Sloan Digital Sky Survey. *AJ*, 122:549–564.

Walsh, J. R. (1996). A World Wide Web tool for spectrophotometric standard stars. *The Messenger*, 83:46–48.

Warren, S., Dye, S., and Hambly, N. (2006). The UKIDSS Early Data Release. *The Messenger*, 123:67.

Whitaker, K. E., Labbé, I., van Dokkum, P. G., Brammer, G., Kriek, M., Marchesini, D., Quadri, R. F., Franx, M., Muzzin, A., Williams, R. J., Bezanson, R., Illingworth, G. D., Lee, K.-S., Lundgren, B., Nelson, E. J., Rudnick, G., Tal, T., and Wake, D. A. (2011). The NEWFIRM Medium-band Survey: Photometric Catalogs, Redshifts, and the Bimodal Color Distribution of Galaxies out to $z \sim 3$. *ApJ*, 735:86–+.

White, S. D. M. and Rees, M. J. (1978). Core condensation in heavy halos - A two-stage theory for galaxy formation and clustering. *MNRAS*, 183:341–358.

Williams, R. J., Quadri, R. F., Franx, M., van Dokkum, P., and Labbé, I. (2009). Detection of Quiescent Galaxies in a Bicolor Sequence from z = 0-2. *ApJ*, 691:1879–1895.

Willmer, C. N. A. (1997). Estimating galaxy luminosity functions. *AJ*, 114:898–912.

Wolf, C., Aragón-Salamanca, A., Balogh, M., Barden, M., Bell, E. F., Gray, M. E., Peng, C. Y., Bacon, D., Barazza, F. D., Böhm, A., Caldwell, J. A. R., Gallazzi, A., Häusler, B., Heymans, C., Jahnke, K., Jogee, S., van Kampen, E., Lane,

K., McIntosh, D. H., Meisenheimer, K., Papovich, C., Sánchez, S. F., Taylor, A., Wisotzki, L., and Zheng, X. (2009). Optically-Passive Spirals: the Missing Link in Gradual Star Formation Suppression upon Cluster Infall. In Wang, W., Yang, Z., Luo, Z., and Chen, Z., editors, *The Starburst-AGN Connection*, volume 408 of *Astronomical Society of the Pacific Conference Series*, page 248.

Wolf, C., Dye, S., Kleinheinrich, M., Meisenheimer, K., Rix, H.-W., and Wisotzki, L. (2001a). Deep BVR photometry of the Chandra Deep Field South from the COMBO-17 survey. *A&A*, 377:442–449.

Wolf, C., Gray, M. E., Aragón-Salamanca, A., Lane, K. P., and Meisenheimer, K. (2007). Morphology-dependent trends of galaxy age with environment in A 901/2 seen with COMBO-17. *MNRAS*, 376:L1–L5.

Wolf, C., Gray, M. E., and Meisenheimer, K. (2005). Red-sequence galaxies with young stars and dust: the cluster Abell 901/902 seen with COMBO-17. *A&A*, 443:435–449.

Wolf, C., Hildebrandt, H., Taylor, E. N., and Meisenheimer, K. (2008). Calibration update of the COMBO-17 CDFS catalogue. *A&A*, 492:933–936.

Wolf, C., Meisenheimer, K., Kleinheinrich, M., Borch, A., Dye, S., Gray, M., Wisotzki, L., Bell, E. F., Rix, H., Cimatti, A., Hasinger, G., and Szokoly, G. (2004). A catalogue of the Chandra Deep Field South with multi-colour classification and photometric redshifts from COMBO-17. *A&A*, 421:913–936.

Wolf, C., Meisenheimer, K., Rix, H., Borch, A., Dye, S., and Kleinheinrich, M. (2003a). The COMBO-17 survey: Evolution of the galaxy luminosity function from 25 000 galaxies with $0.2 < z < 1.2$. *A&A*, 401:73–98.

Wolf, C., Meisenheimer, K., and Röser, H. (2001b). Object classification in astronomical multi-color surveys. *A&A*, 365:660–680.

Wolf, C., Meisenheimer, K., Röser, H., Beckwith, S. V. W., Chaffee, Jr., F. H., Fried, J., Hippelein, H., Huang, J., Kümmel, M., von Kuhlmann, B., Maier, C., Phleps, S., Rix, H., Thommes, E., and Thompson, D. (2001c). Multi-color classification in the calar alto deep imaging survey. *A&A*, 365:681–698.

Wolf, C., Wisotzki, L., Borch, A., Dye, S., Kleinheinrich, M., and Meisenheimer, K. (2003b). The evolution of faint AGN between $z \sim 1$ and $z \sim 5$ from the COMBO-17 survey. *A&A*, 408:499–514.

Wuyts, S., Labbé, I., Schreiber, N. M. F., Franx, M., Rudnick, G., Brammer, G. B., and van Dokkum, P. G. (2008). FIREWORKS U_{38}-to-24 μm Photometry of the GOODS Chandra Deep Field-South: Multiwavelength Catalog and Total Infrared Properties of Distant K_s-selected Galaxies. *ApJ*, 682:985–1003.

Danksagung

An dieser Stelle möchte ich all jenen Personen danken, ohne die mein Studium und diese Arbeit wahrscheinlich nie zustande, oder zumindest zu einem Ende gekommen wären.

Mein Dank gilt vor allem meinem Betreuer Dr. Klaus Meisenheimer, der während der dreieinhalb Jahre, in denen diese Doktorarbeit entstanden ist, stets ein offenes Ohr und fast immer eine offene Tür für noch so triviale Fragen meinerseits hatte und sich immer bemühte auftretende Probleme mit mir gemeinsam zu lösen.

Auch danken möchte ich meiner Freundin Natalie, welche mir durch zahlreiches Korrekturlesen, konstruktive Verbesserungsvorschläge und aufbauene Worte durch die Monate des Schreibens geholfen hat. Wie schon bei meiner Diplomarbeit möchte ich hier wieder meiner Mutter danken, die mir auch während meiner Doktorarbeit stets eine Stütze war, auf die ich mich immer verlassen konnte.

Nicht vergessen werden sollten auch die zahlreichen Kollegen und Freunde, die ich am Max Planck Institut kennengelernt habe und die mir sowohl privat als auch fachlich stets zur Seite gestanden sind: Tessel, Bernhard, Maren, Karsten, Kai-Martin, Christian, Nicolas, Ben, André, Roman, Anika, Eva, Markus, Helen. Sie alle standen immer mit ihrem astronomischen Wissen, ihren Programmierkenntnisen und natürlich auch für allerlei Freizeitaktivitäten zur Verfügung. Danke, es war eine schöne Zeit!

An letzter Stelle hier, aber keineswegs in der Wichtigkeit, seien noch die zahlreichen österreichischen Freunde erwähnt, die nie das Vertauen daran verloren, dass ich doch noch einmal zu einem Ende kommen würde.